The Dynamical Behavior of Boundary Layer Ozone in Winter

Dissertation

with the aim of achieving a doctoral degree
at the Faculty of Mathematics, Informatics and Natural Sciences
Department of Earth System Sciences
at Universität Hamburg

submitted by

Xiaoqin Shi

Hamburg

2023

Department of Earth System Sciences

Date of Oral Defense:	19.01.2024
Reviewers:	Prof. Dr. Guy Brasseur Prof. Dr. Jürgen Oßenbrügge
Members of the Examination Commission:	Prof. Dr. Jürgen Böhner Prof. Dr. Gerhard Schmiedl Prof. Dr. Jürgen Oßenbrügge Prof. Dr. Guy Brasseur Prof. Dr. Eva-Maria Pfeiffer Prof. Dr. Jana Sillmann
Chair of the Subject Doctoral Committee Earth System Sciences:	Prof. Dr. Hermann Held
Dean of Faculty MIN:	Prof. Dr.-Ing. Norbert Ritter

The Dynamical Behavior of Boundary Layer Ozone in Winter

Doctoral dissertation

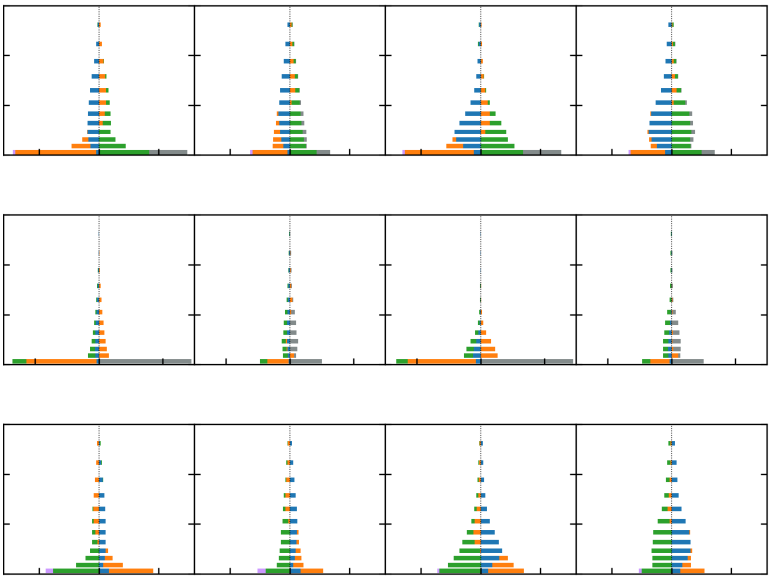

by

XIAOQIN SHI

Hamburg 2023

Abstract

The work focuses on the ozone behavior in the winter boundary layer in the urban area of Beijing. The budget of boundary layer ozone is subject not only to chemical reactions in the atmosphere, but also to turbulent mixing in the boundary layer, advective transport of air masses, pollutant emissions, etc. The dissertation investigates three main external forcing factors of the boundary layer ozone budget in the urban area of Beijing in winter. Two forcing factors affecting the development of turbulence in the boundary layer are large-scale wind and urban heat. Anthropogenic emission related to ozone production and depletion is the third forcing factor. Numerical simulations using the chemical transport model WRF-Chem are performed to investigate the ozone responses to the three external forcing factors. First, under the control of winter monsoon in the Beijing region, a strong northerly wind frequently invades the region and enhances the ozone level in the urban area by up to two times. Four simulations with different nudging strategies are performed to simulate different wind representations. By comparing four nudging simulations, the ozone enhancement in the urban area during the invasion of strong northerly wind is explained by ozone advection from the mountainous areas and the enhanced mechanical turbulent mixing. Good representation of wind shear during the strong northerly wind invasions is essential for reproducing ozone enhancement. Secondly, the important role of urban heat in the evolution of ozone during the day-to-night transition is highlighted. The lowest value of the eddy diffusivity K is reached during the day-to-night transition in simulations without urban heat effect, accompanied by a rapid accumulation of nitrogen oxides (NOx=NO+NO_2) and the associated rapid depletion of ozone. But in the simulation with urban heat effect, the increased turbulent mixing of ozone and NOx leads to significant bias reductions of ozone, from -68% to +0.7%, and of NO_2, from +75% to +6%. Thirdly, the responses of ozone to anthropogenic emissions are tested by redistributing emissions vertically (vertical injection), temporally (diurnal/weekly variation) and horizontally (downscaling). It is found that the simulated ozone concentrations respond strongly to the emission changes in the nocturnal boundary layer due to its low diffusion capacity. The long-narrow zone along the foothills southwest of Beijing is also more sensitive to changes of emissions (in this case the downscaled emissions) than other regions because the southerly wind directed towards the western mountains results in low diffusion capacity. Finally, special attention is paid to the ozone responses to the vast emission reductions following the outbreak of COVID-19 pandemic in China in the first two months of 2020. Contrasting responses of ozone to the nation-wide emission reductions are observed and simulated. In Northern China, the most polluted area in winter, observations show that ozone level increases by a factor of 2 (±0.7) associated with a 53% (±10%) reduction in NO_2, while ozone levels in rural areas of Southern China decrease slightly. The different chemical regimes of ozone production explain the contrasting responses of ozone to NOx emission reductions during the pandemic. The studies in this

dissertation show a novel perspective in studying ozone behavior and provide insights into ozone behavior in the polluted winter boundary layer in light of the increasing ozone trend in China.

Zusammenfassung

Diese Arbeit konzentriert sich auf das Ozonverhalten in der winterlichen Grenzschicht im Stadtgebiet von Peking. Der Haushalt des Grenzschichtozons unterliegt nicht nur den chemischen Reaktionen in der Atmosphäre, sondern auch der turbulenten Durchmischung in der Grenzschicht, dem advektiven Transport von Luftmassen, Schadstoffen usw. Drei wesentliche äußere Einflussfaktoren des Grenzschicht-Ozonhaushalts werden im Stadtgebiet von Peking im Winter untersucht. Zwei treibende Faktoren, die die Entwicklung von Turbulenzen an der Grenzschicht beeinflussen, sind die großräumige Wind und städtische Wärmeinsel. Der dritte treibende Faktor ist die anthropogene Emission im Zusammenhang mit der Ozonproduktion und dem Ozonabbau. Numerische Simulationen werden mit dem chemischen Transportmodell WRF-Chem durchgeführt, um die Ozonreaktionen auf die drei externen Antriebsfaktoren zu untersuchen. Erstens dringt unter der Kontrolle des Wintermonsuns in der Region Peking häufig ein starker Nordwind in die Region ein und kann den Ozonspiegel im Stadtgebiet verdoppeln. Es werden vier Simulationen mit unterschiedlichen Nudging-Strategien durchgeführt, um den Einfluss unterschiedliche Windsysteme zu simulieren. Durch den Vergleich von vier Nudging-Simulationen lässt sich der Ozonanstieg im Stadtgebiet während der Invasion starker Nordwinde durch den advektiv transportierten Ozon aus den Berggebieten und die verstärkte mechanische turbulente Vermischung erklären. Eine gute Darstellung der Windscherung während der Invasion starker Nordwinde ist für die Reproduktion der Ozonverstärkung von entscheidender Bedeutung. Anschließend wird die wichtige Rolle der städtischen Wärme bei der Ozonentwicklung während des Tag-Nacht-Übergangs hervorgehoben. Ohne städtischen Hitzeeffekt wird der niedrigste Wert der turbulenten Wirbeldiffusivität K während des Tag-Nacht-Übergangs erreicht, begleitet von einer schnellen Anreicherung von Stickoxiden ($NOx=NO+NO_2$) und dem damit verbundenen schnellen Ozonabbau. Bei einer Simulation mit städtischem Wärmeeffekt führt die erhöhte turbulente Vermischung von Ozon und NOx zu einer erheblichen Reduzierung des Ozons von -68 % auf +0,7 % und von NO_2 von +75 % auf +6 %. Als nächstes werden die Reaktionen von Ozon auf anthropogene Emissionen getestet, indem die Emissionen vertikal (vertikale Injektion), zeitlich (tägliche/wöchentliche Variation) und horizontal (Downscaling) umverteilt werden. Es zeigt sich, dass die simulierten Ozonkonzentrationen aufgrund ihrer geringen Diffusionskapazität stark auf die Emissionsänderungen in der nächtlichen Grenzschicht reagieren. Die lange, schmale Zone entlang der Ausläufer südwestlich von Peking reagiert außerdem empfindlicher auf Änderungen der Emissionen, in diesem Fall auf die verringerten Emissionen, als andere Regionen. Denn der Südwind (entgegen den westlichen Bergen) führt in dieser Region zu einer geringen Diffusionskapazität. Abschließend wird besonderes Augenmerk auf die Reaktionen des Ozons auf die enormen Emissionsreduzierungen nach dem Ausbruch der COVID-19-Pandemie in China in den ersten beiden Monaten des Jahres 2020 gelegt. Es werden

gegensätzliche Reaktionen des Ozons auf die landesweiten Emissionsreduzierungen beobachtet und simuliert. Beobachtungen zeigen, dass in Nordchina, dem im Winter am stärksten verschmutzten Gebiet, der Ozonwert um den Faktor 2 (±0,7) ansteigt, was mit einer Reduzierung des NO_2 um 53 % (±10 %) einhergeht, während der Ozonwert in ländlichen Gebieten Südchinas leicht sinkt. Die unterschiedlichen chemischen Regime der Ozonproduktion erklären die unterschiedlichen Reaktionen von Ozon auf die Reduzierung der NOx-Emissionen während der Pandemie. Die Studien in dieser Dissertation zeigen eine neue Perspektive bei der Untersuchung des Ozonverhaltens und liefern Einblicke in das Ozonverhalten in einer verschmutzten Wintergrenzschicht vor dem Hintergrund des zunehmenden Ozontrends in China.

Publications related to the thesis

Shi, X., Deroubaix, A., Brasseur, G. P. (2023). Simulation of day-to-night transition of NOx and ozone in the boundary layer (draft to be submitted).

Gaubert, B., Bouarar, I., Doumbia, T., Liu, Y., Stavrakou, T., Deroubaix, A. M., Darras, S., Elguindi, N., Granier, C., Lacey, F., Müller, J. F., **Shi, X.**, Tilmes, S., Wang, T., & Brasseur, G. P. (2021). Global changes in secondary atmospheric pollutants during the 2020 COVID-19 pandemic. *Journal of Geophysical Research: Atmospheres*, *126*(8), e2020JD034213.

Doumbia, T., Granier, C., Elguindi, N., Bouarar, I., Darras, S., Brasseur, G., Gaubert, B., Liu, Y., **Shi, X**., Stavrakou, T., Tilmes, S., Lacey F., Deroubaix A., & Wang, T. (2021). Changes in global air pollutant emissions during the COVID-19 pandemic: a dataset for atmospheric chemistry modeling. Earth System Science Data Discussions, 1-26.

Stavrakou T., Müller J. F., Bauwens M., Doumbia T., Elguindi N., Darras S., Granier C., Smedt I. D., Lerot C., Von Roozendael M., Franco B., Clarisse L., Clerbaux C., Coheur P. F., Liu Y., Wang T., **Shi X.**, Gaubert B., Tilmes S., Brasseur G. P. (2021). Atmospheric impacts of COVID-19 on NOx and VOC levels over China based on TROPOMI and IASI satellite data and modeling. *Atmosphere*, *12*(8), 946.

Shi, X., & Brasseur, G. P. (2020). The response in air quality to the reduction of Chinese economic activities during the COVID-19 outbreak. *Geophysical Research Letters*, *47*(11), e2020GL088070.

Table of Contents

List of figures

List of tables

1 Introduction

1.1 Statement of the problem

The ozone in the Earth's planetary boundary layer represents a secondary pollutant for which the scientific community has been interested for almost a century. It began to attract attention during World War II in Los Angeles, USA [1]. Indeed, during the summer, high ozone levels were observed in this vast urbanized area. Nitrogen oxides and hydrocarbons emitted by complex and intense human activity, for example road traffic and industrial activities, are precursors to the formation of ozone under strong solar radiation. The high concentration of ozone in urban areas represents a form of "atmospheric smog". The desire to understand the chemistry related to ozone in the troposphere has accelerated since then [2].

Before the invention of the supercomputer, thanks to which models of atmospheric composition could be established, the chemistry of ozone was observed in the laboratory and in the field. Transport and chemistry models were then developed to simulate the transport of ozone in the air stream with the chemistry taking place at the same time. The numerical simulation of ozone advances the understanding of ozone chemistry. During the 1990s-2000s, tropospheric ozone chemistry was studied on a global scale because the Earth's atmosphere is a continuum. At the same time, regional models, focusing on specific regions and taking meteorological and chemical fields from global models as boundary and initial conditions, have been developed to resolve atmospheric processes on a smaller scale. Ozone pollution during summer, when photolysis plays an important role, can then be well represented by regional models through which air quality can be predicted, for example, in urban areas. However, the physical and chemical processes that determine the behavior of ozone in the boundary layer during the winter season, when solar radiation is low and photolysis weakens or even ceases to exist, is not yet well understood [3, 4, 5]. During this season, other chemical and physical processes play a major role in determining the ozone levels and its variations in the boundary layer.

The aim of this work is to examine the significance of these processes and to address specific questions that are presented in Section 1.5. First, we summarize the state of our knowledge regarding the atmospheric boundary layer (Section 1.2), the ozone chemistry near the surface (Section 1.3) and the specific mechanisms affecting ozone during wintertime in an urban environment (Section 1.4). Our study will focus on the situation in the Chinese capital region of Beijing, where the level of air pollution in winter is particularly high.

1.2 Atmospheric boundary layer

1.2.1 What is the atmospheric boundary layer (ABL)?

The layer at the bottom of the atmosphere, which is directly influenced by the earth surface, is called the atmospheric boundary layer (ABL). It is located in the first two kilometers (in daytime) above the earth surface as shown in Figure 1-1. The upper border of the boundary layer is characterized by a capping inversion, in which cold air resides below warmer air. Clear diurnal variations of vertical structure of the ABL is attributed to variations in solar radiation (Figure 1-2). During daytime, the earth surface is warmed up as the sun elevates in the sky. Convective motions then develop with the formation of scattered thermals, in which air masses generated above the ground warms up faster than in the surrounding and ascend by buoyancy. Macroscopically, the daytime ABL is dominated by a 1-2km thick convective mixed layer, the top of which is sometimes marked by the bottom of clouds. In the late afternoon when the sun gradually sets, ground heating by solar radiation fades and the ground starts to cool down. During sunset, a very shallow stable layer forms at the bottom of atmosphere, while the air near the ground becomes colder than the air aloft (i.e., a thin inversion layer is formed). The layer above the shallow stable layer collapses into a so-called residual layer as the uplift thermals is interrupted. With the progress of ground cooling at night, the thickened inversion layer forms a nocturnal (stable) boundary layer. After sunrise, a shallow convective layer starts to emerge from the bottom when the ground is heated. The developing convective layer progressively penetrates in the whole nocturnal boundary layer and initiates a new daily cycle of ABL dynamics.

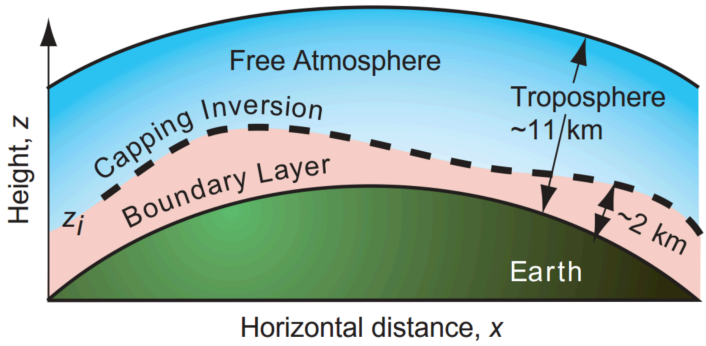

Figure 1-1. The atmospheric boundary layer [6]

The effect of the earth surface on the ABL is manifested itself by the generation and suppression of turbulence. As the atmosphere is a gaseous fluid, turbulence in ABL resembles the viscous fluids under a no-slip condition, in which the fluid in contact with the solid boundary surface has a zero velocity. Due to the fact that the earth surface is not a flat surface, the drag effects of the rough earth surface on atmosphere in ABL are more complex than the idealized case adopted in many fluid dynamics studies and they become larger as one comes closer to the surface. A layer near the earth surface and above most of surface obstacles has the fastest development of

turbulence. This thin layer is called the surface layer (Figure 1-2) and extends as high as one tenth of the height of ABL.

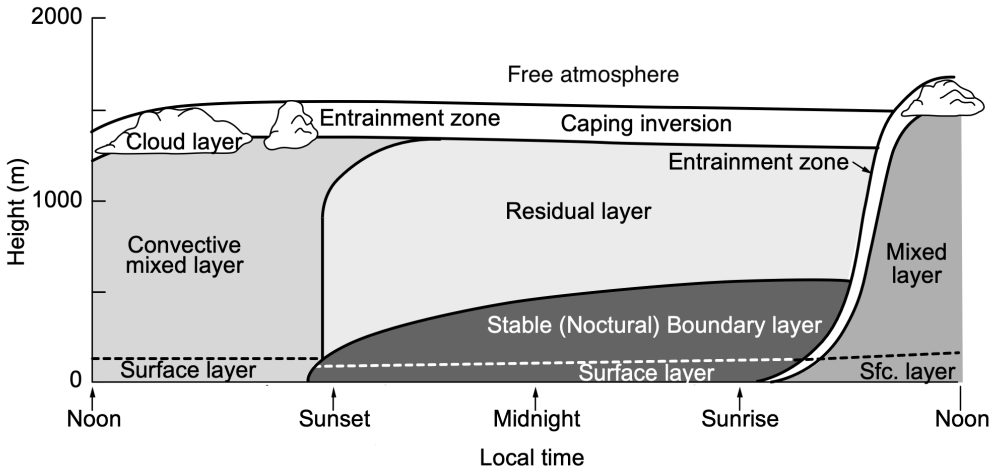

Figure 1-2. The diurnal variation of atmospheric boundary layer structure [7].

1.2.2 Turbulence in ABL

Turbulence in ABL mixes air in all directions due to their chaotic movements that are involved. Vertically, it breaks the layering of atmosphere and creates vertical fluxes of mass, momentum and heat, which play significant roles in the dispersion of air pollutants emitted or produced in the urban or rural atmosphere. In the surface layer, vertical fluxes of mass, momentum and heat by turbulence are conventionally assumed to be constant.

Meteorological parameters, e.g., wind, temperature, humidity, are affected by air motion associated with turbulence. According to the so-called Reynolds averaging procedure, these variables can be separated into an average component (with a horizontal bar on top) and the remaining random turbulent component (also called eddy component, expressed with a prime). For example, the horizontal wind u is split as

$$u = \bar{u} + u' \tag{1-1}$$

If the x-axis follows the direction of u-component of horizontal wind, u is the full horizontal wind. The average of u' is, by definition, equal to zero due to the randomness of the turbulent motions. However, the averages of the vertical turbulent fluxes, which represent the vertical transport of mass, momentum and heat by turbulent motions, are not equal to zero (constants in the surface layer). The vertical turbulent flux of momentum, F_m, is expressed as

$$F_m = \rho_a \overline{w'u'} = -\tau \tag{1-2}$$

where ρ_a is air density (constant) and w' is the turbulent component of the vertical wind. Note that F_m is dominated by the vertical exchanges of horizontal wind momentum, since the atmospheric winds are nearly horizontal.

Due to the unit of F_m resembling the stress (N/m^2), (1-2) is also called Reynolds stress τ. Another important parameter is the friction velocity u_*, which is the velocity scale of turbulence defined as (1-3).

$$u_*^2 = \sqrt{\overline{w'u'}^2} = \tau/\rho_a \tag{1-3}$$

Except for transporting momentum downwards by turbulence, air mass (water vapor and trace gases) and heat (sensible heat and latent heat) are also transported vertically in the boundary layer. The corresponding fluxes (F_μ for fluxes of water vapor or certain trace gas; Q_H, Q_v for sensible heat flux and latent heat flux) are represented as (1-4), (1-5) and (1-6).

$$F_\mu = \overline{w'\mu'} \tag{1-4}$$

$$Q_H = \rho_a c_p \overline{w'\theta_v'} \tag{1-5}$$

$$Q_v = \rho_a L_v \overline{w'q'} \tag{1-6}$$

Variable μ' corresponds to the turbulent component of the mass mixing ratio of water vapor or other trace gases ($\mathrm{kg/kg}$). Coefficient c_p represents the specific heat capacity at constant pressure with a unit of $\mathrm{J}/(kg \cdot K)$ and L_v is the latent heat with a unit of J/kg. θ_v is the virtual potential temperature (K) and q the specific humidity ($\mathrm{kg/kg}$).

In the momentum conservation equation for mean air motions, the flux term $\overline{w'u'}$ is included in the term representing turbulent frictional (viscous) force [8], which is highlighted with the shaded color in (1-7).

$$\frac{\partial \overline{v_i}}{\partial t} + \sum_{j=1,2,3} \overline{v_j} \frac{\partial \overline{v_i}}{\partial x_j} = -\frac{1}{\overline{\rho_a}} \frac{\partial \bar{p}}{\partial x_i} - \delta_{i3} g + \sum_{j=1,2,3} \nu \frac{\partial^2 \overline{v_i}}{\partial {x_j}^2} + \sum_{j=1,2,3} f \epsilon_{ij3} \overline{v_j} - \sum_{j=1,2,3} \frac{\partial \overline{v_i' v_j'}}{\partial x_j} \tag{1-7}$$

Where $i = 1, 2, 3$, v_i represents the three spatial components of the wind velocity u, v, w and x_i represents the three components of the location $\mathrm{x, y, z}$. $\bar{p}$ represents the mean air pressure, g is the gravitational acceleration, ν is the molecular viscosity and f is the Coriolis parameter.

δ_{i3} is the Kronecker symbol

$$\delta_{i3} = \begin{cases} 1, & if\ i = 3 \\ 0, & if\ i \neq 3 \end{cases}$$

ϵ_{ij3} is Levi-Civita symbol

$$\epsilon_{ij3} = \begin{cases} +1, & if\ ij = 12 \\ -1, & if\ ij = 21 \\ 0, & if\ i = j\ or\ i = 3\ or\ j = 3 \end{cases}$$

The mean wind velocity is influenced by the random turbulent motions, which, in other words, transport momentum. Closing the equation (1-7 requires that the flux term $\overline{v_i' v_j'}$ be expressed as a function of mean wind velocity values. The turbulent closure problem requires therefore that a parameterization of the flux term be introduced. The most-accepted approach for turbulent closure is the mixing length theory developed by Prandtl [9]. This semi-empirical theory assumes that the transport of momentum by turbulence is similar to that by molecular viscosity. The Reynolds stress τ can be therefore viewed as an analogy with the molecular viscous stress τ', which is proportional to the normal-direction gradient of the velocity as shown in (1-8a). The Reynolds stress τ is represented by (1-8b).

$$\frac{\tau'}{\rho'} = \nu \frac{dU}{dz} \tag{1-8a}$$

$$\frac{\tau}{\rho_a} = K_m \frac{d\bar{u}}{dz} = u_*^2 = -\overline{w'u'} \tag{1-8b}$$

The coefficient K_m is called eddy diffusivity for momentum. Thus, the calculation of the term $\overline{w'u'}$ is approximated by calculating the product between K_m and $\frac{d\bar{u}}{dz}$ and the turbulence closure problem is therefore simplified. The molecular viscosity $\nu \approx \bar{U} l$, where $\bar{U}$ is the mean velocity of molecular motion and l is the mean free path. By analogy, the eddy diffusivity $K_m \propto \mathrm{V} l_m$, where V is the characteristic turbulent velocity scale, which can be represented by u_*, and l_m is the mixing length that is proportional to the height z. Therefore, following the mixing length theory, the eddy diffusivity K_m is simply parameterized as (1-9).

$$K_m = \kappa u_* z \tag{1-9}$$

The proportional factor κ is the von Kármán constant with a value of typically 0.4.

1.2.3 Driving factors of turbulence: mechanical and buoyant

The generation, maintenance and dissipation of turbulence are controlled by turbulent kinetic energy (TKE), which, for a unit mass of air, is defined as

$$\bar{e} = \frac{1}{2}\left(\overline{u'}^2 + \overline{v'}^2 + \overline{w'}^2\right) \tag{1-10}$$

By assuming horizontally uniform conditions and no vertical motions ($\bar{w} = 0$), turbulent energy equation is derived as (1-11) [8].

$$\frac{\partial \bar{e}}{\partial t} = \frac{g}{\overline{\theta_v}} \overline{w'\theta_v'} - \overline{w'u'} \frac{\partial \bar{u}}{\partial z} - \frac{\partial(\overline{w'e})}{\partial z} - \frac{1}{\overline{\rho_a}} \frac{\partial(\overline{w'p'})}{\partial z} - \xi \tag{1-11}$$

There are five components determining the production/consumption of turbulent energy. On the right side of (1-11), the first term $\frac{g}{\overline{\theta_v}} \overline{w'\theta_v'}$ is the buoyant

production/consumption. The second term $-\overline{w'u'}\frac{\partial \overline{u}}{\partial z}$ is the mechanical (shear) production. This term is always positive, because the signs of the wind shear ($\frac{\partial \overline{u}}{\partial z}$) and of the turbulent momentum flux ($\overline{w'u'}$) are opposite. The second term indicates that the wind shear determines the production of mechanical turbulence. The third and fourth terms $-\frac{\partial(\overline{w'e})}{\partial z}$ and $-\frac{1}{\overline{\rho_a}}\frac{\partial(\overline{w'p'})}{\partial z}$ are, respectively, the turbulent transport of TKE and the pressure perturbation. The last term $-\xi$ is the molecular viscous dissipation of TKE.

The production of turbulence in the ABL is mainly controlled by the competition between buoyant production/consumption and the mechanical (shear) production, which are the first and second terms in (1-11). The intensity of buoyancy in the ABL is dependent on solar radiation, cloudiness, the surface material and so on. When the buoyant term in (1-11) is positive (buoyancy is upward), the earth surface is heated to become warmer than the air aloft, and thermal turbulences emerge (normally during daytime in Figure 1-2). On the opposite, if the buoyant term is negative (during nighttime in Figure 1-2), turbulence produced by the mechanical (shear) term is suppressed. Figure 1-3 depicts approximate regimes of turbulent states under different combinations of buoyant production of TKE and shear (mechanical) production of TKE. The turbulent condition dominated by buoyant production is called free convection, which is associated with strong solar radiation, e.g., thunderstorm in summer. The forced convection refers to turbulence mainly generated by shear production, which mostly happens under overcast and windy weather. In between, turbulence can be driven comparably by shear and buoyancy, for example during daytime with moderate weather. When the suppression of buoyancy is comparable to the shear production, stably stratified turbulence occurs, as observed in the nocturnal boundary layer shown in Figure 1-2. In a cloudless and stable winter night with the excessive radiative cooling of the ground, turbulence can cease because the suppression of buoyancy dominates over the shear production.

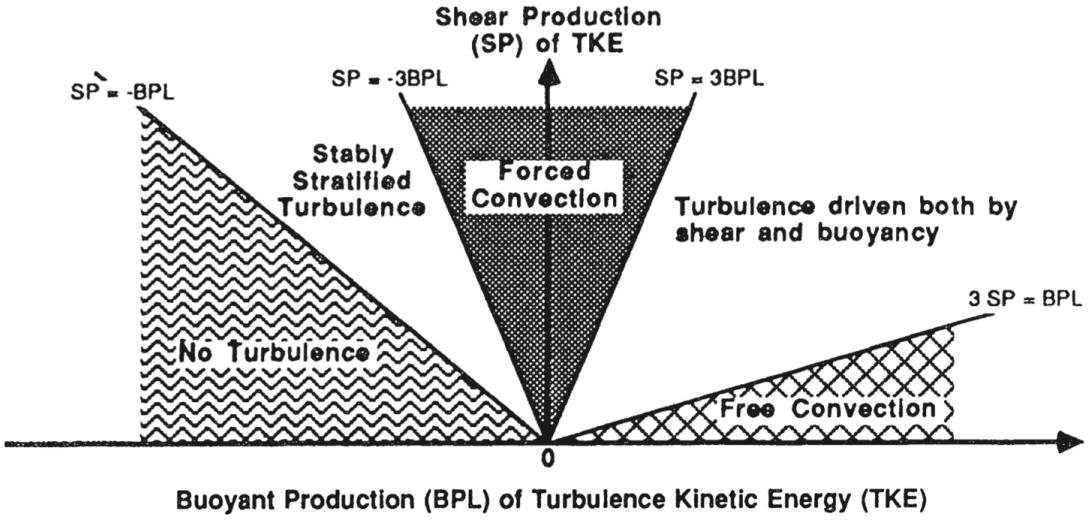

Figure 1-3. Approximate regimes of turbulent driven forces in ABL [7]..

In the Monin-Obukhov (M-O) similarity theory for the surface layer [10], a parameter with unit of length, called M-O Length L as defined in (1-12), is defined to represent the comparison of contributions between mechanical (shear) production and buoyant production.

$$\mathrm{L} = -\frac{u_*^3}{\kappa \frac{g}{\overline{\theta_v}} \overline{(w'\theta_v')_s}} \tag{1-12}$$

The quantity $(w'\theta_v')_s$ is proportional to the sensible heat flux Q_H as indicated in (1-5) at the surface. Here u_* in the numerator represents the contribution of mechanical (shear) production. The denominator includes the buoyant production/consumption of TKE at the surface. The quantity of $|L|$ can be interpreted as 'the height of the sub-layer of dynamic turbulence' [10]. Here the word 'dynamic' is interchangeable with 'mechanical'. M-O Length L is also thought to be the height of the surface layer (Figure 1-2), in which turbulent fluxes are constant and the friction velocity u_* is an important velocity scale. In the surface layer, turbulence is mainly driven by mechanical forces. When $\mathrm{z} \ll |L|$, turbulence is mechanical. With $\mathrm{z} = |L|$, turbulence is equally influenced equally by buoyancy (upward or downward) and mechanical forces. If $\mathrm{z} \gg |L|$, buoyancy (upward or downward) dominates the turbulence.

The static stability of the surface layer can be classified as 'unstable', 'stable' and 'neutral' based on the value of $\zeta = \mathrm{z}/\mathrm{L}$. When $\zeta < 0$, buoyancy is upward and contributes to the turbulence production; in this case, the surface layer is 'unstable'. When $\zeta > 0$, buoyancy suppresses the turbulence production and the surface layer is 'stable'. When $\zeta = 0$, turbulence is only mechanical and the surface layer is determined as being 'neutral'. The dynamical stability of the surface layer is merely represented by mechanical production (wind shear) of turbulence.

Due to the influence of buoyancy, the eddy diffusivity K_m for momentum must be adjusted for 'unstable' or 'stable' conditions. The parameterization of K_m defined in (1-9) satisfies only the 'neutral' condition. In order to make the parameterization compatible with universal conditions, the dimensionless quantity of wind shear is replaced by a function of ζ, as shown in (1-13), instead of being unity. As a result, the eddy diffusivity K_m is adjusted as (1-14).

$$\frac{\kappa z}{u_*}\frac{\partial \overline{u}}{\partial z} = \varphi_m(\zeta) \tag{1-13}$$

$$K_m = \frac{\kappa u_* z}{\varphi_m(\zeta)} \tag{1-14}$$

Under 'neutral' condition, the universal function $\varphi_m(0) = 1$. Through field observations, empirical forms of $\varphi_m(\zeta)$ are obtained as in (1-15) and (1-16) [11, 12].

$$\varphi_m(\zeta)_{unstable} = (1 - A\zeta)^{-1/4} \tag{1-15}$$

$$\varphi_m(\zeta)_{stable} = 1 + B\zeta \tag{1-16}$$

Different values of factors A and B are adopted by different studies. For example, $A = 15.0$ and $B = 4.7$ in the study of Businger et al. [11].

1.3 Ozone chemistry in ABL

1.3.1 Mechanism of ozone production

Ozone (O_3, a molecule that contains three oxygen atoms) is produced in the troposphere by a series of chemical reactions that mainly involve the presence of Volatile Organic Compounds (VOCs) and Nitrogen Oxides (NOx=NO_2+NO) under solar radiation. In 1950s, the attribution of the formation of the ozone 'smog' observed in the urban area of Los Angeles was discovered by Dr. Arie Jan Haagen-Smit [13]. VOCs, mainly hydrocarbons (RH), or Carbon monoxide (CO) [14] are oxidized by the hydroxyl radical (OH) and produces the hydroperoxyl radical (HO_2) as shown in (1-18) or several organic peroxy radical (RO_2) as shown in (1-17). Nitric oxide (NO) emitted for example by car exhaust is then oxidized by RO_2 or HO_2 to form the nitrogen dioxide NO_2 as shown in (1-19) and (1-20), which is photolyzed (wavelength of solar radiation is less than 420nm) to produce one ground state oxygen atom $O(^3P)$, as shown in (1-21). Eventually, $O(^3P)$ collides with one oxygen molecule O_2 in the presence of an inert molecule such as nitrogen molecule N_2 or O_2 to form one ozone molecule (O_3), as shown in (1-22). Intense solar radiation is therefore the energy source of ozone formation (the photolysis of NO_2). This explains why ozone 'smog' pollution usually happens in the afternoon during summertime in polluted urban areas, where emissions of VOCs, CO and NOx emitted from traffic, industrial processes and others are high.

$$RH + OH + O_2 \rightarrow H_2O + RO_2 \quad (1\text{-}17)$$

$$CO + OH + O_2 \rightarrow CO_2 + HO_2 \quad (1\text{-}18)$$

$$NO + RO_2 \rightarrow RO + NO_2 \quad (1\text{-}19)$$

$$NO + HO_2 \rightarrow OH + NO_2 \quad (1\text{-}20)$$

$$NO_2 + h\nu\ (\lambda < 420nm) \rightarrow NO + O(^3P) \quad (1\text{-}21)$$

$$O(^3P) + O_2 + M \rightarrow O_3 + M \quad (1\text{-}22)$$

The ozone molecules that are produced by this reaction chain can be consumed by reactions with NOx (also called NOx titration), as shown in (1-23) and (1-24), or by entering an oxidation chain involving VOCs, as indicated by (1-25).

$$NO + O_3 \rightarrow NO_2 + O_2 \quad (1\text{-}23)$$

$$NO_2 + O_3 \rightarrow NO_3 + O_2 \quad (1\text{-}24)$$

$$RH + O_3 \rightarrow \cdots \rightarrow CO_2 + H_2O \qquad (1\text{-}25)$$

Both of NOx and VOCs, as ozone precursors, are important for the formation of ozone. The abundance of ozone is a nonlinear function of the precursors' levels as highlighted in Figure 1-4. This diagram, which shows ozone isopleths, is based on numerical modelling performed for different concentrations of NOx and VOCs. When the ratio of VOCs and NOx is larger than 15 (downright region of the graph in Figure 1-4), the abundance of VOCs does not affect the production of ozone anymore. Instead, the ozone production increases with increasing concentrations of NOx. This chemical regime is conventionally called 'NOx-limited' regime. On the opposite, when the ratio of VOCs and NOx is smaller than 4 (upperleft region of the graph in Figure 1-4), VOCs is the major precursor that controls the ozone production; this chemical regime is usually called 'VOC-limited' regime. The level of ozone is not completely insensitive to the level of NOx in the 'VOC-limited' regime, in which the ozone concentration decreases with an increase in the NOx level due to NOx titration. The chemical regime of the urban area is often 'VOC-limited', while the rural area with large biogenetic emissions of VOCs is under 'NOx-limited' regime.

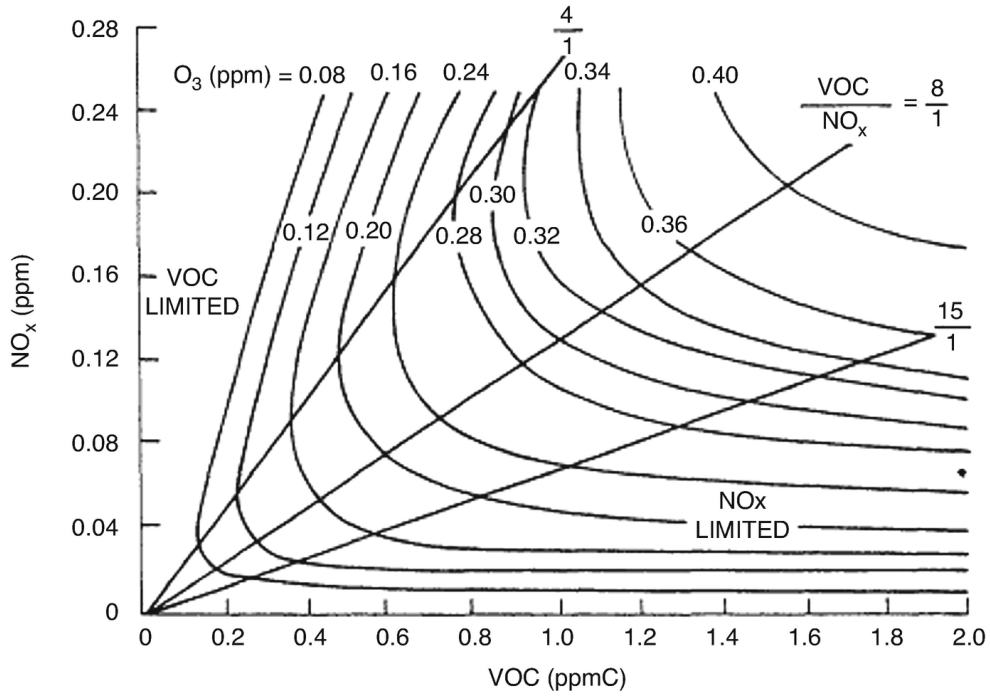

Figure 1-4. EKMA (Empirical Kinetic Modelling Approach) diagram of ozone isopleth controlled by levels of VOCs and NOx [15].

1.3.2 Chemical relation between ozone and NOx

During daytime, the production of ozone is closely associated with the level of NOx, particularly in 'NOx-limited' region, where the ozone production increases with the increase of NOx abundances. Assuming that the level of VOCs is fixed at a value of 0.6 ppm as in Figure 1-4, the increase of ozone production by increasing the level of NOx gradually slows down and even ceases when the level of NOx reaches the value of 0.14 ppm. By continuing to increase NOx, the chemical regime is switched to 'VOC-

limited' and the ozone production changes inversely with the increase of NOx. This is because the excessive NOx enhances ozone loss by (1-23) and (1-24) and hinders the ozone production by reducing the level of HOx (HOx=OH+HO2) as shown in (1-26). The gas-phase nitric acid (HNO_3) can be removed from the atmosphere by being dissolved in the liquid water of cloud drops and aerosol particles and deposited on the ground or being washed out during rain events.

$$NO_2 + \mathrm{OH} \rightarrow HNO_3 \quad (1\text{-}26)$$

$$O_3 + h\upsilon\ (\lambda < 319nm) \rightarrow O_2 + O(^1D) \quad (1\text{-}27)$$

$$O(^1D) + H_2O \rightarrow 2OH \quad (1\text{-}28)$$

At night, the formation of OH, which relies on ozone photolysis in the humid air during daytime with reactions (1-27) and (1-28), ceases and the OH level is largely reduced. Ozone then represents a major nighttime oxidant [16]. Ozone plays an important role in removing NOx from the atmosphere at night. First, NO, which is continuously emitted at night, is oxidized by ozone to produce NO_2 by the reaction (1-23). Then NO_2, which can be directly emitted or produced from NO, reacts with ozone to produce nitrate radicals (NO_3) by the reaction (1-29). NO_3 then combines with NO_2 to produce dinitrogen pentoxide (N_2O_5) by the reaction (1-30). At the end, N_2O_5 is converted to HNO_3 by hydrolysis reactions in the presence of aerosols, as indicated in (1-31). In the areas with high levels of VOCs, another important loss of NO_2 is provided by the reaction with peroxyacetyl radicals (CH_3CO_3) to produce the peroxyacetylnitrate reservoir (PAN, formula $CH_3CO_3NO_2$) [17], whose lifetime is one hour at 295K but months at 250K [18]. After joining the colder air flow at high altitudes, PAN can travel for thousands of kilometers before it encounters warmer air masses where it decomposes into the original reactants. This mechanism, as shown in (1-32), brings short-lived pollutants (NOx) to remote areas.

$$NO_2 + O_3 \rightarrow NO_3 + O_2 \quad (1\text{-}29)$$

$$NO_2 + NO_3 \rightarrow N_2O_5 \quad (1\text{-}30)$$

$$N_2O_5 + H_2O(l) \rightarrow 2HNO_3 \quad (1\text{-}31)$$

$$NO_2 + CH_3CO_3 + M \rightleftharpoons CH_3CO_3NO_2 + M \quad (1\text{-}32)$$

1.4 The specificity of ozone behavior in winter

1.4.1 ABL in Winter

The characteristics of the atmospheric boundary layer in winter depend on latitude, topography and climate of the region under consideration. This study focuses on the wintertime situation (December-January-February) in the region of Beijing, in northern

China. Under the control of winter monsoon, this region is characterized as 'cold', 'dry' and 'windy' in winter.

At the latitude of 40°N, shorter daytime and lower solar elevation in winter limit the solar energy reaching the earth surface. During daytime, the peak height of ABL is on average 50% lower than during summer time (Figure 1-5). At night, buildings with heating systems emit extra anthropogenic heat to the atmosphere and reduce the stability of the ABL [19]. The region of Beijing during wintertime is prone to windy and cold weather, as the winter monsoon with cold circulation system proceeds southwardly from Siberia in Russia to the region. During these windy and cold days, the ABL is mainly under neutral conditions, in which the intensity of turbulent motions in the ABL is controlled by winds (mechanical force).

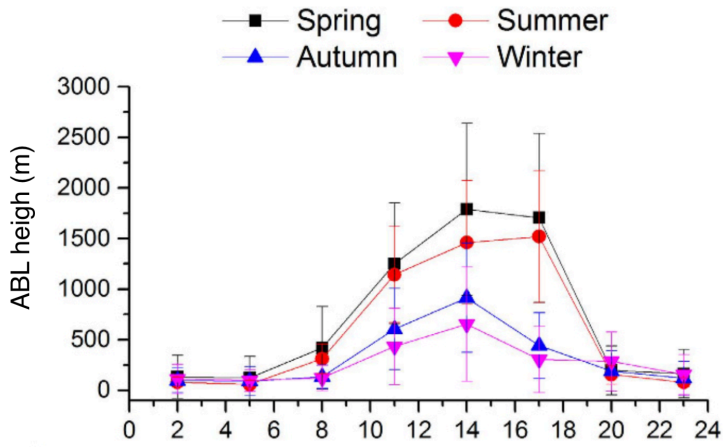

Figure 1-5. Diurnal variation of long-term statistic ABL heights in Beijing [20].

1.4.2 Emission and Chemistry in winter

The period in Beijing during which buildings are heated covers the entire wintertime. Coal burning is the main energy source for winter heating in northern China. According to the report 'The plan of clean winter heating in northern China (2017-2021)' by the National Development and Reform Commission of China [21], 83% of the total heating area in northern China use coal as burning fuel. In Beijing, coal burning contributes to around 40% of the total annual NOx emissions and in winter over 50% of NOx emissions are from coal burning [22]. Through the year, NOx emissions in winter reach their highest point in winter, resulting in high concentrations of ambient NOx in winter.

In addition to the high winter emissions of NOx, high winter ambient NOx levels are also attributed to shallower ABL and unfavorable atmospheric conditions for chemical losses of NOx. During dry and dark winters, the pathway of NOx loss by reacting with OH, as shown in (1-26), is considerably reduced due to the low production of OH, which depends on the ozone level, as indicated by the reactions (1-27) and (1-28).

Therefore, the pathway of NOx loss initiated by ozone reacting with NO becomes important, as explained in Section 1.3.2. This is also highlighted in the study of Zong Z. et al. [22]. The low concentration of OH also hinders the formation of ozone in winter.

As a result, the concentration of ambient ozone in winter is in most cases lower than the limits based on air quality criteria. In the model simulation of Beijing in January of 2019, the net ozone production is seen mostly in layers around the top of or above the ABL in daytime (Figure 1-6). A net destruction of ozone takes place under 300 meters. The produced ozone on the top of the ABL is transported downward by turbulent mixing in the ABL. As a result, an afternoon maximum of surface ozone concentration can be observed (blue line in Figure 1-10).

In winter, the concentrations of ozone change inversely with NOx in urban areas due to the dominance of NOx titration. The chemical regime of ozone production in winter is normally 'VOC-limited' in urban areas under conditions of high concentration of NOx and the lack of radicals HOx [23]. Figure 1-7 shows the results of a zero-dimension model taking chemistry, vertical turbulent mixing and deposition into account. This model simulates the changes in the concentrations of NOx, ozone, OH and HO_2 with an increase of the NOx emission rate [24]. In spring (March and May) and summer (July), the concentrations of ozone and HOx increase first and decrease after NOx emission rate gets larger than a certain value. However, in winter (January), ozone concentration solely decreases with the increase of NOx emission rate, even in the case of very low NOx emission rate. The very low HOx level and low solar radiation in winter (January) cause net chemical destruction of ozone, as the NOx titration by the reaction (1-23) consistently surpasses the rate of NO_2 photolysis by the reaction (1-19) that produces ozone. In the real atmosphere, the ozone deficit in the chemical system during wintertime in urban areas is replenished by turbulent mixing (transporting ozone from upper ABL to the surface layer) and advective transport (displacing ozone from rural to urban areas).

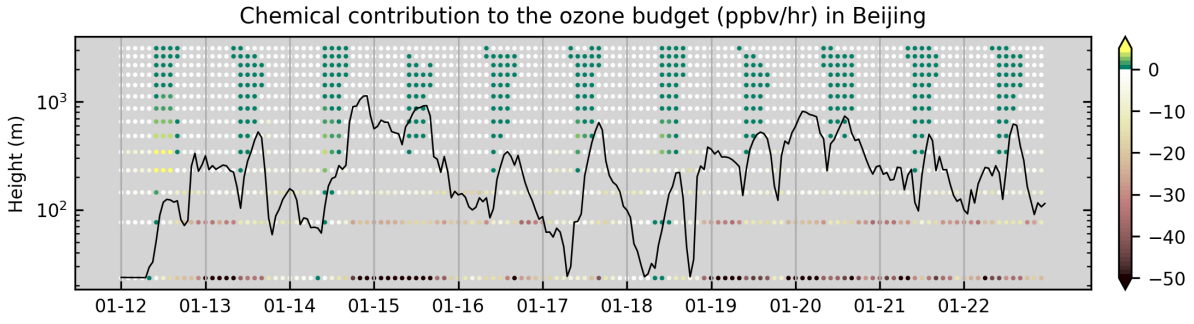

Figure 1-6. Time-height cross section of chemical contribution of the ozone budget (ppbv/hr, parts per billion by volume per hour) simulated in Beijing in January of 2019. Black line represents the height of simulated ABL.

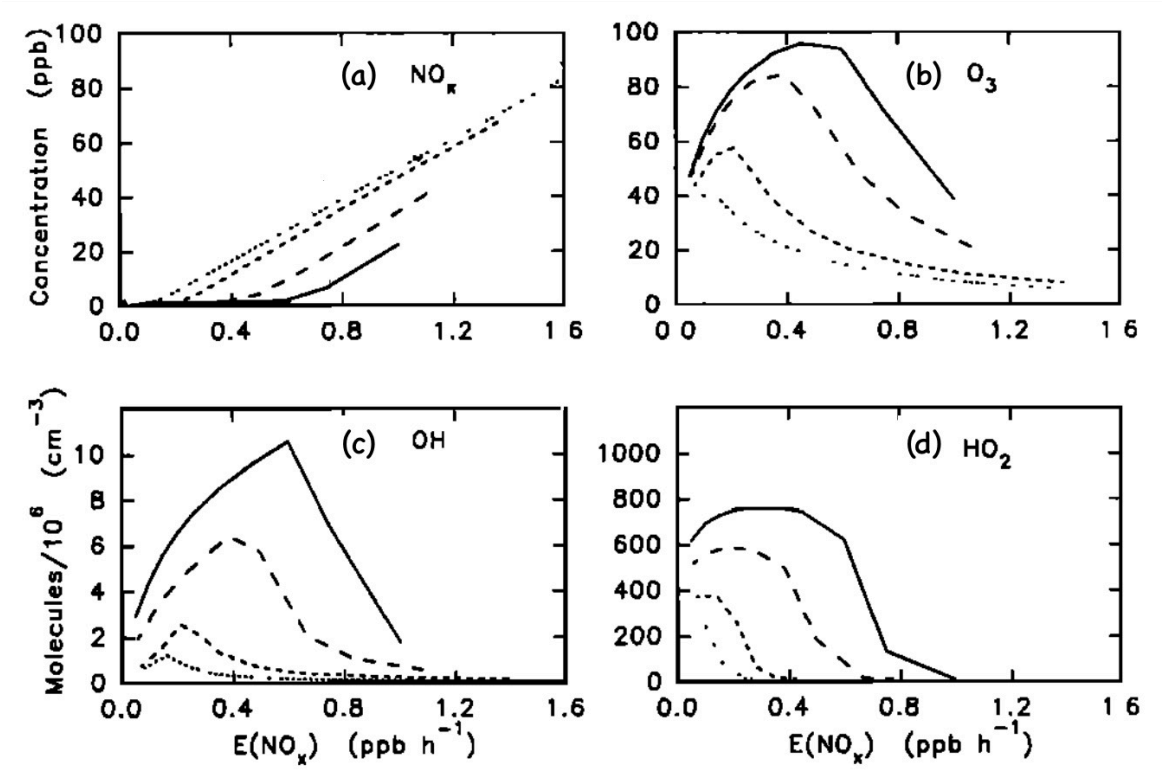

Figure 1-7. Concentrations of NOx (a), ozone (b), OH (c) and HO_2 (d) as a function of NOx emission rate. Simulations of a zero-dimension model in environmental conditions of January (dotted line), March (short dashed line), May (long dashed line) and July (solid line) on the latitude of 40°N [25].

1.4.3 Budget of ozone in winter

Trace gases in atmosphere are subject to chemistry as well as to dynamical processes, for example turbulent mixing and advective transport. The removal of trace gases from the atmosphere includes dry deposition and wet scavenging during rain events. Primary trace gases are first emitted from the biosphere and the lithosphere on earth. One of the most variable and significant sources among them is anthropogenic sources. In Figure 1-8, the budgets of ozone and NOx are summarized schematically for wintertime in polluted urban areas. The winter ozone chemistry in the surface layer is closely associated with NOx titration. Primary NOx (mainly NO) is supplemented by emissions, most of which are anthropogenic, for example coal burning and traffic. Losses of ozone and NOx by dry deposition are relatively small and low occurrence of precipitation in winter reduces the loss of trace gasses by wet scavenging. Turbulent mixing and transport exert opposite contributions to the abundance of ozone and NOx in the surface layer. The diffusion of high NOx relies on turbulent mixing and advective transport, which at the same time bring ozone into the area.

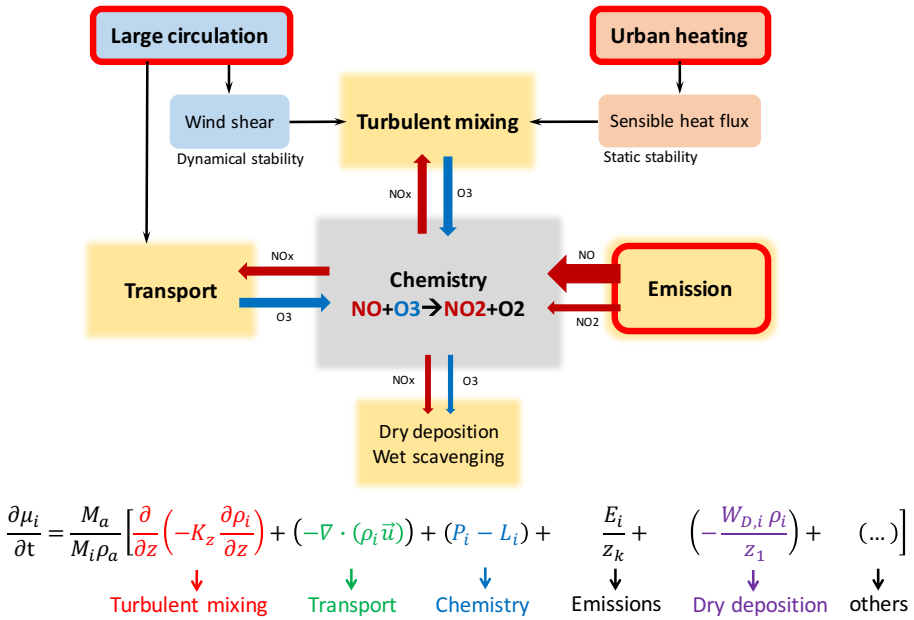

$$\frac{\partial \mu_i}{\partial t} = \frac{M_a}{M_i \rho_a}\left[\frac{\partial}{\partial z}\left(-K_z \frac{\partial \rho_i}{\partial z}\right) + \left(-\nabla \cdot (\rho_i \vec{u})\right) + (P_i - L_i) + \frac{E_i}{z_k} + \left(-\frac{W_{D,i}\,\rho_i}{z_1}\right) + (\ldots)\right]$$

Turbulent mixing | Transport | Chemistry | Emissions | Dry deposition | others

Figure 1-8. Schematic of budgets of ozone and NOx and the simplified formulas of time derivative of mixing ratio of chemical specie i represented by a sum of budget components. In the schematic, red boxes mark out external forcing factors of the system, black arrows indicate influence relationships, red and blue arrows represent contributions of respective budget components to the abundance of ambient ozone (blue) and NOx (red) in the surface layer of certain area. In the formula, μ_i is the molar mixing ratio of chemical specie i, M_a and M_i are respectively molar mass of air and chemical specie i, ρ_a and ρ_i are respectively mass density of air and chemical specie i, K_z is eddy diffusivity for vertical turbulent mixing, $\vec{u}$ is wind vector, P_i and is chemical production rate, L_i is chemical loss rate, E_i is mass emission flux, z_k is atmospheric layer thickness, $W_{D,i}$ is dry deposition velocity, z_1 is bottom layer thickness.

Spatial distributions of ozone (NOx) indicate the positive (negative) contributions of transport and turbulent mixing to the abundance of ozone (NOx) in urban areas. In the case of Beijing, NOx is contained in the shallow ABL and accumulates in urban areas (Figure 1-9a), while ozone is abundant above ABL and in rural mountainous regions (Figure 1-9b). The turbulent flux $-K_z \frac{\partial \rho_i}{\partial z}$ is proportional to the counter-gradient of the mass density (formula in Figure 1-8), so that turbulent mixing produces downward (upward) turbulent fluxes of ozone (NOx) in the city of Beijing (confirmed by studies in [26, 27]). Similarly, advective transport diffuses NOx out of the city and brings ozone into the city from rural or suburban areas. In polluted urban area under the control of the winter monsoon, the shallow and stable ABL constrains the diffusion of ambient pollutants, which are primarily emitted to the atmosphere mainly by fossil fuel combustion. These emitted pollutants tend to accumulate fast and to reach large abundances. At the same time, ozone is largely and consistently consumed by NOx titration. Therefore, the ozone concentration in the urban area appears to be very low in contrast with the surrounding rural areas. Figure 1-9 shows that the NOx-abundant area, which is in the ABL and in the urban area of Beijing, corresponds to the ozone-deficient area (also called 'ozone cavity').

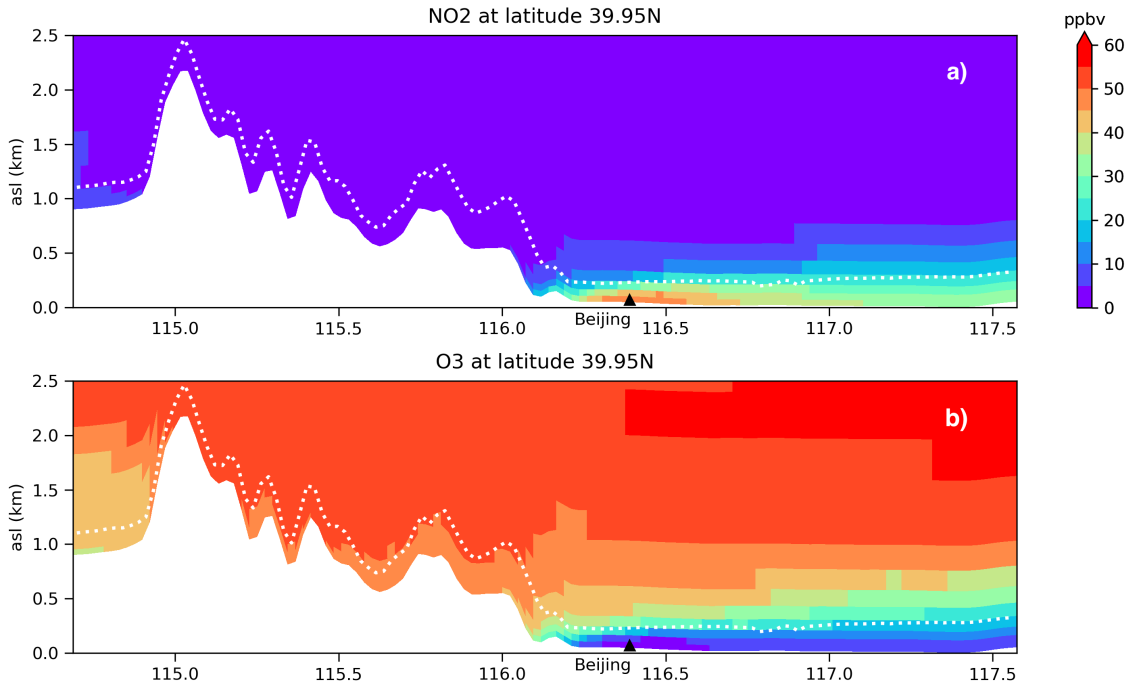

Figure 1-9. Longitude-height cross section of mean mixing ratio of NO_2 and ozone in a period from January 12 to 22, 2019 simulated by a regional model.Unfilled white area represents mountains; white dotted line is the mean height of ABL; asl represents height above sea level.

Ozone and NO_2 have an inverse relationship (seen in Figure 1-10 and studies in [28, 29]). Diffusion of NOx by turbulent mixing and transport compete with high emissions of NOx in polluted urban areas, which determines the specific ozone behavior in the winter boundary layer. Three external forcing factors play important roles in controlling the ozone-NOx system in polluted urban areas during wintertime (red boxes in Figure 1-8). First, large circulation exerts influence on dynamical stability of the ABL by modifying the wind shear. At the same time, the transport of air masses is also controlled by the large circulation. Under the control of the winter monsoon, the large circulation plays an important role in turbulent diffusion and advectively transport diffusion of pollutants. Second, the urban heating in winter provides an extra energy source for the atmosphere and modifies the static stability of the ABL (reduced buoyant suppression), especially at night. Third, emissions, especially anthropogenic emissions in polluted urban areas, determine the intensity of NOx titration and the associated ozone behavior. This thesis investigates the behavior of ozone during winter in polluted urban areas, which is affected by three external forcing factors: large circulation, urban heating and emissions.

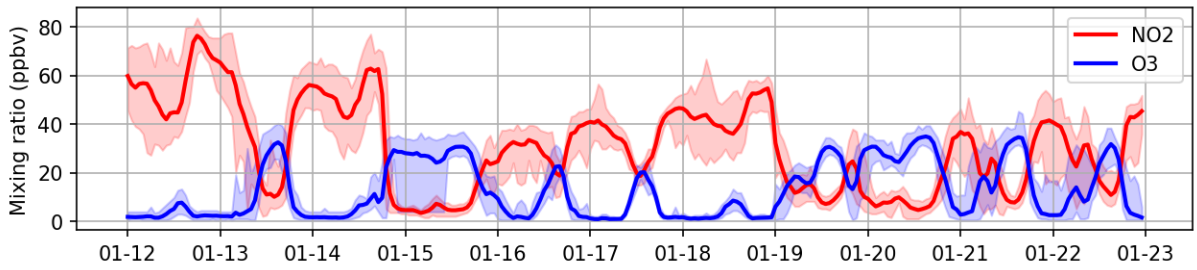

Figure 1-10. Observations of surface ozone and NO_2 in Beijing in January of 2019. Shadow under lines is the range of observed values of 12 observation sites.

1.5 Questions to be answered in this thesis

The objective of the thesis is *to quantify the contribution of different physical and chemical processes that determine the level of ozone in the urban atmospheric boundary layer of the polluted area of Beijing during wintertime*. The study provides science-based information that should contribute to mitigation actions required to improve air quality in the capital city of China and imply the potential responses of winter ozone to the continuing urbanization and climate change. The thesis addresses three scientific questions.

- **Question 1: How do large-scale winds influence the ozone behavior during wintertime?**

Large-scale winds controlled by synoptic-scale circulations provide a forcing mechanism for the local boundary layer and represent an energy source for mechanical turbulence in the ABL. They influence the abundance of surface layer ozone directly by transport or indirectly by modifying turbulent mixing in ABL. Strong large-scale circulation (strong winds) enhances the diffusion of primary pollutants (e.g. NOx) in polluted urban areas by increasing both of transport and turbulent mixing, while the 'ozone cavity' there is efficiently refilled. When the velocity of the winds is greatly reduced (stagnant condition), the rate of ozone refilling by transport and turbulent mixing becomes considerably smaller than the rate of NOx titration and, as a result 'near-zero ozone concentrations' are found in the surface layer of the ABL. In this case, the main pathway of NOx loss is cut off and the accumulation of NOx reaches the highest level. So large-scale winds are an external independent variable in determining the abundance of ozone and NOx in the surface layer of the ABL in polluted urban areas.

In the case of Beijing, the winter monsoon is the strongest large-scale circulation in winter. When cold and strong northerly winds invade the region of Beijing, the stability of ABL is close to 'neutral' and turbulence in ABL is principally mechanical. During this period, high abundances of ozone are expected, even at night [5, 30]. Our regional chemical transport model reproduces nocturnal ozone enhancement events during the invasion of strong northerly winds that happened in January of 2019. In Section 3.2, the ozone increases during those events are quantified and the contributions of different atmospheric processes are assessed by a series of sensitivity tests using different estimates of the winds.

- **Question 2: What is the role of urban heating in controlling the fate of ozone and NOx during the day-to-night transition?**

In winter, the heating on building walls and roofs provides an important external energy input and modifies the energy balance of the earth surface. It affects the atmospheric stability of the layer immediately above the ground by changing the quantity and even the direction of sensible heat flux. During the day-to-night transition (sunset), urban heating competes with the energy loss associated with radiative cooling, and maintains an upward sensible heat flux until after sunset. Kuang et al. [31] has conducted a year-long observation of the energy balance for two different ground materials in Beijing, one is a forest park and the second one is a building roof covered with gray cement concrete. The results show that the sensible heat flux above the building roof remains directed upwards even after sunset in all seasons; in the winter season, the upward sensible heat flux lasts for 2 hours after sunset, while the sensible heat flux observed in the forest park decreases rapidly in the afternoon and becomes directed downward at sunset. With upward sensible heat flux occurring after sunset, the surface layer becomes thermally unstable and, to certain extent, a shallow convection layer is formed [19, 32, 33, 34]. Therefore, urban heating in winter is an important factor affecting turbulent fluxes of trace gases in the surface layer, especially during the day-to-night transition and during nighttime.

Without urban heating resolved in regional models, the calculated eddy diffusivity, which describes the turbulent exchanges in the ABL, drops suddenly to small values at the same time as the day-to-night transition [34]. The gases such as NOx that continue to be emitted at the surface therefore accumulate in the lowest layer of the model as they no longer disperse vertically. During the winter season, in highly polluted urban areas, NOx quickly titrates surface ozone; the concentration of this molecule, which is photo-chemically produced during the day, is therefore considerably reduced at the beginning of the night, and can remain abnormally low through the night. However, observations do not show the existence of these pronounced NOx peaks and the virtual disappearance of surface ozone as simulated by regional models during the day-to-night transition. We will therefore investigate this question in detail in Section 3.3.

- **Question 3: How does ozone respond to anthropogenic emissions?**

Emissions of pollutants provide the 'fuel' for boundary layer ozone chemistry. Anthropogenic emissions are the most variable and complex sources of pollutants due to the large temporal-spatial variability in the amplitude of these sources. This is the case, for example, of NOx, which is mainly emitted by anthropogenic sources (globally 77% of NOx emissions are of anthropogenic origin [35]). The anthropogenic emissions of pollutants are independent of atmospheric processes and consistently injected into atmosphere in polluted urban areas. In winter, the ozone behavior is closely related to the intensity of these NOx emissions.

In addition to high horizontal heterogeneity, anthropogenic emissions from certain sources are injected at different altitudes in the atmosphere. Industrial chimneys, for example, inject flue gases directly at a height of hundreds of meters. Emissions in urban

areas show regular diurnal and weekly patterns according to urban population activities, for example, traffic rush hours and impacts of weekends and holidays. For numerical modelling of atmospheric trace gases, gridded emission inventories, which include anthropogenic emission fluxes, are developed and published by specialized scientific groups. Anthropogenic emission fluxes (mass of certain pollutant per unit of area per unit of time) are derived by multiplying quantified human activities, which are documented normally in various statistical data (e.g. national statistical yearbook), and emission factor (mass of certain pollutant per unit of certain human activity) measured in field experiments. Emission inventories typically provide two-dimensional (2D) maps of emission fluxes for a city, a country, a continent or the whole earth on a yearly or monthly timescale. The vertical injection and diurnal/weekly variations in the emissions are usually not resolved in published emission inventories. Further, these inventories provide data at a horizontal resolution of typically 10-50 kilometers, which is not optimal for addressing city-scale questions. This study reproduces anthropogenic emissions in Beijing and its surrounding areas by resolving the complexities of the vertical injection, the diurnal/weekly variations and horizontal heterogeneity (downscaling) based on an existing global gridded emission inventory. Using the standard 2D emission fluxes from the original emission inventory in the model provides a baseline simulation, to which other simulations can be compared. This allows us to assess how the adoption of more complex formulations of the anthropogenic emissions affects the behavior of ozone and NOx in the atmosphere. This study is covered in Section 4.2, 4.3 and 4.4.

A real-world unexpected and unprecedented 'experiment' with vast emission reduction took place after the outbreak of the COVID-19 pandemic in Wuhan, China at the beginning of the year 2020. Almost the whole population in China was put into quarantine in order to contain the pandemic. Normal human life ceased suddenly in a few days. Automobiles stopped running on road, shopping malls were closed, factories had to partly or fully close due to lack of workers, airports were empty due to cancellation of 89% of flights [36]. Anthropogenic emissions of NOx, CO, sulfur dioxide (SO_2), VOCs etc. were subject to vast reductions [37, 38] and even disappeared from some reported sources, e.g. emissions in closed airports. After the outbreak of COVID-19, the concentrations of surface ozone in Northern China increased by a factor of 2 associated with a 53% reduction of NOx [39]. It is conceivable that reduced ozone titration by NOx caused the ozone concentration to increase. Interestingly, the response of ozone in Southern China was of opposite sign. Section 4.5 discusses the responses of ozone to the massive emission reduction in China during the COVID-19 pandemic by simulating two cases (with and without the application of reduction factors to emissions) using a regional chemical transport model.

1.6 Overview

The thesis is organized as follows: Chapter 2 provides a description of the region under consideration, and explains the regional model that is adopted for simulations in the studies of this thesis. Chapter 3 addresses the influence of large-scale winds (mechanical forcing) and the role of urban heat (thermal forcing) on the dynamics of

the boundary layer and on the distribution of key chemical species (questions 1 and 2 mentioned in Section 1.5). Chapter 4 discusses the response of ozone to different formulations of anthropogenic emissions and the perturbation of this chemical species during the lockdown following the outbreak of the COVID-19 pandemic in China (question 3 raised in Section 1.5). Finally, the major findings presented in this thesis are summarized in Chapter 5. An outlook for further investigations is also outlined in Chapter 6.

2 Studied region and model description

2.1 The city of Beijing

2.1.1 Topography and climate

Beijing, with over 21.7 million residents, is among the largest megacities in China. It is located in the northern part of the North China Plain (NCP) at an elevation of less than 50 meters above sea level (Figure 2-1). Apart from the municipality of Tianjin to the south-east, Beijing is bordered on all other sides by the densely populated province of Hebei (population 75 million) and by its hills and mountains (elevated up to 2000 meters above sea level) to the north and the west.

The meteorology in the region of Beijing is under the control of East Asia monsoon. In summer, the air temperature can be as high as 40 °C and thunder storms often occur when the warm and humid air blows from the southeast and the ocean during the season of summer monsoon. Winter is often cold (air temperature is as low as -10℃), dry and windy due to strong northerly winds originated from the cold-core Siberia-Mongolia High. Under the impact of global warming, both of annual maximum and minimum of observed surface air temperature increase by 0.387 ℃ and 0.271 ℃, respectively, from 1979 to 2021 in Beijing [40]. It has shown that the warming in urban areas is also attributed to rapid urbanization that accounts for 8-15% of warming trend in the region of Beijing-Tianjin-Hebei [41]. In the recent decade, light precipitations decrease and instead short-period extreme precipitations increase in the highly urbanized area of Beijing city [42, 43]. Locally, the mountain-plain breeze characterizes the diurnal wind in the region of Beijing. Therefore, during the daytime in winter, weak southern or southwestern winds dominate in the region (plain breeze against the northerly background winds). However, during winter nights, strong northern and north-eastern winds blow from mountains into the region (mountain breeze pro the northerly background winds). Figure 2-2 shows the background wind fields in winter and summer (upper row) and the mean local wind fields in daytime and night-time of January (lower row) in the region of NCP.

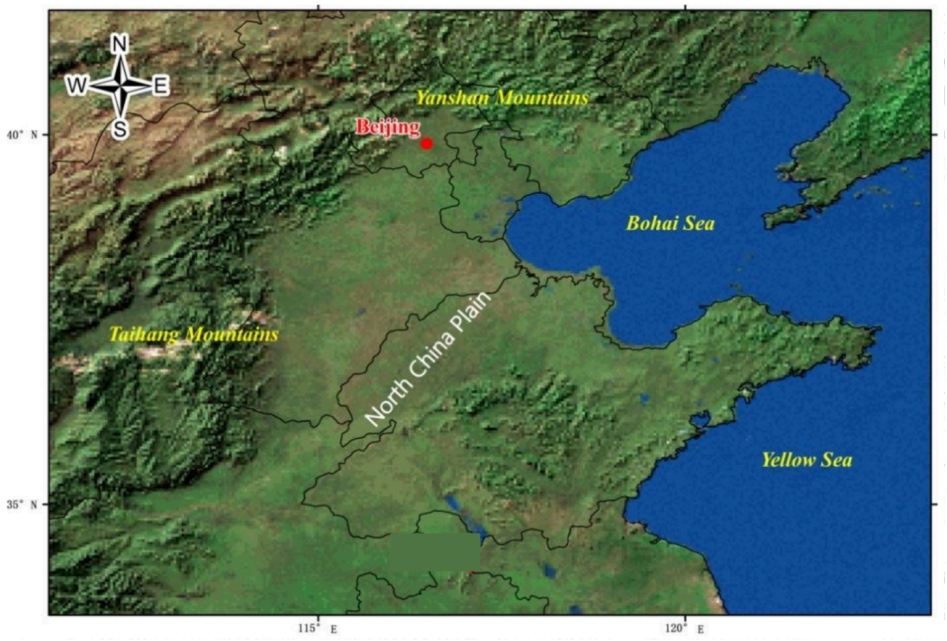

Figure 2-1. Terrain of the surroundings of Beijing [44].

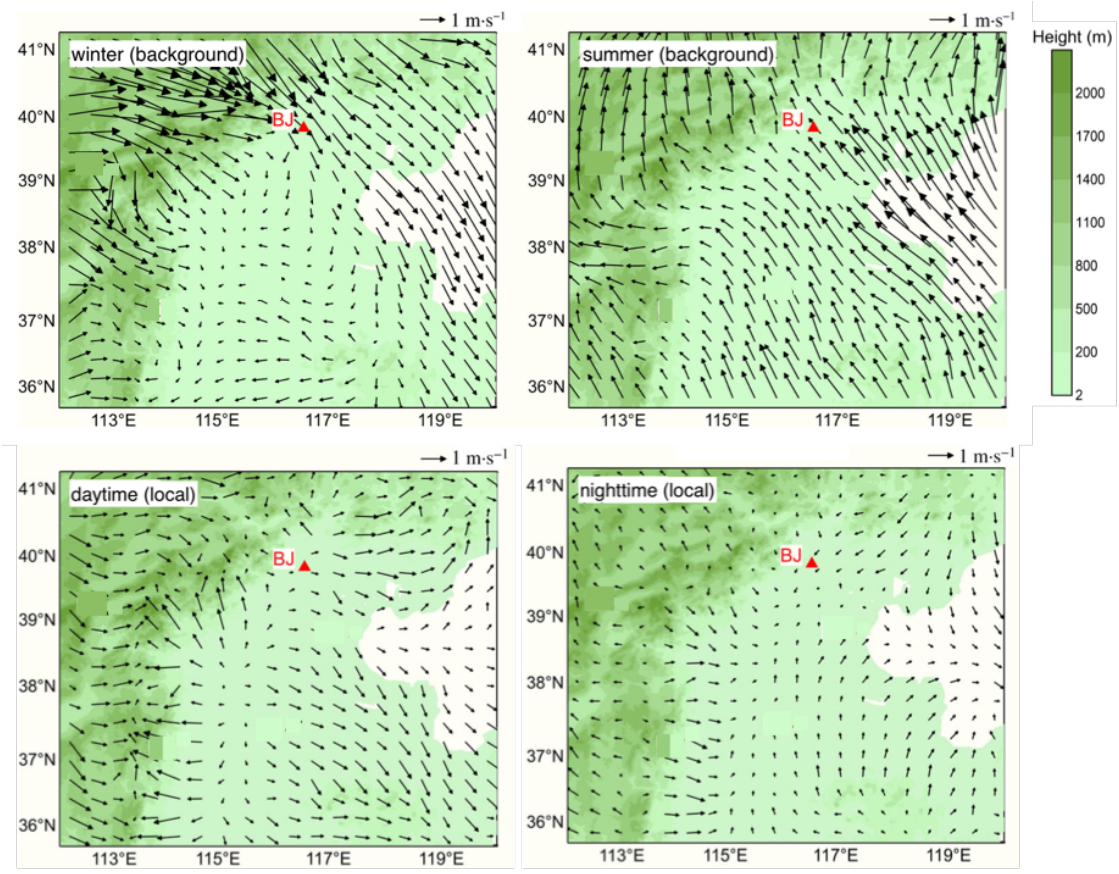

Figure 2-2. Monthly mean background wind fields in winter (January) and summer (July) (upper row) and monthly mean local wind field in daytime and night-time in January (lower row). The climatology period is from 2014 to 2020; red triangle marks out the city Beijing (BJ). Adapted from [45].

2.1.2 Air pollution in winter

Due to high anthropogenic emissions and a complex topography that favors the accumulation of pollutants, the Beijing region is often affected by extreme episodes of air pollution, particularly during the winter [46]. Aerosols, and in particular fine particulate matter $PM_{2.5}$ (with a diameter less than 2.5 micrometers), are the dominant air pollutants in Beijing in winter and often lead to 'haze' events [47]. The major component of $PM_{2.5}$ is secondary inorganic aerosols [48], which are closely associated with levels of ammonia (NH_3), NOx and SO_2 through the mechanism of heterogeneous chemistry. The levels of ozone during 'haze' events, which characterize wintertime, are relatively low due to low solar radiation and stagnant meteorological conditions, which favor the accumulation of NOx and depletion of ozone. But when northerly winds are enhanced, larger advective transport and turbulent mixing lead to the increase of ozone (as explained in Section 1.4.3), which is associated with higher wind speed, lower air temperature and lower levels of 'haze' pollutants, e.g. $PM_{2.5}$ and NOx etc. [28]. In the region of Beijing, the level of ozone is anti-correlated with 'haze' pollutants during wintertime.

In recent years, wintertime air pollution in eastern China has been mitigated since the Clean Air Actions were implemented by the government in 2013. In Beijing, 'haze' pollutants, e.g. NO_2, and CO in winter progressively decreased over the last decade, seen in Figure 2-3, due to strict emission control strategies. Large reductions were also found in SO_2 concentrations, which dropped by about 84% between 2014 and 2018 [49]. Due to the relation between ozone and NOx, the reduction of NOx corresponds to the increase of ozone [50, 51]. The surface ozone concentrations increased by 0.43±0.41 ppbv/year in Beijing from 2013 to 2020, with the largest increase of 1.12 ± 0.82 ppbv/year in winter [50].

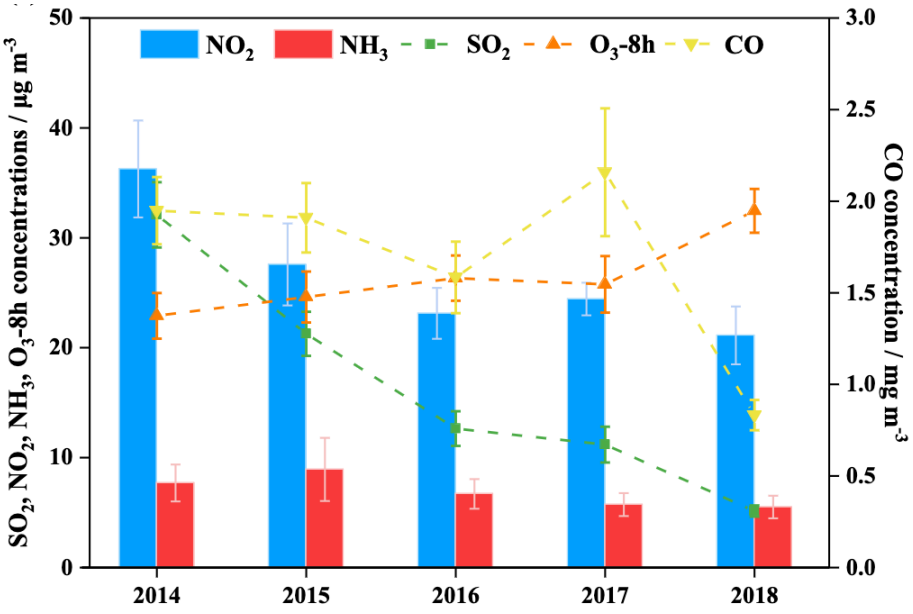

Figure 2-3. Monthly mean concentrations of observed surface NO_2, NH_3, SO_2, daily maximum of 8-h average of ozone (O_3-8h) and CO in Beijing in January from 2014 to 2018 [49].

Anthropogenic emission sources

The major difference of anthropogenic emissions between winter and summer in the city of Beijing is the increased residential emissions in winter. Figure 2-4 shows the fractions of emission sources contributing to certain pollutants in Beijing in January 2019. Residential sources account for one fifth of CO emissions, 19 % of NMVOCs emissions, 15% of NH_3 emissions and 6% of NOx emissions. By contrast, residential emissions are largely reduced in summer and only 3% of emissions of CO and NMVOCs are from residential sources (not shown). Regarding NOx emissions, the level of primary NOx is dominated by three non-residential emission sources with no big difference between winter and summer. In winter, the industrial, transportation and energy sources almost equally contribute to NOx emissions (33%, 30% and 31%, respectively). The source of industrial processes contributes to over half emissions of CO and NMVOCs. And the agricultural emissions dominate total emissions of NH_3 (63%).

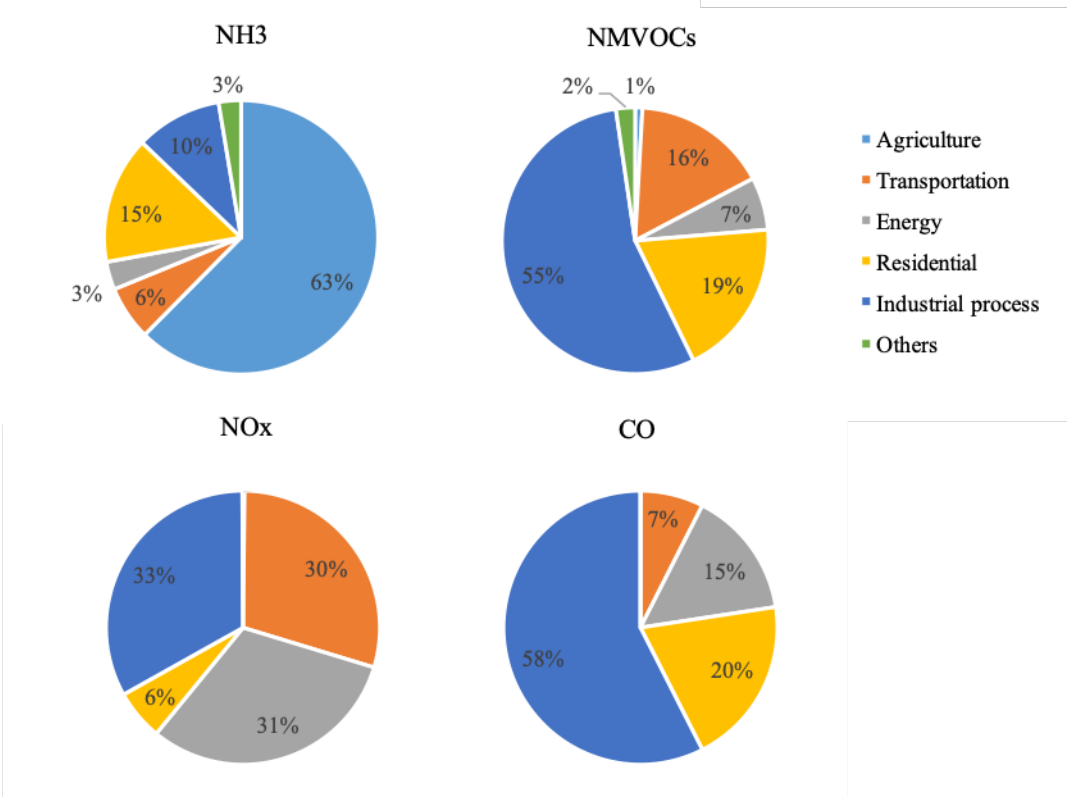

Figure 2-4. Fraction of emissions of NH_3, NMVOC (non-methane VOCs), NOx and CO from six emission sources in Beijing in January 2019. Total monthly emissions are 0.01 Tg (Terragram) for NH_3, 0.19 Tg for NMVOCs, 0.15 Tg for NOx and 1.62 Tg for CO. Data source: the global emission inventory CAMS-GLOB-ANT-v5.3 [52] (downloaded from https://permalink.aeris-data.fr/CAMS-GLOB-ANT, Last access: 2023-10-03). The source 'Energy' includes power generation by power plants, fugitives and refineries. Solvent use is included in 'Industrial process'. 'Transportation' includes road and off-road transportation and ships. 'Others' include solid and water waste.

2.1.3 Urban heat island effect

Impervious surfaces in urban areas, e.g. buildings and roads etc., tend to emit extra heat into the aloft atmosphere, leading to higher surface air temperature than suburban and rural areas, which are instead covered with more vegetation. The warmer urban area forms an urban heat island (UHI). The effect of UHI is largest at night in winter [53, 54]. The observed UHI intensity of Beijing in winter night is as high as 4.3 ℃ [54]. The major cause of UHI effect is anthropogenic heat (AH) emissions in urban areas. Due to increased heating demands, AH emissions are the highest in winter. In Beijing during winter season, the mean intensity of AH is as high as 135 W/m^2, which is mainly linked to commercial and industrial areas in the metropolitan area of Beijing [55]. The large AH intensity in winter of Beijing is even comparable or larger than solar radiation, which indicates the important role of AH in modifying urban climate, especially ABL stability, during cold wintertime.

2.2 Regional chemical transport model: WRF-Chem

2.2.1 Introduction to the model

The Weather Research and Forecasting model coupled with Chemistry (WRF-Chem) is a non-hydrostatic, limited area, regional chemical transport model [56, 57, 58]. It simulates meteorology and chemistry in the troposphere and lower stratosphere. Over a specific region, WRF-Chem downscales simulations by applying several nested domains with increased horizontal resolutions. Boundary and initial conditions of the meteorological and chemical simulations in WRF-Chem are originated from global fields either simulated or assimilated by global models. Chemistry is online-coupled with meteorological calculation in WRF-Chem. So it is very suitable for investigating meteorology-chemistry feedbacks on local to regional scales, although it could be computationally expensive and less flexible for conducting ensemble modelling. The version WRF-Chem v4.1.2 is used in this study (source code: https://github.com/wrf-model/WRF/tree/release-v4.1.2).

In calculations of meteorology in WRF-Chem, apart from regional-scale dynamics, some subgrid processes are parameterized, e.g. convective clouds and turbulence in ABL. Mainly tropospheric chemistry is calculated in the model by solving chemical kinetics with the tool Kinetic PreProcessor (KPP). The fates of trace gases and aerosols are simulated by resolving multiple processes, e.g. emissions, transport, dry/wet removal and chemistry (including gas-phase and heterogeneous chemistry, cloud chemistry and photolysis). The chemical system also gives feedbacks to meteorological processes, e.g. aerosol radiation effect and microphysics in the cloud formation. More information of WRF-Chem can be found on the official website: https://ruc.noaa.gov/wrf/wrf-chem/.

With a chemical transport model, the contributions of all relevant processes to the evolution of chemicals are calculated and a comprehensive view of realistic evolution of chemicals is depicted in the model. An investigation of the interplay among

different processes gives new knowledge of behavior of chemicals in the real atmosphere.

2.2.2 Model configuration

Model frame and domain

The simulations of regional models are normally framed in a flat synoptic-scale box, which has a much larger horizontal extent than the vertical extent. Figure 2-5 shows a schematic representation of the model framework used in this study. The horizontal span is an area with a size of 2400km x 1700km centred on the city of Beijing. Vertically, the top model layer is fixed at the constant pressure level 50hPa (approximately the altitude 20km). Three model domains are defined with spatial resolutions of 18 km, 6 km and 2 km, respectively (Figure 2-6). The number of vertical model layers for three domains is 37 or 47, which are used for specific purposes in ensemble simulations conducted in this study (Section 2.2.3). Below 1600 m, the setting of total 47 model layers has 20 layers with the first-layer at the altitude of 23m, while the setting of total 37 layers has only 10 layers with the first-layer at the altitude of 46m. The level altitudes of model layers below 1600m are shown in Table A-1. Domain 1 communicates with external lateral boundary conditions to transport air mass in or out. Domain 2 and Domain 3 take, respectively, the calculations of Domain 1 and Domain 2 as lateral boundary conditions, while they also give feedbacks to their upper domains. Time steps used in simulations of three domains are 120, 60 and 20 seconds, respectively. The ABL possesses 0.25%~10% of the vertical part of the model.

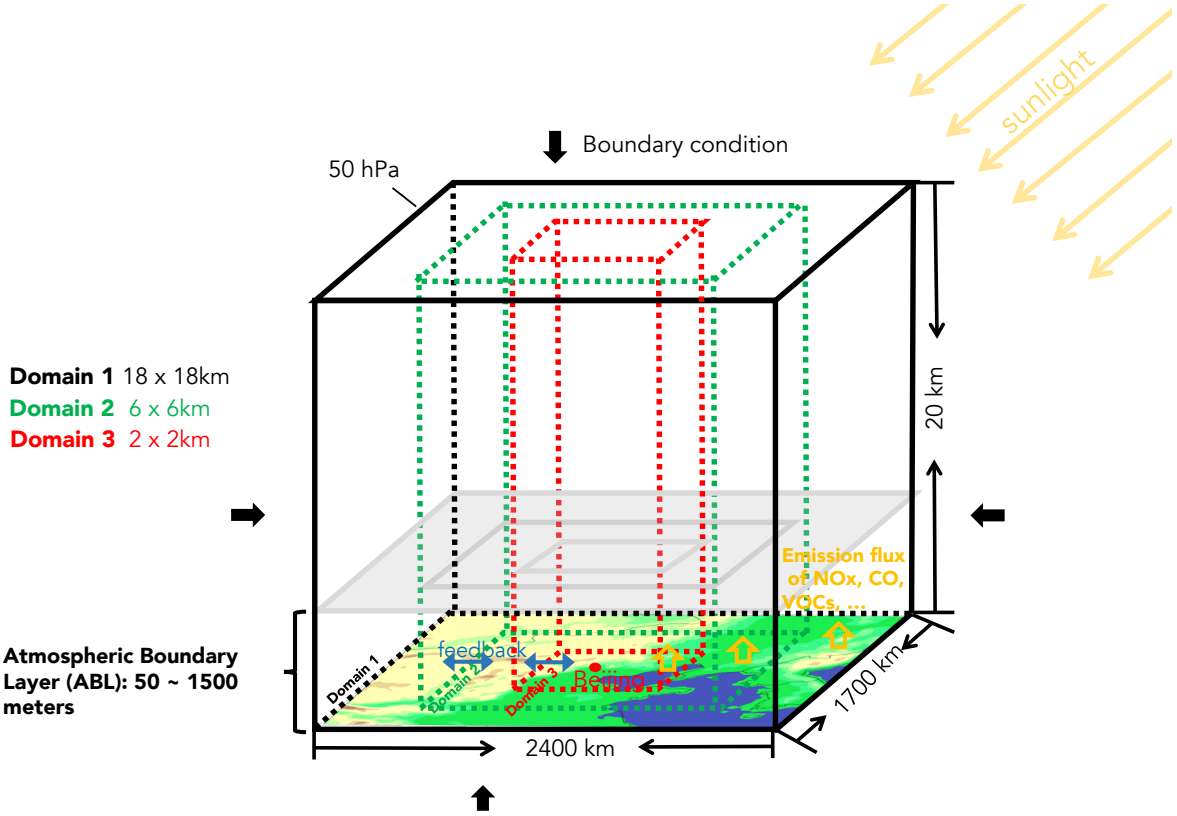

Figure 2-5. The framework of the model. Vertical scale is enlarged for better observation.

Boundary and initial conditions

In order to simulate different meteorology in the model, the lateral boundary and initial conditions for calculations of meteorology are from two global datasets: the final analysis (FNL) dataset by the National Centers for Environmental Prediction (NCEP) [59] and the fifth-generation atmospheric reanalysis of global climate (ERA5) by the European Center for Medium-Range Weather Forecasts (ECWMF) [60]. The top layer of the model has no fluxes of air mass and therefore no need for boundary conditions. The bottom boundary conditions for the meteorological calculations are surface fluxes of energy and water calculated by the coupled land surface model, which needs initial conditions of soil parameters that has been included in the meteorological initial conditions.

Chemistry calculations have separate inputs of initial and boundary conditions. The chemical initial and lateral boundary conditions are from global simulations with the Community Atmosphere Model with Chemistry (CAM-Chem) [61]. In order to account for stratospheric intrusions, which significantly affect tropospheric chemistry, upper boundary conditions of eight chemical species, i.e. methane (CH_4), CO, ozone, NOx, H_2O, HNO_3, N_2O_5 and nitrous oxide (N_2O), are provided with climatological concentrations. Between the pressure level 50hPa and the tropopause, the concentrations of the eight chemical species are relaxed to the climatological values. The chemical bottom conditions are natural and anthropogenic emission fluxes that are separately calculated.

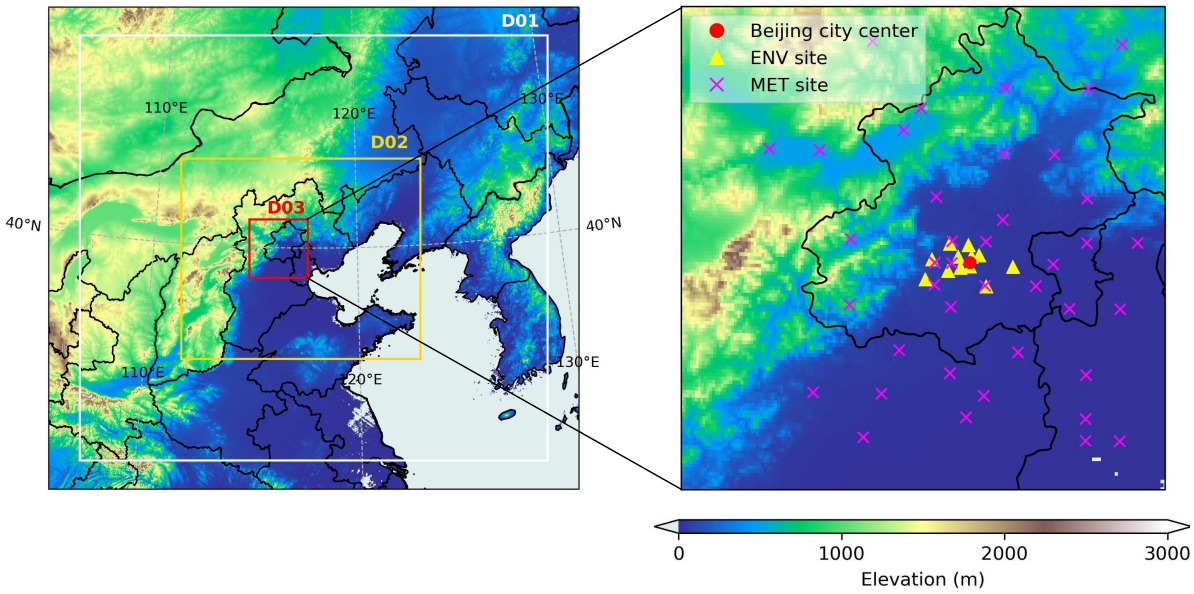

Figure 2-6. Model domains with topography as the background. ENV site - environmental observation site; MET site - meteorological observation site.

Meteorological nudging

In order to reinforce the influence of meteorological driving fields (as boundary and initial conditions for meteorology) on the mesoscale simulations in this study, a technic 'nudging', also called Newtonian relaxation [62], is used by adding a very small

adjustment, calculated from meteorological driving fields, to the tendencies of meteorological variables, which are, in this study, temperature, humidity and wind. In simulations with nudging, calculations of temperature, humidity and wind are adjusted at same time intervals as the driving datasets, i.e. 6-hourly in simulations driven by FNL and hourly in simulations driven by ERA5. The adjustment term is based on the difference of simulated values and values in driving fields. To constrain the intensity of nudging, this study uses 0.0006 as the nudging factor, which represents the relative magnitude of the adjustment term to the total tendency. Variations of nudging settings among ensemble simulations are detailed in Section 2.2.3.

Physical and chemical parameterizations

The microphysics parameterization based on the Thompson-Grauple scheme [63] and the cumulus parameterization based on the New Grell scheme [64, 65] are adopted because they are suitable for high-resolution simulations. The radiation in the model is calculated by the Rapid Radiative Transfer Model for General Circulation Models (RRTMG) [66].

For the parameterization of planetary boundary layer (PBL, interchangeable with ABL), the first-order non-local PBL scheme from Yonsei University (YSU) [67] is used in this study. Combining the YSU scheme, the unified Noah land surface model [68] and the revised MM5 Monin-Obukhov surface layer scheme [69] together account for land-atmosphere interactions in the model.
The mechanism of gas-phase and heterogeneous chemistries is from the Model for Ozone and Related chemical Tracers for tropospheric chemistry (MOZART-T1) [70], which is coupled with the Goddard Chemistry Aerosol Radiation and Transport (GOCART) model [71]. The photolysis of chemical compounds is parameterized by the Tropospheric Ultraviolet and Visible (TUV) Radiation Model [72]. All physical and chemical parameterizations are summarized in Table 2-1.

Table 2-1. A summary of physical and chemical schemes.

	Parameterization	Scheme
Physical	Microphysics	Thompson graupel scheme
	Cumulus	New Grell scheme
	Radiation	RRTMG
	Planetary boundary layer	YSU
	Surface layer	Revised MM5 Monin-Obukhov scheme
	Land surface	Unified Noah land-surface model
Chemical	Chemical mechanism	MOZART-T1
	Aerosol	GOCART
	Photolysis	TUV

Emissions

There are many complex processes contributing to emissions of trace gases and aerosols in the atmosphere. These processes are divided into natural sources dominating emissions in the rural areas and anthropogenic sources dominating in the urban areas.

In this study, anthropogenic emissions are from the global gridded emission inventory, CAMS-GLOB-ANT v4.2-R1.1 (in short CAMS, downloaded from https://eccad3.sedoo.fr/, last accessed: 2023-02-04). This is a harmonized version between the CAMS-GLOB-ANT v4.2 and the Chinese emissions inventory from the Multi-resolution Emission Inventory model for Climate and air pollution research (MEIC) [73]. Previous studies indicate that the MEIC inventory well represents anthropogenic emissions in China [74, 75]. Emission sources are categorized into twelve sectors in the CAMS inventory (Table A-2). Chemical species contributing to anthropogenic emissions in the model are five inorganic compounds, i.e. NO, NO_2, CO, NH_3 and SO_2, four aerosol species, i.e. organic carbon (OC), black carbon (BC), $PM_{2.5}$ and PM_{10} (particulate matter with a diameter less than 10 micrometers) and twenty-two VOCs species (listed in Table A-4). A mapping from the original chemical species in the CAMS inventory to the primary chemical species defined in the chemical scheme MOZART-T1 is shown in Table A-3. The emission fluxes ($kg/(m^2 \cdot s)$) for NOx in the CAMS inventory is considered as NO. Conventionally, 90% (mole fraction) of NOx emissions is assigned as NO and 10% as NO_2.

Emissions of particulate matter ($PM_{2.5}$ and PM_{10}) are not included in the CAMS inventory and therefore estimated separately. The BC and OC emissions, part of PMs, at a given location are assumed to be in a fixed ratio to the emissions of $PM_{2.5}$ and PM_{10} at the same location. In a study by Schaap et al. [76], BC emissions over Europe is generated by its fixed fraction to sub-micro particles emissions. Zheng et al. [73] has produced anthropogenic emissions of BC, OC, $PM_{2.5}$ and PM_{10} for years of 2010-2017 in China with a bottom-up methodology. The ratio of yearly total emissions of BC+OC to $PM_{2.5}$ and PM_{10} is 0.42-0.45 and 0.30-0.33, respectively. For a ratio of yearly total emissions of $PM_{2.5}$ to PM_{10}, a range of 0.72-0.75 is derived.

Here an auxiliary emissions inventory from Emissions Database for Global Atmospheric Research (EDGAR) version 5 [77, 78, 79, 80] (https://edgar.jrc.ec.europa.eu/dataset_ap50, last access: 2021-09-21) for the year of 2015, is used to generate ratios of $PM_{2.5}$/(BC+OC), $PM_{10}/PM_{2.5}$ and PM_{10}/(BC+OC) and to derive $PM_{2.5}$ and PM_{10} emissions for 2019 from the CAMS BC and OC emissions (Table 2-2). To avoid repetitive counting of aerosol masses, the calculated emissions of $PM_{2.5}$ and PM_{10} exclude masses of BC and OC and additionally emissions of PM_{10} exclude masses of $PM_{2.5}$. Due to different sector nomenclature of EDGAR and CAMS, harmonization of sectors of the two inventories is conducted (shown in Table A-5). Eight sectors in the inventory EDGAR v5 in the year of 2015 are chosen to account for six sectors, i.e. power generation (ene), residential (res), on-road transportation (tro), off-road transportation (tnr), industrial (ind) and shipping (shp), in the CAMS inventory.

Figure 2-7 shows the fraction of emissions from different sources for NOx, CO, BC, OC, NMVOC, SO_2, NH_3, $PM_{2.5}$ and PM_{10} averaged over the simulation periods in Beijing. It is clear that emissions in Beijing are mainly generated by transportation, residential and industrial activities. Especially CO and BC are mainly emitted by transportation. The residential source contributes to most of OC emissions, while industrial emissions dominate the total emissions of NOx, NMVOC and SO_2.

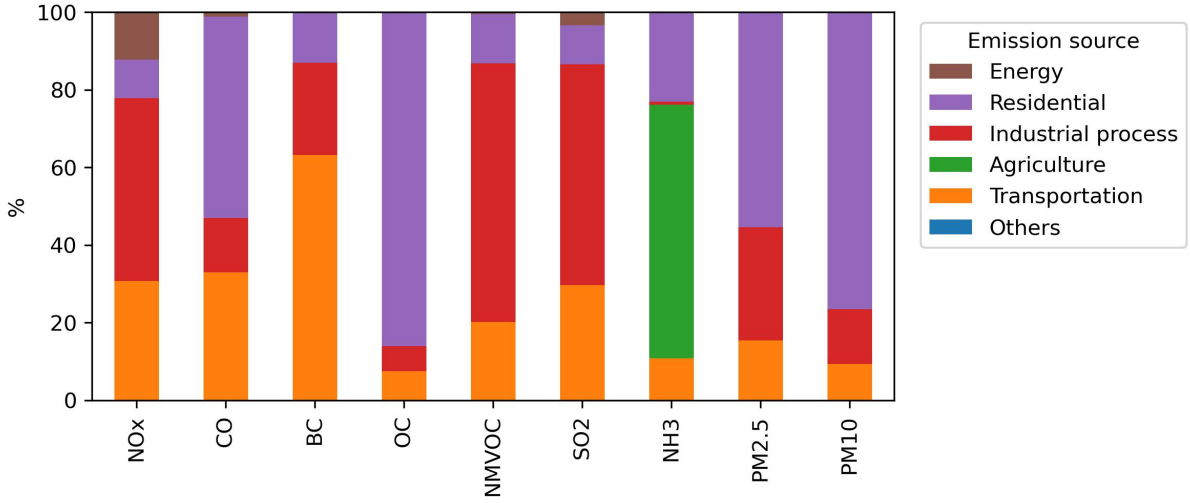

Figure 2-7. Fraction of emissions from different sources in Beijing. The sector lumping is same as Figure 2-4.

Apart from anthropogenic emissions, the emissions from biomass burning (wildfire) are also activated in the model. First, the model reads in daily fire emissions from the Fire INventory of NCAR Version 2.2 (FINNv2.2) [81]. Then a plume rise model in WRF-Chem [82] is called every 15 minutes during the simulation to generate effective heights of biomass burning emissions. Biogenic emissions are online-calculated by the Model of Emissions of Gases and Aerosols from Nature (MEGAN) [83]. In addition, dust and sea salt emissions are handled by the model GOCART.

2.2.3 Numerical experiments

In total, 13 simulations are conducted in this thesis to fulfill different purposes of studies detailed in Chapter 3 and Chapter 4. Here a comprehensive summary of all simulations is given. Two time periods during wintertime are chosen. One is a two-week period in January of 2019, extending from 12 to 22 of 2019 after 3 days of spin-up period. The second time period is from January 1 to February 29, 2020, with 10 days of spin-up time. The first time period represents typical winter conditions in the region of Beijing in recent years. During the first time period, there is no precipitation and the weather is either sunny or cloudy. A strong cold front, accompanied by a drop in temperature, begins in the afternoon of January 14 and lasts throughout the day of January 15 in 2019. The second time period is chosen as a special case and covers the outbreak of COVID-19 in China in winter 2020. Two experiments including one control case and one test case are conducted in the second time period to evaluate the effect of vast emission reduction during the nation-wide lockdown on ambient abundance of ozone and NOx. The model configuration regarding simulations with the second time

period slightly differs from aforementioned one and is specifically described in Section 4.5. And the related experiments are also found in that section.

Summary of experiments

Except two experiments for the special case regarding COVID-19, 11 experiments for January of 2019 are shown in Table 2-3. Two control simulations, named as CTL1 and CTL2, are mainly differentiated by the number of vertical layers adopted under 1.6 km altitude in the model configuration. The vertical setting with 37 layers is for CTL1 with ten layers under 1.6km and 47 layers for CTL2 with twenty layers under 1.6km. The names of all other experiments start always with their corresponding control cases. In order to investigate ozone behavior under different meteorological forcing, four nudging experiments are designed based on the control case CTL1. Different meteorological driving fields and nudging strategies are used in nudging simulations, which is detailed in Section 3.2. To test the sensitivity of ozone budget to urban heat, the ground temperature is artificially elevated by 3 Kelvin degree in the experiment CTL1_heat. The last four experiment regarding emission redistribution are designed to test different ways of emission allocation including vertical injection of emissions (CTL1_vert and CTL2_vert), emission variation with time (CTL2_vert_t) and emission downscaling (CTL1_dwns).

Validation of model results

The validation of meteorological fields covers the whole area of Domain 3. Routine observations of in total 42 weather stations operated by China Meteorological Administration (CMA) (fuchsia cross in Figure 2-6) are used to validate temperature, wind and relative humidity. Surface ozone and NO_2 are validated only in the city of Beijing, with observations from 12 environmental stations operated by the Beijing Municipal Ecological and Environmental Monitoring Center (yellow triangles in Figure 2-6). The environmental stations cover an area ranging from 39.80°N to 39.99°N in latitude and from 116.15°E to 116.66°N in longitude. The 12 environmental stations have a relatively good representativeness of adjacent areas as they are classified as 'environmental assessment sites' by the operation department and none of them are close to traffic-busy roads or emission hot spots. The simulations of meteorological and environmental (chemical species) variables are linearly interpolated to the locations of the observation stations.

In addition, four validation metrics are used, i.e. mean bias (MB), vector wind differences (VMD), root-mean-square errors (RMSE) and correlation coefficients. The equations for calculating MB, VMD and RMSE are detailed in Appendix. The first three metrics represent the deviation of the model simulation from the observation. The last metric is to show the correlation of the trends between simulation and observation. First of all, the Pearson correlation coefficients (r) of trends at every station are calculated. Then the maximum correlation coefficient r_{max} measures the best performance of the model at individual stations. And another quantity is the number of stations at which the correlation coefficient of trends is larger than a threshold,

which is 0.8 for meteorological variables or 0.65 for environmental variables (the significance level is $p<0.05$).

The meteorological variables for validation are 2-m temperature (T2, °C), 10-m wind speed (WS10, m/s) and relative humidity (RH, %). And ozone (ppbv) and NO_2 (ppbv) are environmental variables for validation. The calculated quantities of metrics mentioned above are shown in Table 2-4 for meteorological variables and Table 2-5 for environmental variables.

Surface temperature and wind are overestimated in all experiments. Two experiments with meteorological driving fields from ERA5 (CTL1_era and CTL1_era_w) simulate the best representation of RH. This is related to the inherent property of the reanalysis dataset ERA5, which is produced by assimilating observation data from various sources including surface routine observations. The best representations of ozone and NO_2 are simulated by the experiment CTL1_heat.

Table 2-2. The generation of emissions of $PM_{2.5}$ and PM_{10} from EDGAR v5 to CAMS. The specie names in EDGAR v5 are represented by lower case letters and those in CAMS by bold upper case letters.

	$\mathrm{bc} + \mathrm{oc} < \mathrm{pm2.5}$	$\mathrm{pm2.5} \leq \mathrm{bc} + \mathrm{oc} < \mathrm{pm10}$	$\mathrm{bc} + \mathrm{oc} \geq \mathrm{pm10}$
$\mathbf{PM2.5} =$	$(\boldsymbol{BC} + \boldsymbol{OC}) \cdot (factor1^{a} - 1)$	0	0
$\mathbf{PM10} =$	$[(\boldsymbol{BC} + \boldsymbol{OC}) \cdot factor1^{a}] \cdot (factor2^{b} - 1)$	$(\boldsymbol{BC} + \boldsymbol{OC}) \cdot (factor3^{c} - 1)$	0

[a] $factor1 = \frac{pm2.5}{bc+oc}$; [b] $factor2 = \frac{pm10}{pm2.5}$; [c] $facotr3 = \frac{pm10}{bc+oc}$

Table 2-3. A summary of 11 model experiments

Groups	Simulations	Layers under 1.6km	Meteorological driving field	Nudging	Urban heat	Vertical injection of emissions	Emission variation with time	Downscaled emissions
Control	CTL1	10	FNL	no	no	no	no	no
	CTL2	**20**	FNL	no	no	no	no	no
Nudging	CTL1_fnl	10	FNL	yes^	no	no	no	no
	CTL1_fnl_w	10	FNL	yes*	no	no	no	no
	CTL1_era	10	ERA5	yes^	no	no	no	no
	CTL1_era_w	10	ERA5	yes*	no	no	no	no
Urban heat	CTL1_heat	10	FNL	no	yes	no	no	no
Emission redistribution	CTL1_vert	10	FNL	no	no	yes	no	no
	CTL2_vert	**20**	FNL	no	no	yes	no	no
	CTL2_vert_t	**20**	FNL	no	no	yes	yes	no
	CTL1_dwns	10	FNL	no	no	no	no	yes

^ Wind is nudged in all model layers

* Wind is nudged above PBL and above 600m

Table 2-4. Validation of meteorological variables, 2-m temperature (T2, °C), 10-m wind speed (WS10, m/s) and relative humidity (RH, %) of 11 experiments shown in Table 2-3 with observations of 41 weather stations. Statistics: mean, mean bias (MB) (in brackets), root-mean-square error of vector wind difference (VMD), root-mean-square deviation (RMSE), maximum correlation coefficient (r_{max}) ($p < 0.05$) of trends at individual observation stations and the number of stations at which the correlation coefficient of trends is larger than the threshold 0.8 (in brackets).

	Mean (MB)			**VMD**	**RMSE**			**r_{max} (stations with $r > 0.8$)**		
	T2	**WS10**	**RH**		**T2**	**WS10**	**RH**	**T2**	**WS10**	**RH**
OBS	-2.14 (-)	1.68 (-)	32 (-)	-	-	-	-	-	-	-
CTL1	-1.30 (0.84)	3.38 (1.70)	28 (-4)	3.39	3.30	2.69	17	0.92 (32)	0.73 (0)	0.87 (9)
CTL2	-1.42 (0.73)	3.36 (1.68)	29 (-3)	3.38	3.21	2.66	16	0.94 (33)	0.72 (0)	0.87 (11)
CTL1_fnl	-2.07 (0.07)	2.43 (0.75)	24 (-8)	2.10	2.93	1.56	17	0.93 (38)	0.84 (3)	0.87 (18)
CTL1_fnl_w	-1.78 (0.36)	3.43 (1.75)	23 (-9)	3.14	2.88	2.50	17	0.93 (40)	0.80 (1)	0.87 (21)
CTL1_era	-2.05 (0.09)	2.42 (0.74)	34 (2)	2.16	2.73	1.61	11	0.96 (39)	0.88 (2)	0.94 (40)
CTL1_era_w	-1.66 (0.47)	3.63 (1.95)	33 (1)	3.41	2.79	2.76	11	0.96 (40)	0.77 (0)	0.94 (39)
CTL1_heat	-0.53 (1.61)	3.50 (1.83)	26 (-6)	3.43	3.73	2.76	19	0.93 (24)	0.75 (0)	0.83 (3)
CTL1_vert	-1.30 (0.84)	3.38 (1.70)	28 (-4)	3.39	3.27	2.69	17	0.93 (32)	0.73 (0)	0.87 (10)
CTL2_vert	-1.42 (0.73)	3.36 (1.68)	29 (-3)	3.38	3.21	2.66	16	0.94 (33)	0.72 (0)	0.87 (11)
CTL2_vert_t	-1.42 (0.73)	3.36 (1.68)	29 (-3)	3.38	3.21	2.66	16	0.94 (33)	0.72 (0)	0.87 (12)
CTL1_dwns	-1.30 (0.84)	3.38 (1.70)	28 (-4)	3.39	3.27	2.69	17	0.92 (32)	0.73 (0)	0.87 (9)

Table 2-5. same as Table 2-4 but for NO_2 (ppbv) and ozone (O_3, ppbv) with observations of 12 environmental stations. The threshold of correlation coefficients of trends is 0.65 here.

	mean (MB)		**RMSE**		$\mathbf{r_{max}}$ **(stations with** $r > 0.65$**)**	
	NO_2	**O_3**	**NO_2**	**O_3**	**NO_2**	**O_3**
OBS	30.85 (-)	12.72 (-)	-	-	-	-
CTL1	43.39 (12.54)	10.04 (-2.68)	22.30	10.19	0.63 (0)	0.78(11)
CTL2	45.67 (14.82)	8.75 (-3.98)	23.70	10.54	0.62 (0)	0.76 (10)
CTL1_fnl	49.57 (18.73)	9.97 (-2.76)	29.92	10.63	0.67 (1)	0.78 (8)
CTL1_fnl_w	40.67 (9.82)	12.56 (-0.16)	19.40	10.12	0.73 (6)	0.80 (11)
CTL1_era	43.54 (12.69)	9.81 (-2.91)	21.73	10.57	0.68 (1)	0.78 (8)
CTL1_era_w	38.71 (7.86)	13.87 (1.15)	18.84	11.14	0.70 (4)	0.74 (11)
CTL1_heat	34.86 (4.01)	16.13 (3.41)	16.72	9.94	0.71 (7)	0.87 (12)
CTL1_vert	35.75 (4.91)	13.94 (1.22)	18.50	10.68	0.62 (0)	0.78(9)
CTL2_vert	37.88 (7.03)	12.47 (-0.25)	19.03	10.39	0.63 (0)	0.8 (9)
CTL2_vert_t	36.22 (5.37)	13.81 (1.09)	20.21	11.95	0.59 (0)	0.71 (3)
CTL1_dwns	40.73 (9.89)	11.78 (-0.94)	22.23	10.49	0.57 (0)	0.75 (10)

3 Winter ozone behavior influenced by two boundary layer forcing factors

3.1 Introduction

Large-scale synoptic wind, as the mechanical forcing on the local boundary layer turbulences, increases the transport of pollutants, which is an increase in ozone and a decrease in NOx in the urban area of Beijing, as explained in Section 1.4.3, and also provides mechanical energy to the maintenance of turbulences in the boundary layer, which increases the downward turbulent transport of ozone [84, 26, 27]. Under 'static stable' conditions, normally at night, the intensity of large-scale wind competes with the thermal suppression in the boundary layer. When northerly synoptic wind invades the urban area of Beijing, the mechanical force for turbulence generated by the large-scale wind overpowers the thermal suppression and ozone is enhanced by both increases of transport and turbulent mixing. The study in Section 3.2 differentiates wind simulations in the boundary layer by nudging wind from two kinds of meteorological fields into different portions of the vertical model layers. By observing different ozone behavior under distinct representations of winds, the main characteristics of ozone evolutions in Beijing's urban areas with the winter monsoon background are identified.

Urban heat is an important thermal forcing factor affecting the boundary layer stability, especially at night during wintertime. It exerts forcing to the surface layer by perturbing the surface energy flux and generating 'anthropogenic convection' in urban areas. The created convection increases the diffusion of emitted pollutants in the surface layer and generates a downward turbulent flux of ozone [85]. Due to the demand for heating and cold temperatures in winter season, urban heat flux (also called anthropogenic heat flux in literatures) is the highest in the winter nights in Beijing [55]. The intense urban heat flux modifies the evolution of the winter boundary layer during the day-to-night transition. In the model simulation, simulating without resolving the urban heat in wintertime leads to fast increases of emitted pollutants and very low level of ozone during the day-to-night transition due to the high stability of the boundary layer. However, carrying out observations, it is seen that NOx increase is a smooth curve with less intensity. Section 3.3 investigates how the model simulations of NOx and ozone during the day-to-night transition are improved by including the influence of urban heat.

3.2 Influence of large-scale wind

3.2.1 Different representations of meteorology

Different representations of meteorology are achieved with the application of nudging. Four experiments are designed with nudging adjustment. Two of them are driven by the meteorological fields from FNL and the other two by the meteorological

fields from ERA5. Between the two experiments with the same meteorological driving fields, the wind is nudged, either on all model layers, or above the 7th layer (about 600m) and also the top of PBL. All four simulations are based on the control case CTL1. Detailed descriptions are shown in Table 3-1. Other nudging settings are kept the same. Apart from wind, temperature and moisture from the meteorological driving fields are nudged on all model layers in the four nudging experiments. The nudging coefficient is set as 0.0006 for all three nudging variables.

Table 3-1. Experiments with different representations of meteorology

Experiments	Meteorological driving field	Nudging wind in all layers*	Nudging wind above PBL and above 600m*
CTL1	FNL	-	-
CTL1_fnl	FNL	yes	no
CTL1_fnl_w	FNL	no	yes
CTL1_era	ERA5	yes	no
CTL1_era_w	ERA5	no	yes

* The sign '-' means that there is no calculation of nudging

3.2.2 During the invasion of synoptic northerly wind

Synoptic northerly wind (strong, cold and dry) is the background wind in the region of Beijing during wintertime. It often brings thick and large-scale cold air masses into the region and dominates the winter boundary layer. When northerly wind invades, the boundary layer becomes neutral and the development of turbulences is mainly controlled by the mechanical force (wind). Figure 3-1 shows a time-height cross section of potential temperature overlaid with the horizontal wind (white arrows) and the height of the boundary layer (PBLH, black line) in Beijing simulated in the control experiment (CTL1). Two events of northerly wind invasion may be identified with the features of strong northerly wind and thick cold layer. The first event (E1), the strongest one, is from 18:00, January 14 to 15:00, January 15. And the second event (E2) has less intensity, occurring from 21:00, January 19 and 6:00, January 20. The two events mainly cover nighttime. They are also associated with enhanced PBLH at night, e.g. in E1 the PBL reaches over 1000m at sunset. Another association with the northerly wind invasion event is the fast increase of the boundary layer ozone shown in Figure 3-1b.

The elevated concentrations of ozone at night during E1 and E2 can be as high as the daytime maximum. In observations of surface ozone in Beijing (lower panel in Figure 3-2), the nighttime maximum of ozone is 29 ppbv (21:00, January 14) in E1 and 31 ppbv (01:00, January 20) in E2. There are in total five events of nighttime ozone enhancement (NOE) found in the observations of ozone, but only three of them (January 15, January 19 and January 20) with higher intensities are captured by the model. Two of them are during events E1 and E2, identified as periods of strong northerly wind invasion. And the third one, during 00:00-08:00 on January 19, is associated with a weaker northerly wind invasion, as shown in Figure 3-1.

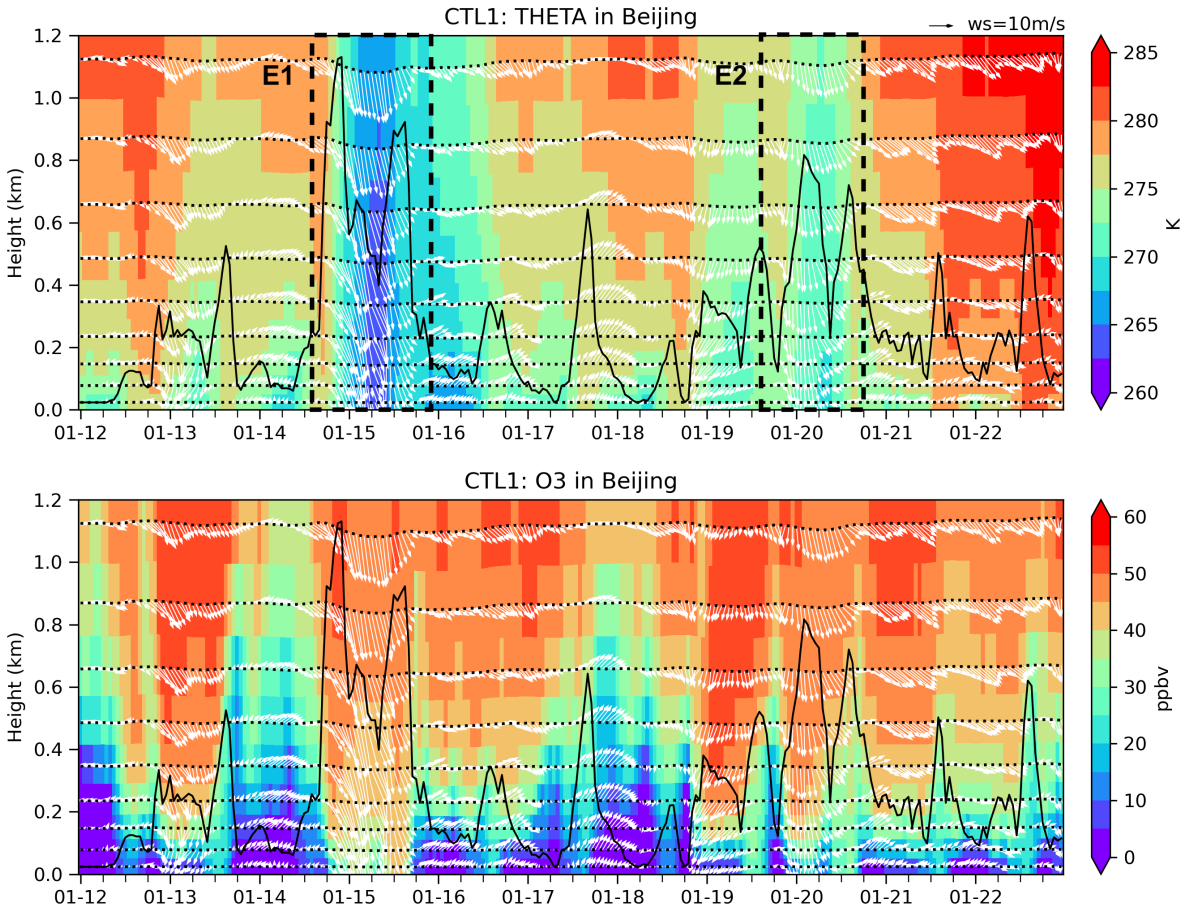

Figure 3-1. Time-height cross section of potential temperature (THETA) and ozone in Beijing simulated by the control run CTL1. Black solid lines in both plots are the height of the boundary layer (PBLH). Horizontal dotted black lines are the middle heights of model layers. White arrows on model layers are horizontal wind vectors. Boxes with bold dotted lines are two events (E1 and E2) of northerly wind invasion.

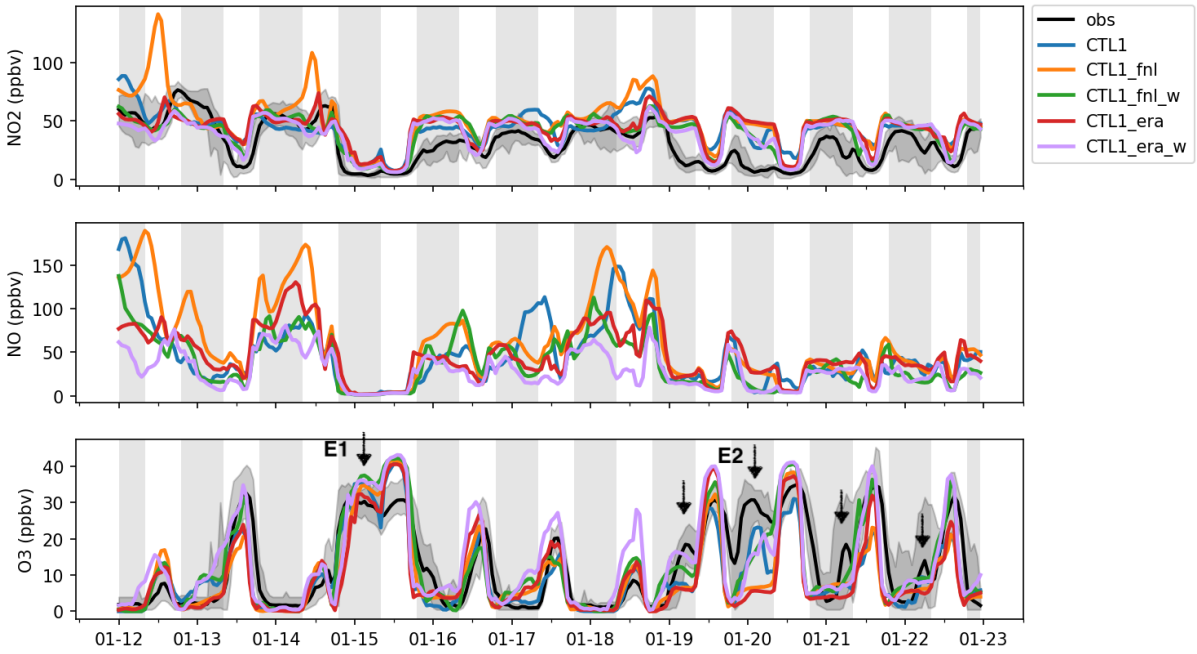

Figure 3-2. Time series of NO_2, NO and ozone in the observation (black line) and five experiments. Shadows under the black lines are the range of observations among stations. Vertical light grey rectangles mark night-time periods (19:00-08:00). Black arrows point out five events of night-time ozone enhancement.

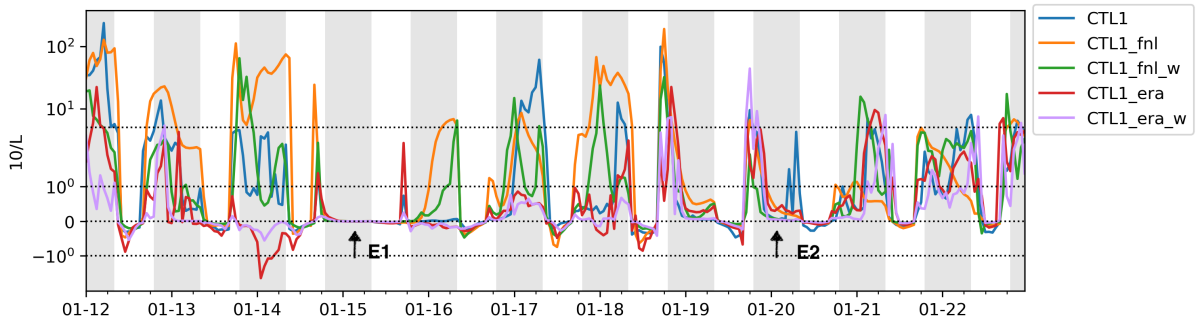

Figure 3-3. Time series of the stability index 10/L simulated in five experiments. L represents the Monin-Obuhov length calculated with the equation in (1-12). Two black arrows point two events of strong northerly wind invasion. Four horizontal dotted lines are at the y-axis levels of -1, 1 and 5.

During the invasion of strong northerly wind (E1 and E2), the northerly wind dominates the nocturnal boundary layer, in which the static stability becomes neutral. Figure 3-3 shows the time series of a stability index, namely 10/L, composed with Monin-Obuhov length (L) simulated by the model. The quantity 10/L is chosen because it is calculated with only parameters in the surface layer (friction velocity and sensible heat flux) and represents well the surface layer stability. A positive 10/L represents the 'stable' condition, and a negative one represents the 'unstable' condition. The 'neutral' condition is associated with a zero value of 10/L. During E1 and E2, the stability in simulations that capture NOE (CTL1, CTL1_fnl_w and CTL1_era_w) is 'neutral' ($10/L \approx 0$). The eddy diffusivity K simulated during these two events is significantly elevated (Figure 3-5), especially during E1. It is indicated that the strong mechanical force imposed by strong northerly wind increases the turbulent mixing of ozone with an intensity that can be larger than the turbulent mixing of the daytime boundary.

In summary, ozone is enhanced when strong northerly wind invades; it is normally initiated at night. In observation, ozone increases by a factor of 1.9 (+19 ppbv) and NO_2 drops by 84% (-44 ppbv) during the initiation period (the first 3 hours) of the strongest northerly wind invasion (E1). The maximum ozone level during NOE (night-time ozone enhancement) can be higher than daytime ozone maximum. The significantly enhanced mechanical mixing accounts for NOE. It is implied that ozone enhancement at night during strong northerly wind invasion could be over the alert level of ozone, if the background ozone level is high.

3.3.3 Close relationship between wind and ozone in winter

Winds contribute to both turbulent mixing and transport of chemicals. The NOE in two events of strong northerly wind invasion (E1 and E2) is partly accounted for by the ozone transported from the north mountainous area to the urban area of Beijing by the strong northerly wind. Due to the ozone 'cavity' (lower ozone level than the surrounding area) across the day in the urban area of Beijing, the transport of either northerly or southerly wind always contributes to the increase of ozone. Wind always transports ozone into the urban area and mostly transports NOx out of it during winter time. Figure 3-4 shows the contribution of transport to the ozone budget in Beijing simulated in five experiments. The permeant positive values (blue line) indicate the positive contribution of advective transport to ozone level increase. The contribution of the northerly wind to ozone level increase has a higher intensity than that of the southerly wind. Most of the time, the transport contributes to the NOx decrease in the urban area of Beijing (Figure A-1) except for some short periods in the daytime with southerly wind, which brings NOx plume from southern polluted regions.

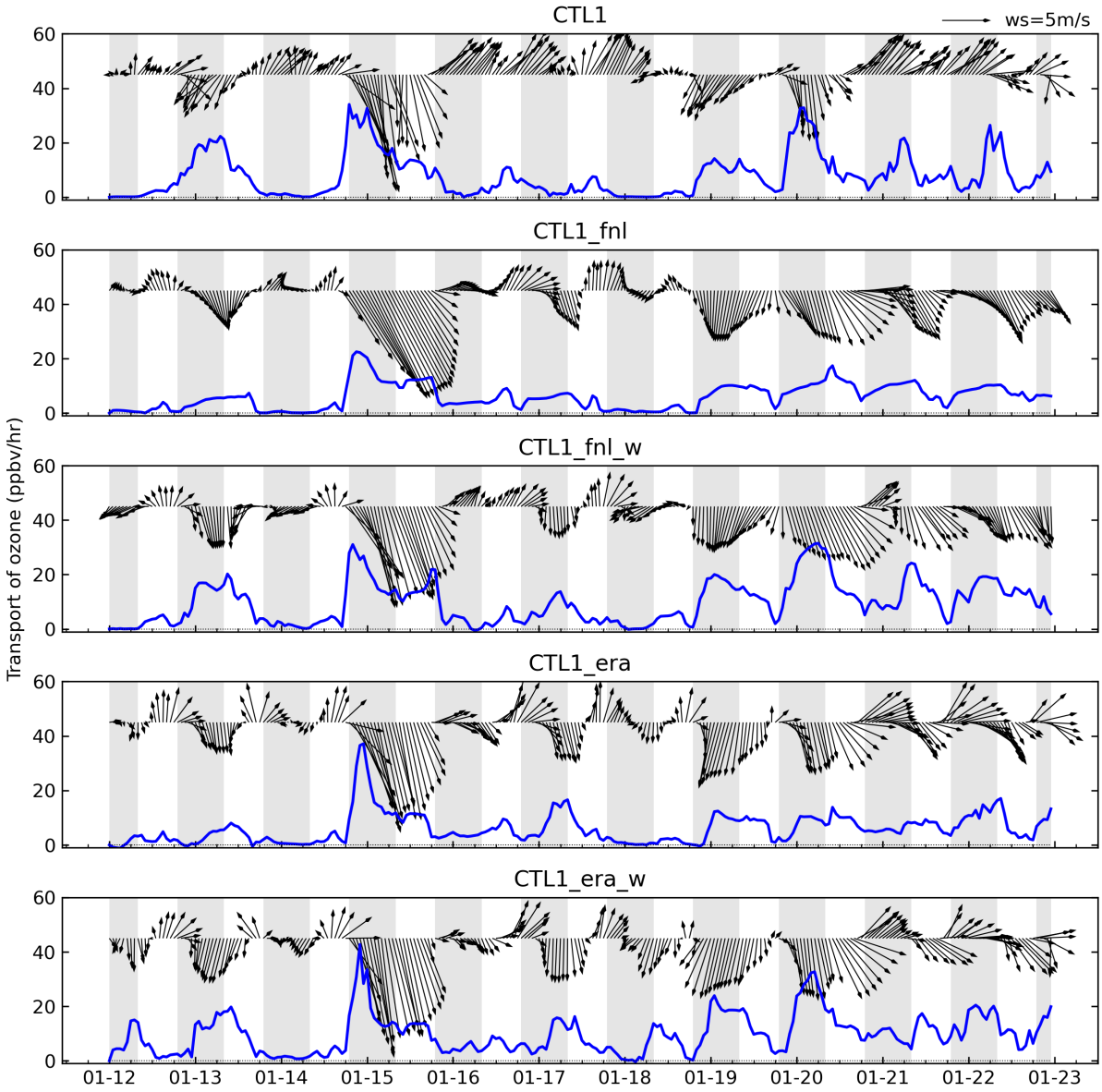

Figure 3-4. Time series of the contribution of transport to ozone budget (blue line) and wind vectors (black arrows) in the surface layer in Beijing simulated in five experiments. Shading areas represent night-time 19:00-08:00 (LCT).

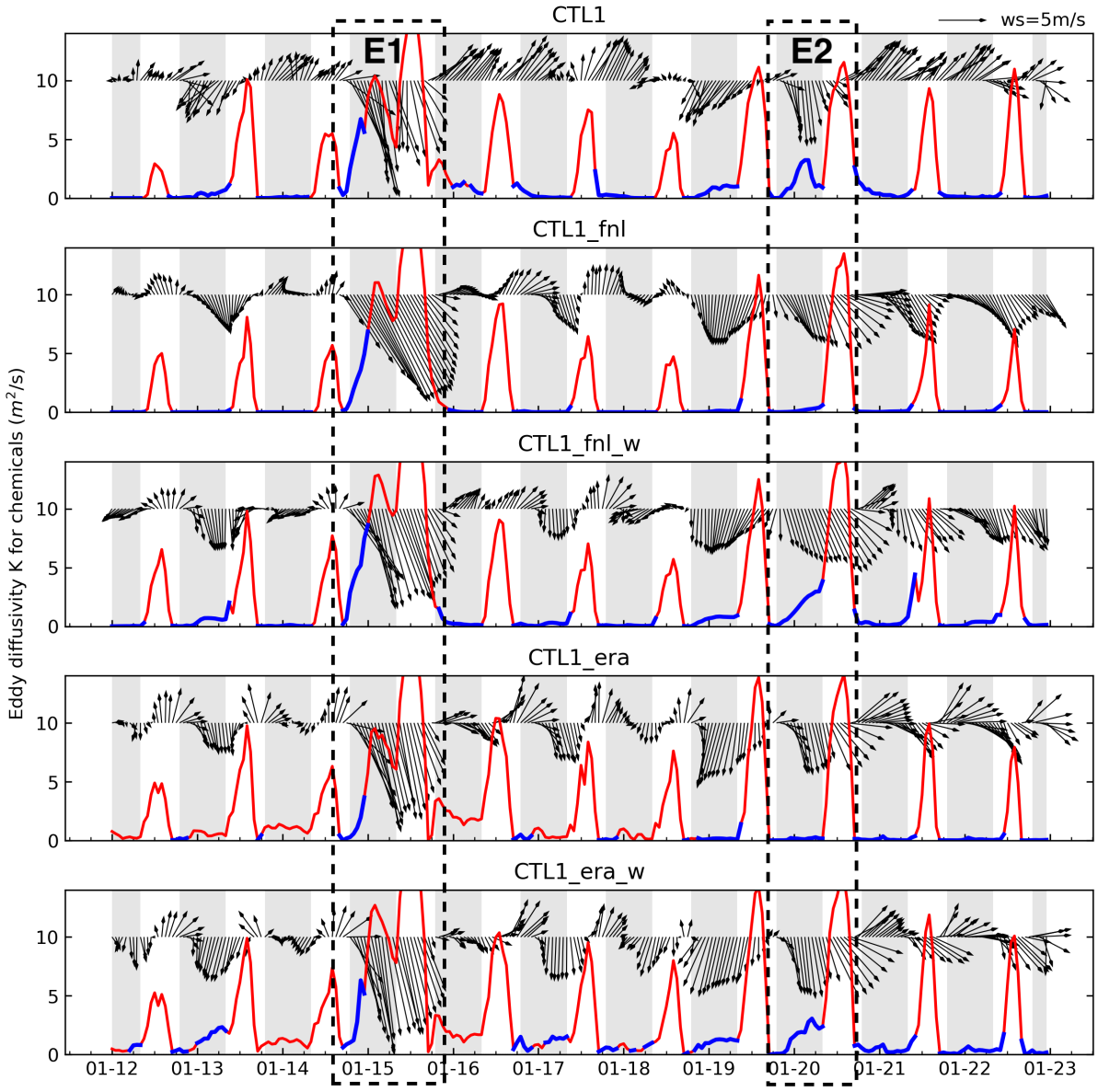

Figure 3-5. Time series of eddy diffusivity K for chemicals in the surface layer simulated by five experiments. Two long rectangle boxes with dashed lines show periods of two events of strong northerly wind invasion. The red parts of the lines represent K values with upward sensible heat flux (unstable) and blue parts with downward sensible heat flux (stable). Shading areas represent night-time 19:00-08:00 (LCT).

The winter nocturnal boundary layer is prone to be 'stable' as indicated in Figure 3-3. The prevailing northerly wind is a potential source of turbulences in the stable boundary layer during wintertime. So the generation of turbulences in the stable boundary layer has to rely on the mechanical force of wind overpowering the thermal suppression. The eddy diffusivity K for chemicals in the surface layer is a indicator of the turbulent mixing of chemicals. Figure 3-5 shows the eddy diffusivity K for chemicals in the surface layer simulated in five experiments. Blue parts of the lines mark out hours with negative (downward) sensible heat flux, which indicates thermal suppression or 'static stable' condition in the surface layer. A time series of sensible heat flux in Beijing simulated by five experiments is shown in Figure A-2.

In the 'neutral' periods (strong northerly wind invasion), mechanical force (wind) overpowers the thermal suppression and increases the turbulent mixing of chemicals. During the period of E1 (dashed-line box in Figure 3-5), the early evening is 'stable' (blue line). But eddy diffusivity K rapidly increase in all five experiments due to the large mechanical energy provided by the strong northerly wind. In the budgets of chemicals, both the transport and turbulent mixing of ozone and NO_2 significantly increase, while the chemical loss of NO rapidly increases due to increased ozone (Figure A-3). During the period of E2 with less intensity of northerly wind invasion, the increase of eddy diffusivity K is much weaker and is only simulated in the control experiment (CTL1) and experiments with wind nudged at higher altitudes (CTL1_fnl_w, CTL1_era_w). Next, the reason for still weak turbulent mixing under strong forcing of northerly wind, simulated by experiments with full-layer wind nudging (CTL1_fnl, CTL1_era), is investigated.

The wind shear (vertical difference of horizontal wind) represents the mechanical force for turbulence generation in the boundary layer. Figure 3-6 is the longitude-height cross section of the horizontal wind averaged over the period of E2. It is seen that simulations with full layer wind nudging (CTL1_fnl, CTL1_era) generate very weak wind shear (2nd and 4th panel of Figure 3-6) and, therefore, a near-zero K value (2nd and 4th panel of Figure 3-5) under 'stable' condition in the urban area of Beijing. However, when nudging wind at higher altitudes (CTL1_fnl_w, CTL1_era_w), wind speed around the top of the boundary layer significantly increase and low level jet (strong wind shear) with prevailing northerly wind is formed there (3rd and 5th panel of Figure 3-6), which effectively overcome the thermal suppression and generate a larger K value (3rd and 5th panel of Figure 3-5). Even though the advective transport of ozone increases, NOE is still not captured over the period of E2 in experiments with full-layer wind nudging (CTL1_fnl and CTL1_era in 3rd panel of Figure 3-2). Another similar case that occurred on the previous day is shown in Figure A-4. It is indicated that the turbulent mixing in the boundary layer mainly controls the occurrence of NOE, because the boundary layer dynamics, reproduced by the PBL scheme in the model, are indispensable to the increase of the downward turbulent fluxes of mass (ozone) and momentum in the boundary layer.

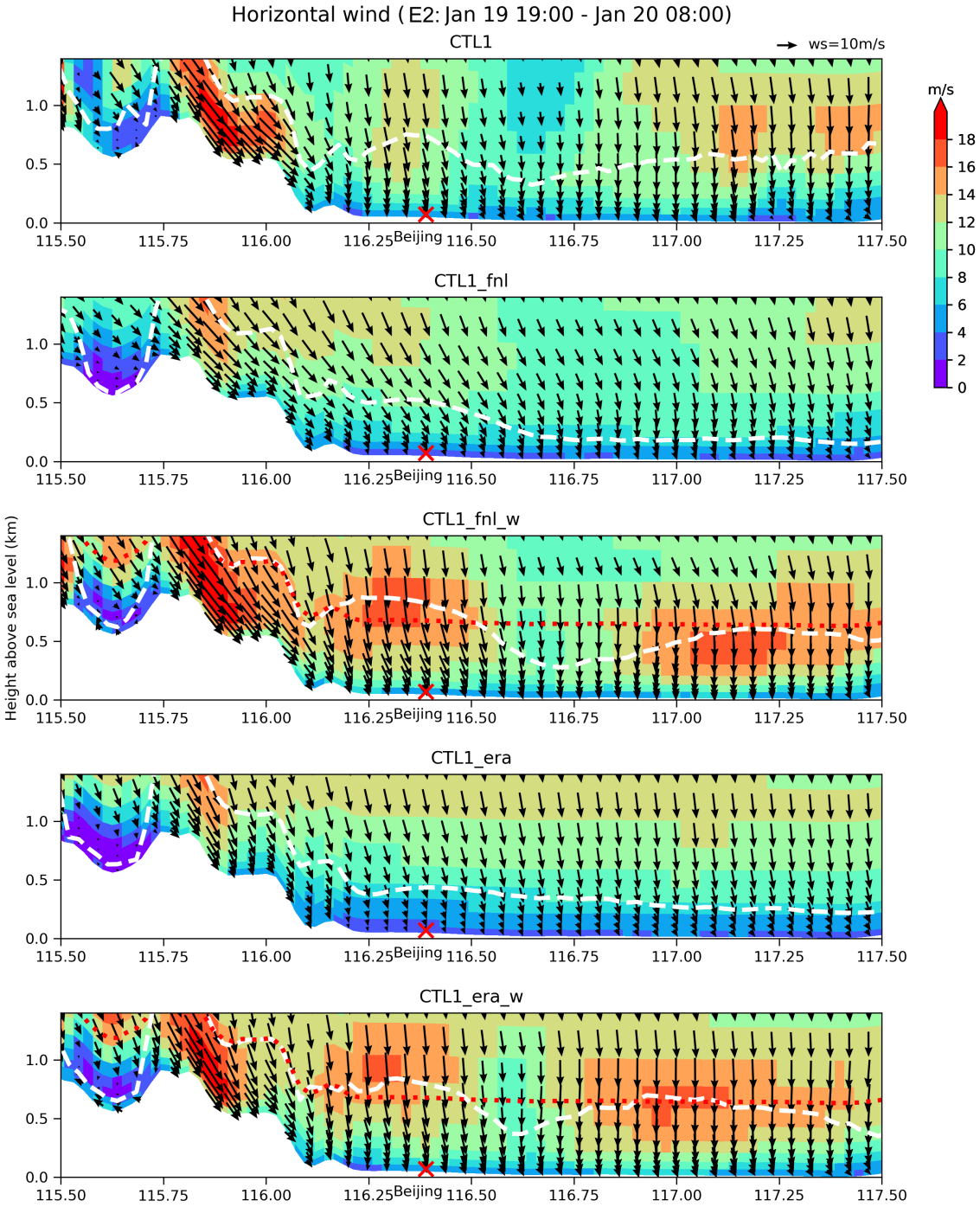

Figure 3-6. Longitude-height cross section of horizontal wind (shading is the wind speed and black arrow is the wind vector) simulated in the period of E2 by five experiments. White dashed line is the PBLH and red dotted line marks the height of 600m above the ground. The location of Beijing is marked by a red cross. The latitude is 39.92N.

It is implied that the high momentum at higher altitudes, in simulations with full-layer wind nudging (CTL1_fnl, CTL1_era), cannot be transported downward to the boundary layer by turbulent mixing efficiently because wind nudging in the boundary layer smooths the vertical difference of horizontal wind and hinders the generation of turbulence. Nudging wind at higher altitudes (CTL1_fnl_w, CTL1_era_w), however, simulates better boundary layer wind, especially low level jet at night and enhanced wind shear, which generates more turbulent mixing in the boundary layer. A good representation of the local wind is important to the simulation of turbulence intensity, which controls the diffusion of emitted pollutants and the vertical fluxes of ozone.

When the boundary layer is very stable (strong thermal suppression), very weak wind in the surface layer leads to stagnant conditions (ceased or very weak turbulence) and, therefore, fast accumulation of NOx, in the extreme case NOx rockets even by a factor of 2 and ozone disappears in the urban ozone 'cavity'. The extreme case is simulated by the experiment CTL1_fnl (orange line in the upper panel of Figure 3-2). Three NOx peaks are captured, respectively on January 12, January 14 and January 18. First, NO peaks at night and a NO_2 peak follows in the next daytime. Figure 3-7 is the 24-hour variation of horizontal wind of different model layers on January 12, simulated by CTL1_fnl. Very stable and stagnant boundary layer is simulated at night, and the daytime PBLH is only 200m. It assembles a 'chamber' with continuous NOx emissions, most of which is NO (the fraction of NO in NOx emission is set as 0.9). Fast accumulation of NO leads to a rocketing peak of NO at night, when ozone almost disappears. After sunrise, increased turbulent mixing brings ozone into the 'chamber' and results in a NO_2 peak and reduction of NO by fast conversion from NO to NO_2. The weakening of both turbulent mixing and transport in the extremely stable and stagnant boundary layer could lead to the dramatic increase of NO and the disappearance of ozone.

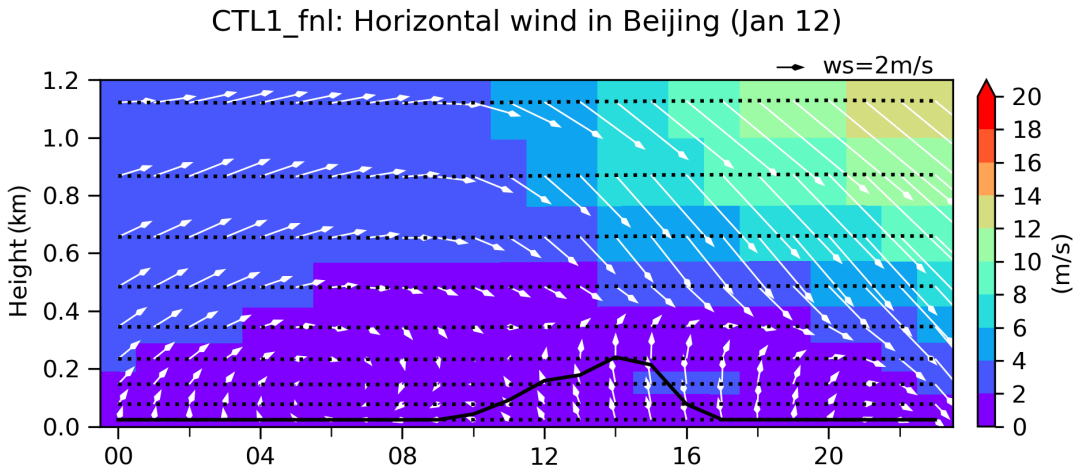

Figure 3-7. Hour-height cross section of horizontal wind (shading is the wind speed and white arrows are the wind vectors) on the day of January 12 simulated by CTL1_fnl. The black solid line is PBLH.

In summary, wind always contributes to the increase of surface ozone in the urban area of Beijing by turbulent mixing and advective transport. The northerly wind has more intense effect on the surface ozone increase than the southerly wind. Even with the increase of advective transport of surface ozone during the period of E2, experiments with full-layer wind nudging fail to capture NOE, because the weak turbulent mixing of surface ozone is generated at night by underestimated wind shear, especially low level jet. In contrast, NOE is reproduced in experiments without wind nudging in PBL, which better represent local wind dynamics. It is indicated that the increased PBL turbulent mixing influenced by large-scale wind (mechanical force) is the major process that accounts for the occurrence of NOE in the surface layer. The extremely stable and stagnant conditions are simulated by experiments with full-layer wind nudging, in which NOx significantly accumulates with an unrealistic peak and ozone disappears at night in the surface layer.

3.3 The role of urban heat during the day-to-night transition

3.3.1 The surface layer

Energy balance of the surface layer

The energy fluxes of a flat ground surface include four components: the net radiation flux Q_*, the sensible heat flux Q_H, the latent heat flux Q_E and the energy storage Q_G under the ground (Figure 3-8a). Among them, the sensible heat flux Q_H represents the direct heat conduction from the ground to the atmosphere usually during the daytime or from the atmosphere to the ground at night. In dry and cold winters, it is the major energy source of atmospheric buoyancy, generating air masses' up-motion and creating turbulences. Solar radiation is the only external energy input in the balance.

In the urban area, energy balance is counted in a volume, including the urban canopy [33] (Figure 3-8b). On the top of the volume, Q_*, Q_H and Q_E keep same but Q_G is replaced by more complex energy fluxes. ΔQ_A is the net heat flux transported by wind and ΔQ_S is heat storage in the urban surface material, e.g. buildings, roads and trees. At last, Q_F is the anthropogenic heat accounting for another external energy input to the urban canopy volume. Even though solar radiation is gone at night, Q_F can still maintain a positive Q_H and leads to unstable boundary layer. Observations have shown that the nocturnal sensible heat flux near the ground surface always stays positive in the urban area of Beijing [86], and is also observed in other megacities, such as London [87].

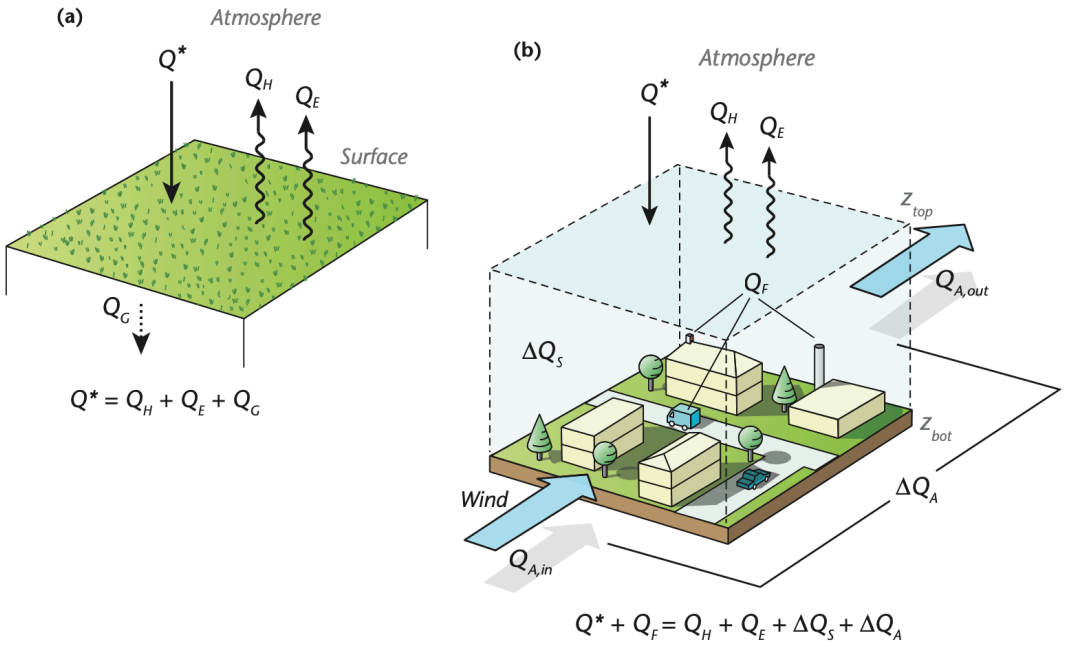

Figure 3-8. Energy balance of the ground surface (a) and a volume of urban canopy layer (b) [33].

Parameterizations of the surface layer

Processes in the surface layer are parameterized mainly with three models, i.e. land surface model, surface layer model and PBL model. They work together to simulate the eddy diffusivity K_h for heat, which is at the end used by the chemistry model to calculate the turbulent mixing of chemicals (Figure 3-9). First, the surface layer model and land surface layer model interact with the radiation model (not shown) to get the net radiation input. Then, the surface layer model calculates the exchange coefficients for heat and momentum (C_{hs} and C_{ms}) for the land surface model to calculate the sensible heat flux Q_H and latent heat flux Q_E, which are input to the PBL model. At the same time, the ground temperature T_s, also as an output of the land surface model, is used by the surface layer model to calculate the bulk Richardson number BR. The sign of BR (positive for stable, negative for unstable) is a stability indicator used by the PBL model to choose the parameterization of K that is designed for two conditions, 'stable' and 'unstable'. The calculation of K also considers similarity functions (ψ_m and ψ_h) and friction velocity u_*, which are also calculated by the surface layer model. The atmospheric state variables u, θ and q influenced by the PBL model are used in the calculation of surface layer model. The effect of urban heat is initiated with the increase of T_s in this study, which then might change the atmospheric stability and lead to the increase of K_h.

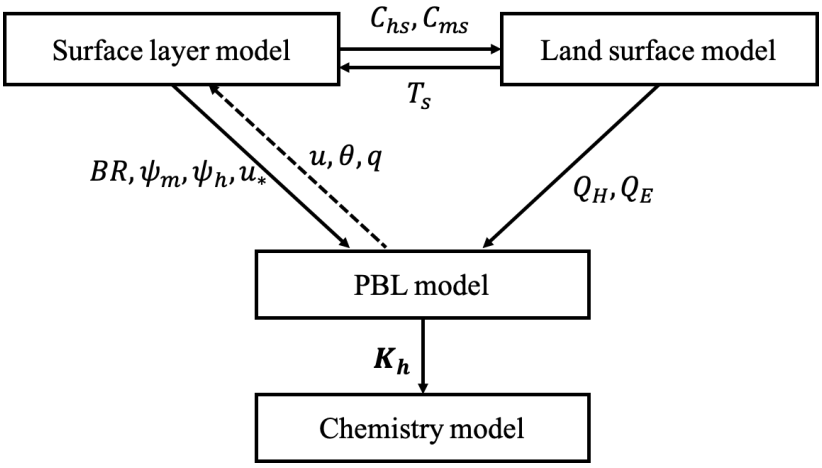

Figure 3-9. The related models in WRF-Chem used for the calculation of eddy diffusivity K_h that is later used by the chemistry model. C_{hs} and C_{ms} are exchange coefficients for heat and momentum. T_s is ground temperature. BR is bulk Richardson number. ψ_m and ψ_h are integrated similarity functions. u_* is friction velocity. u, θ and q are wind speed, potential temperature and water mixing ratio, which are not directly calculated but influenced by the PBL model.

3.3.2 Simulations of ozone and NOx during the day-to-night transition

The study of this section is based on the drafted paper shown below.

> **Shi, X.**, Deroubaix, A., Brasseur, G. P. (2023). Simulation of day-to-night transition of NOx and ozone in the boundary layer (draft).

Experiments

Five experiments are designed to investigate the sensitivity of NOx and ozone to different model formulations during the day-to-night transition. They are summarized in Table 3-2. The experiment CTL1_vert with anthropogenic emissions distributed vertically up to 500m is intended to simulate the NOx and ozone concentrations with less intense surface pollution emissions. The experiment CTL1_heat is to test the sensitivity of turbulent mixing of pollutants during the day-to-night transition to the urban heat effect. In order to look at the model behavior under different meteorological forcing, two experiments, CTL1_fnl_w and CTL1_era_w, are chosen due to their better representations of turbulent mixing compared to other nudging experiments.

Table 3-2. Experiments for simulating the day-to-night transition of ozone and NOx

Experiments	Meteorological driving field	Nudging	Urban heat	Vertical injection of emissions
CTL1	FNL	no	no	no
CTL1_vert	FNL	no	no	yes
CTL1_heat	FNL	no	yes	no
CTL1_fnl_w	FNL	yes	no	no
CTL1_era_w	ERA5	yes	no	no

Representation of urban heat effect

Urban heat, also called anthropogenic heat, that is emitted by human energy consumption is one of two external inputs in the energy balance of the earth surface, and the other one is solar radiation. It affects the atmospheric stability of the layer right above the ground by changing the direction of sensible heat flux. The upward sensible heat flux, which means warmer ground than the atmosphere, delivers energy into the atmosphere aloft and raises the near-surface air temperature, making the surface layer thermally unstable and possibly inducing more turbulence and creating a shallow convection layer.

Quantifying realistic anthropogenic heat in the urban area is an elaborate work [88]. For only serving the purpose of sensitivity test, the urban heat in this study is represented by an artificial elevation of the land surface temperature in the urban area. An increase of three Kelvin of the land skin temperature is implemented in the Noah land surface model subroutine. In the resulting simulation, a three Kelvin increase of the land skin temperature is sufficient to perturb the atmospheric stability and increase turbulent mixing of air masses.

Simulated NOx and ozone during the day-to-night transition

The experiment CTL1_heat simulates the lowest bias of NO_2 and ozone during the day-to-night transition, while other experiments much overestimate NO_2 (Figure 3-10a). The biases of the simulated NO_2 concentrations at 17:00 (the middle of the day-to-night transition period) in experiments CTL1, CTL1_vert, CTL1_heat, CTL1_fnl_w and CTL1_era_w are +21.6 ppbv (+75%), +14.0 ppbv (+48%), +1.6 ppbv (+6%) and +18.7 ppbv (+65%) and +19.9 ppbv (+69%), respectively. The concentration of simulated NO_2 at 17:00 in CTL1_heat is reduced by 40% compared to CTL1 and shows the best agreement with the observation. The simulated ozone concentrations are also improved in CTL1_heat with an average of 19.4 ppbv and a bias of +0.1 ppbv (+0.7%) at 17:00, while other experiments simulate very low levels of ozone, e.g. only 6.1 ppbv at 17:00 in CTL1 with a bias of -13.2 ppbv (-68%). The highly-elevated and biased NOx levels during the day-to-night transition in experiments, CTL1, CTL1_vert, CTL1_fnl_w and CTL1_era_w, is hereafter called 'transition high' (TH) problem and the associated experiments are called TH simulations.

With the same anthropogenic emissions, differences of simulated NOx and ozone concentrations in CTL1, CTL1_fnl_w and CTL1_era_w reflect the effects of different meteorological representations. The simulated NO in these three experiments diverges before 16:00 and then converges while peaking at 17:00 in the range of 42.9 ppbv (CTL1_era_w) to 48.1 ppbv (CTL). Very close values of NO_2, NO and ozone at 17:00 in the three experiments indicate that TH problem is less sensitive to meteorological representations.

By changing emissions in the surface layer (CTL1_vert), the simulated NO_2 and NO values in the surface layer are reduced by 15% and 51%, respectively, compared to CTL1. However, the TH problem of NO_2 is still displayed in CTL1_vert, but with less intensity. The TH problem of simulated NO is significantly alleviated. The weak response

of the simulated NO_2 concentrations at 17:00 to reduced surface emissions is because NO_2 is also supplemented by secondary production from the chemical reaction between NO and increased ozone (1-23), in addition to being emitted from the ground.

The simulated NO in CTL1_heat does not peak at 17:00 as in other experiments, but falls to its lowest value (8.2 ppbv) at 16:00 and slowly increases until next day morning (Figure 3-10b). Vertically, the simulated NO_2 and ozone at 17:00 have a smaller vertical gradient in CTL1_heat than in any other experiments (Figure 3-11). In the experiment CTL1_vert, vertical profiles of simulated NOx and ozone in injection layers (below 500 m) show a mixing-increase-like change, i.e. reduced vertical gradients. The reduction of NO_2 concentrations simulated in CTL1_fnl_w and CTL1_era_w is much smaller below 100m than that above 100m. Particularly between 100 m and 900 m, the simulated NO_2 concentrations in CTL1_fnl_w and CTL1_era_w are reduced by 27% compared to the control experiment CTL1 (Figure 3-11a). The influence of meteorological forcing is presumably not passed downwards into the surface layer (below 100m) during the day-to-night transition.

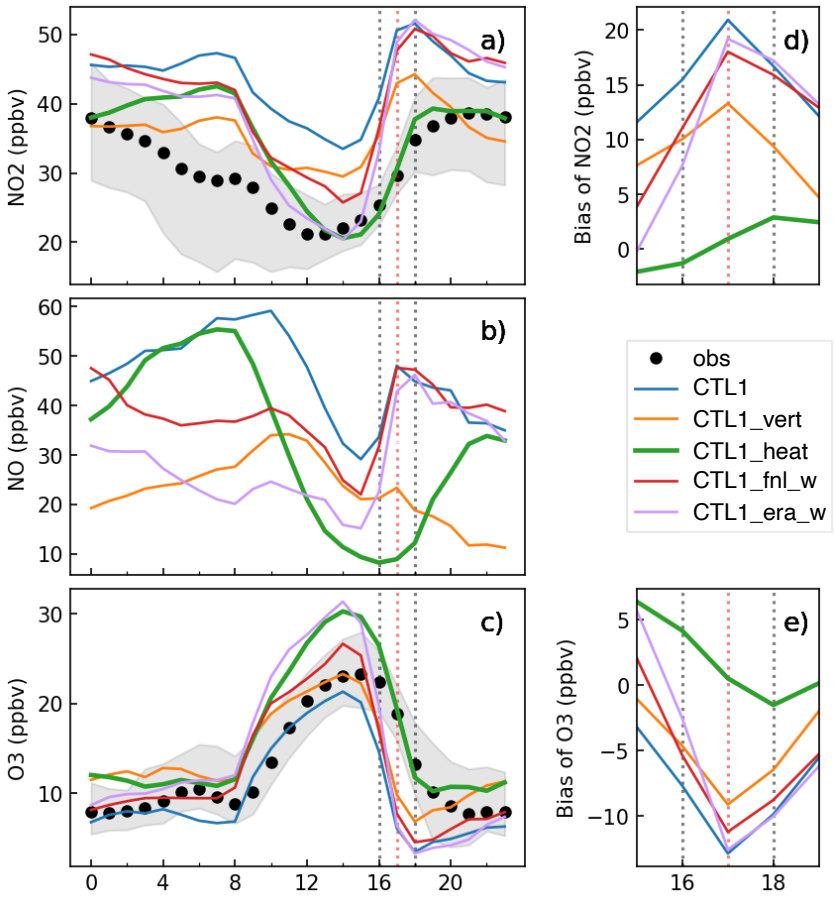

Figure 3-10. Mean diurnal variations of simulated and observed NO_2 (a), ozone (c) concentrations, and simulated NO (b) concentrations in five experiments and biases of simulated NO_2 (d) and ozone (e) between 15:00 LCT and 19:00 LCT. Grey shades represent the value ranges of observation sites. Three vertical dotted lines mark transition hours, from left to right, 16:00 LCT, 17:00 LCT and 18:00 LCT.

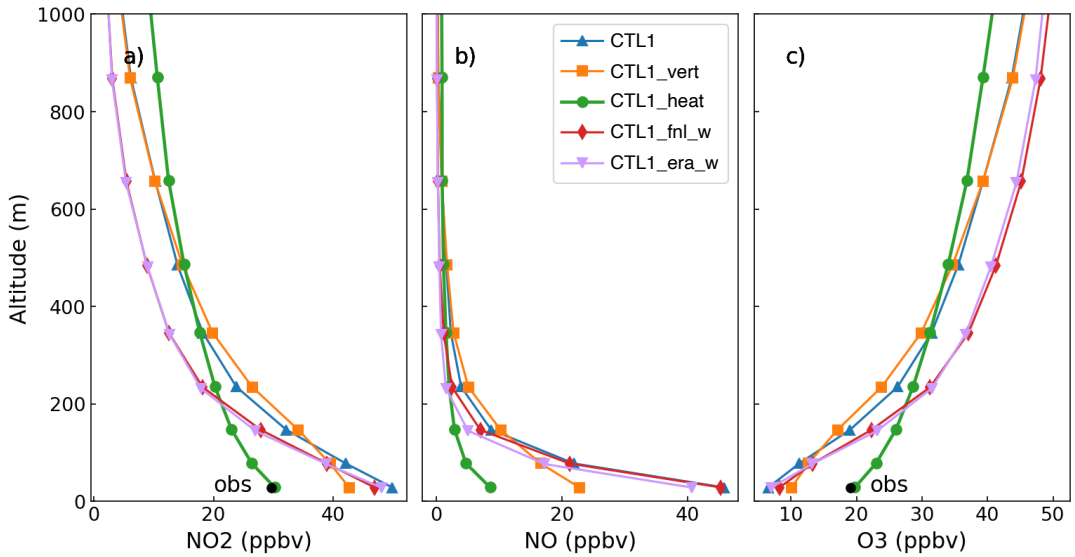

Figure 3-11. Vertical profiles of simulated NO_2 (a), NO (b) and ozone (c) at 17:00 LCT in five experiments. Surface observations of NO_2 and ozone are marked with black dots.

3.3.2 Diagnosis of the role of urban heat during the day-to-night transition

Budgets analysis

During the occurrence of TH, the sudden reduction in the contribution of turbulent mixing to the NO_2 and ozone budgets leads to the strong accumulation of NOx and rapid depletion of ozone. The large drops of the contribution of turbulent mixing to the NOx and ozone budgets at 17:00 are found in all TH simulations (Figure 3-12). In the experiment CTL1, the contribution of turbulent mixing to the budgets of NO_2, NO, and ozone fall sharply by 30%, 12%, and 34% from 16:00 to 17:00, respectively. Despite different meteorological representations, the experiments CTL1, CTL1_fnl_w and CTL1_era_w simulate a similar variation of the NOx and ozone budgets during the day-to-night transition.

The evolution of NOx and ozone budgets in TH simulations (the first, second, fourth and fifth rows in Figure 3-12) during the day-to-night transition is interpreted as follows. At 16:00, the contribution of turbulent mixing to the NOx and ozone budgets begin to decrease, while the eddy diffusivity K decreases significantly (Figure 3-14h). The resulting accumulation of NO at 16:00 leads to an increase of chemical reaction rate between NO and ozone (increased length of green bars in Figure 3-12). As turbulent mixing and the K value continue to decrease, the TH problem finally occurs at 17:00. At 18:00, the chemical contribution to the NOx and ozone budgets reach their lowest points, indicating a considerably reduced ozone level in the surface layer shown in Figure 3-10. After 18:00, the transport process is intensified to reduce the NOx level and increase the ozone level in the urban area of Beijing, when the contributions of transport to the NOx and ozone budgets increase (increased length of blue bars in Figure 3-12).

In contrast, the contribution of turbulent mixing to the NO_2 and ozone budgets in CTL1_heat increase from 13:00 to 17:00 and peak at 17:00 (the third row in Figure 3-12).

And the eddy diffusivity K during the day-to-night transition in CTL1_heat is larger than other experiments (Figure 3-14h). The decline in the contribution of turbulent mixing to the NO_2 and ozone budgets in CTL1_heat occurs at 19:00, instead of at 16:00 in TH simulations, while the transport takes over to reduce the NOx level and increase ozone levels. Therefore, the large accumulation of NOx and depletion of ozone are prevented and TH problem does not occur in the experiment with urban heat effect (CTL1_heat).

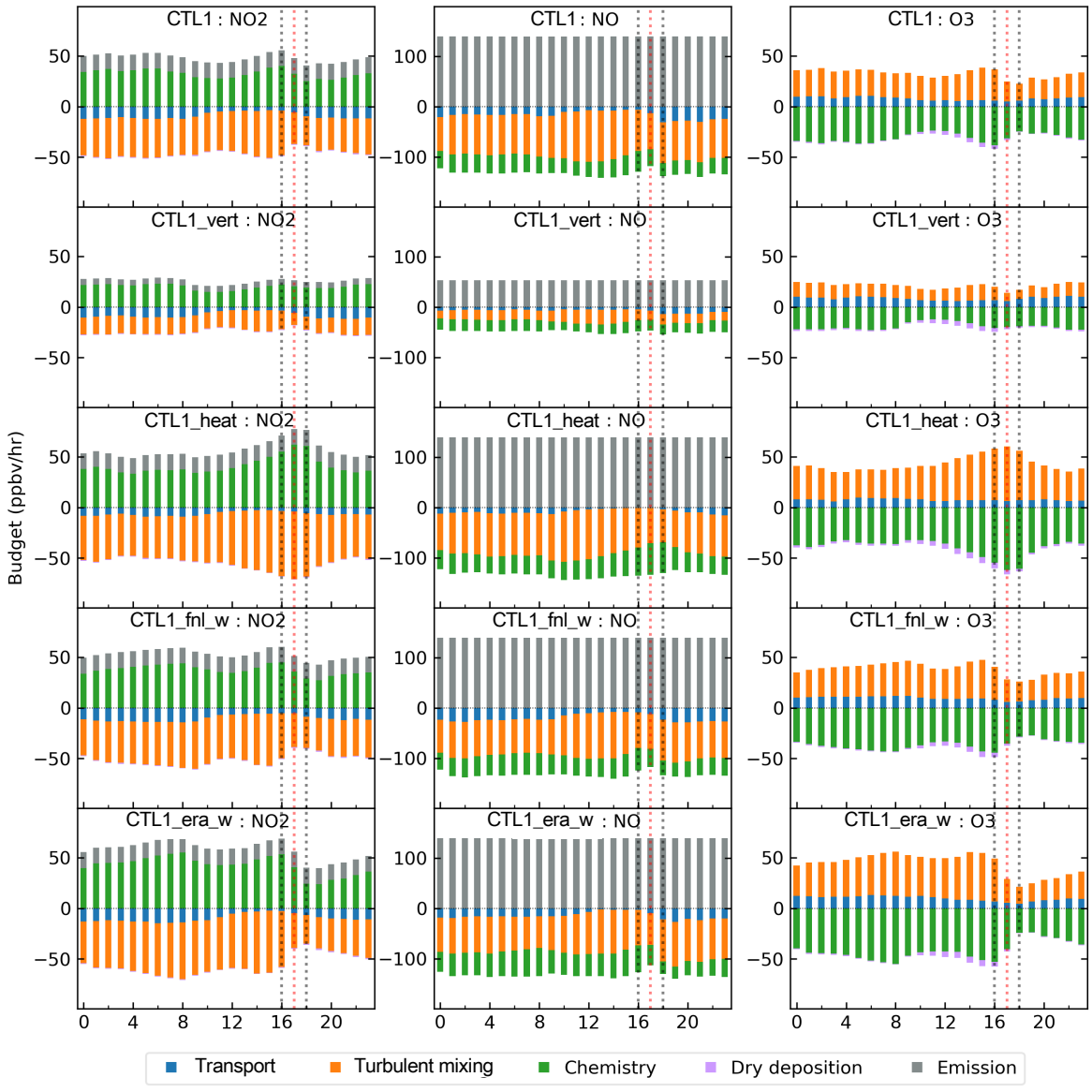

Figure 3-12. The mean diurnal variation of budgets of NO_2 (left panel), NO (middle panel) and ozone (right panel) of five experiments. Vertical lines mark time hours 16:00 LCT, 17:00 LCT and 18:00 LCT.

Vertically, from the ground up to a height of 500m, larger contributions of turbulent mixing to the NO_2 and ozone budgets are simulated in CTL1_heat (the middle column of Figure 3-13) compared to other experiments. The sign of the contribution of turbulent mixing to the NO_2 budget in CTL1_heat changes from negative (-) to positive (+) in the

third layer (146 m), while in CTL1 the sign changes in the second layer (77 m). However, the contribution of turbulent mixing to the NO budget of first three layers in CTL1_heat decrease slightly, because higher downward turbulent flux of ozone results in more chemical loss of NO and therefore the vertical gradient of NO decreases. In CTL1_vert, the quantities of the contribution of turbulent mixing to the NOx and ozone budgets are reduced (the second column of Figure 3-13), because vertical injection of emissions actually decreases the vertical gradients of NOx and ozone. The experiments CTL1, CTL1_fnl_w, CTL1_era_w simulate comparable budgets of NOx and ozone during the day-to-night transition despite differing simulations of meteorology (the first, fourth and fifth columns of Figure 3-13).

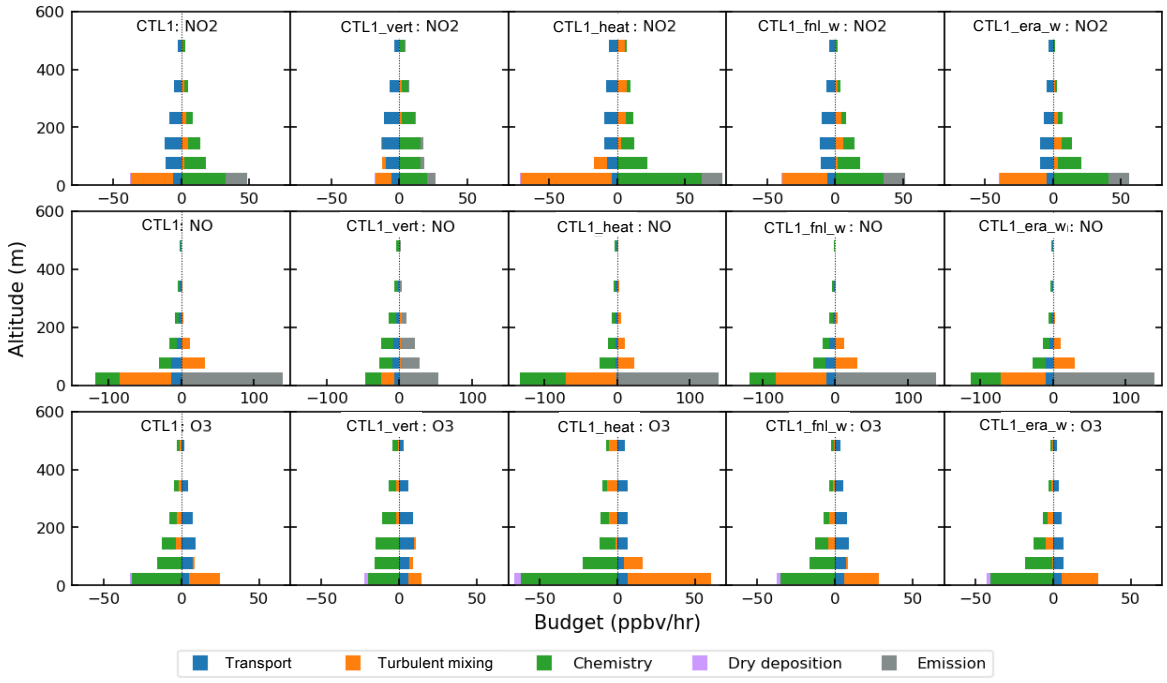

Figure 3-13. The vertical distribution of budgets of NO_2 (first row), NO (second row) and ozone (third row) of five experiments at 17:00 LCT.

Large drop of the eddy diffusivity K

The contribution of turbulent mixing to the NOx and ozone budgets significantly decrease during the day-to-night transition in TH simulations, and the large drop of eddy diffusivity K plays the key role (Figure 3-14h). In TH simulations CTL1, CTL1_fnl_w, CTL1_era_w (simulation of meteorology in CTL1_vert is same as CTL1 and not discussed in this subsection), the K value rapidly drops by 50%~55% from 15:00 to 16:00 and by 77%~94% from 16:00 to 17:00, reaching the lowest values 0.5~1.6 m^2/s at 17:00.

The hour 17:00 is the transition (sunset) hour that is right before the shortwave radiation reaching the ground turns to zero (Figure 3-14a). The upward sensible heat flux Q_H first becomes negative (-) (Figure 3-14b) at 17:00 in TH simulations, and the air temperature T_a is greater than the ground skin temperature T_s (Figure 3-14c). Therefore, the static stability increases when the sensible heat flux becomes downward. In addition, during the formation stage of the nocturnal stratified stable boundary layer, horizontal wind

speed (Figure 3-14e) is relatively low, which indicates a weak mechanical mixing (i.e. high dynamical stability). The increases of both static and dynamical stability lead to the reduction of friction velocity (u^*), which is calculated in the surface layer scheme as

$$u^* = \frac{kU}{ln\ ln\ \frac{z_1}{z_0} - \psi_m\left(\frac{z}{L}\right)} \tag{3-1}$$

where $k = 0.4$ is the von Kármán constant, U is the wind speed in the first model layer, z_1 is the middle height of the first model layer, z_0 is the roughness length. $\psi_m\left(\frac{z}{L}\right)$ is the integrated similarity functions for momentum, which is negative when the surface-layer air is warmer than the ground surface and positive when the surface-layer air is colder than the ground surface. During the day-to-night transition when the air temperature is higher than the ground temperature (Figure 3-14c), $\psi_m\left(\frac{z}{L}\right)$ changes from positive to negative and the wind speed U is relatively small. This results in that the friction velocity u^* simulated in TH simulations decrease to the lowest values 0.16~0.18 m/s at 17:00 (Figure 3-14f). The quantities of K of the surface layer, parameterized in YSU PBL scheme, is mainly determined by the friction velocity u^* under the 'stable' condition [89]. Therefore, the value K also reaches the lowest value at 17:00.

The various vertical structures of wind speed U and potential temperature θ in TH simulations are shown in Figure 3-15a and b, respectively. Large drops of eddy diffusivity K and friction velocity u^* at 17:00 still happen in all TH simulations, because the key factor, the sensible heat flux Q_H, in these simulations immediately becomes negative when the solar radiation is gone (Figure 3-14a and b).

The relationship between urban heat and turbulent mixing

Urban heat from the ground changes the surface-layer atmospheric stability during the day-to-night transition period and generates stronger turbulent mixing, which reduces the concentration of surface NOx and therefore increases the concentration of surface ozone. In the experiment with urban heat effect, CTL1_heat, the ground temperature (T_s) is 1.5 ℃ warmer at 17:00 and averagely 0.6 ℃ warmer through the whole night (19:00-07:00) than the surface air temperature (T_a) (Figure 3-14c). In the layer under 100m, the vertical gradients of potential temperature θ change from positive (thermal suppression) in TH simulations to slightly super-adiabatic (thermal enhancement) in CTL1_heat (Figure 3-15b), which means a 100m convective layer exists during the day-to-night transition. The convection velocity scale (W_{*s}) in the surface layer [7] can be calculated as

$$W_{*s} = \left[z_1 \frac{g}{\underline{\theta_v}} \underline{(w'\theta_v')_s}\right]^{1/3} \tag{3-2}$$

where $g = 9.8\ m/s^2$ is the gravitational acceleration, θ_v is the mean virtual potential temperature in the first model layer, $(w'\theta_v')_s$ is the surface virtual kinematic heat flux. In CTL1_heat, the surface layer is still convective at 17:00 and keeps a small convective velocity 0.2 m/s the whole night (green line in Figure 3-14d).

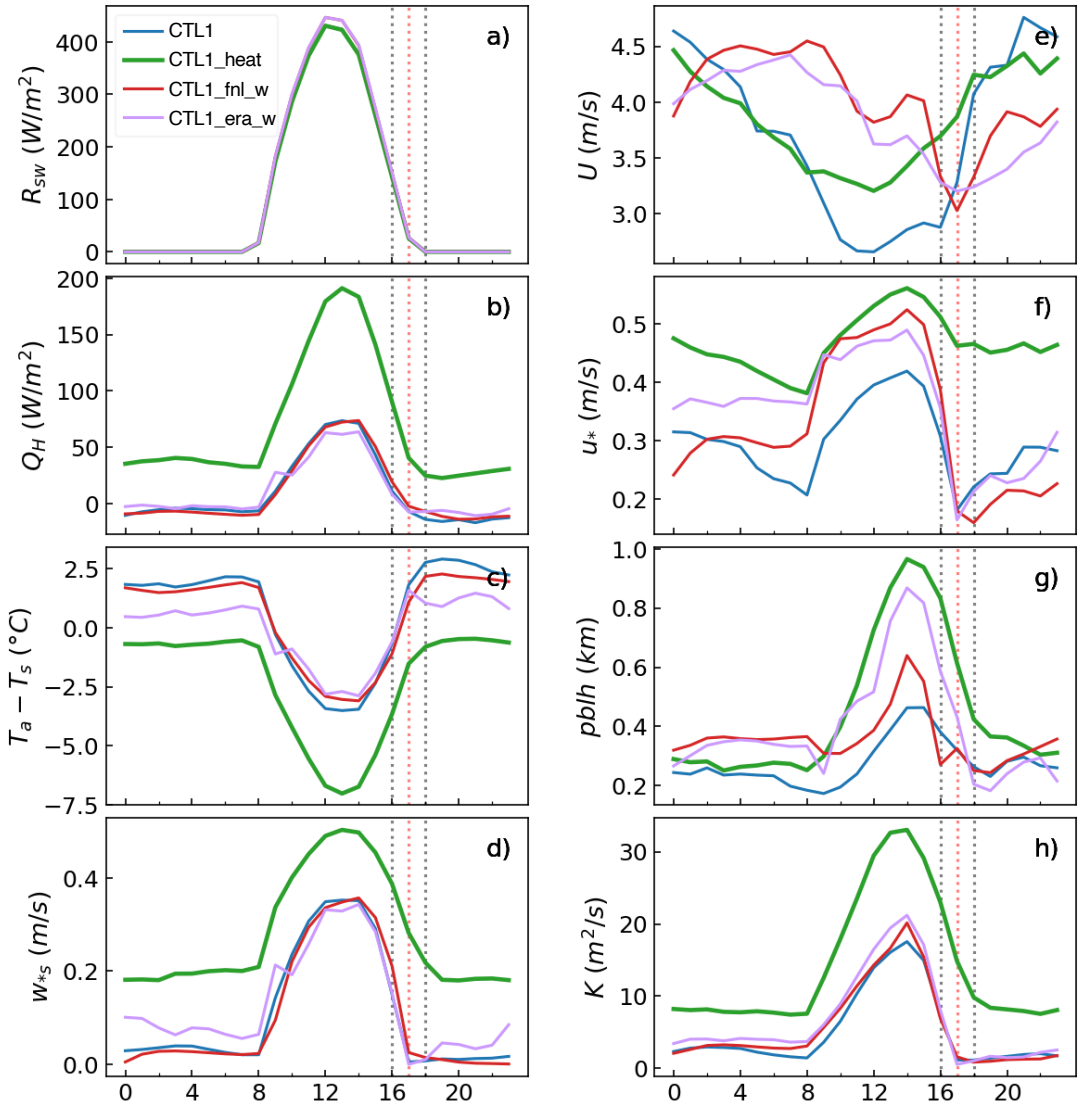

Figure 3-14. Mean diurnal variations of shortwave radiation R_{SW}, upward sensible heat flux Q_H, difference between surface layer air temperature T_a and ground skin temperature T_s, surface layer convective velocity W_{*S}, horizontal wind speed U, friction velocity u^*, boundary layer height $pblh$ and eddy diffusivity K simulated in TH simulations. Three vertical dotted lines mark time clocks 16:00 LCT, 17:00 LCT and 18:00 LCT. Horizontal dotted lines represent zero-value.

In CTL1_heat, the turning point of the curvature of diurnal variations of K and W_{*S} when transitioning from day to night is postponed for one hour. W_{*S} simulated in CTL1_heat decreases almost linearly between 16:00 and 18:00 and reaches the lowest value (~0.2 m/s) at 19:00, while in TH simulations W_{*S} decrease rapidly and reaches almost zeros at 17:00. Correspondingly, the eddy diffusivity K simulated in CTL1_heat experiences a smooth decrease during the day-to-night transition period and keeps a mean value of 7.9 m^2/s through the whole night.

An increase of downward momentum flux during the day-to-night transition is also seen in CTL1_heat, while in TH simulations the surface momentum stays low no matter how large wind speed is above (Figure 3-15a). The vertical profile of horizontal mean wind speed simulated at 17:00 in CTL1_heat decreases above 100m and increases underneath. An increase of downward momentum flux indicates an increase of eddy diffusion intensity. The eddy diffusivity K simulated at 17:00 by CTL1_heat significantly increases (Figure 3-15c) by a factor of 14 in the surface layer and a factor of 47 at the height of 233m. As a result, the upward turbulent fluxes of simulated NOx in CTL1_heat increase by a factor of 3.6 in the surface layer, while the downward turbulent flux of ozone increase by a factor of 15.1 (Figure 3-15d, e and f).

In summary, the occurrence of TH problem is because the turbulent mixing of NOx and ozone is rapidly suppressed once the solar radiation is gone during the day-to-night transition. The lowest values of eddy diffusivity and friction velocity are reached in the occurrence of TH problem, in which the 'stable' condition of the boundary layer coincides with the weak mechanical mixing in the low wind speed period in the early evening. Urban heat from the ground maintains a shallow convective layer during the day-to-night transition and prevents the occurrence of TH, resulting in smoothed day-to-night transitions of eddy diffusivity and NOx and ozone concentrations.

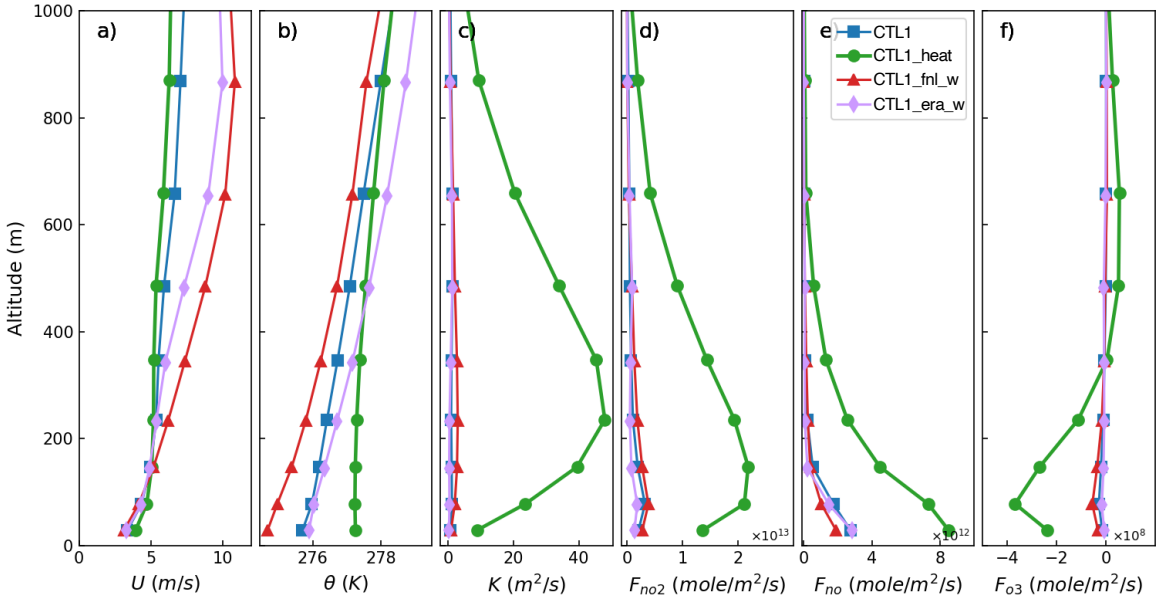

Figure 3-15. Vertical profiles of horizontal wind speed U (m/s), potential temperature θ (K), eddy diffusivity K (m^2/s) and turbulent mixing fluxes of NO_2 F_{no2} (mole/m^2/s), NO F_{no} (mole/m^2/s) and ozone F_{o3} (mole/m^2/s) at 17:00 LCT simulated TH simulations.

3.4 Conclusions

This chapter investigates the different roles of large-scale wind, as the mechanical forcing of turbulent mixing, and urban heat, as the thermal forcing of turbulent mixing, in influencing the surface ozone in the urban area of Beijing during winter time.

The winter boundary layer in Beijing is susceptive to the strong northerly wind invasion to the region. The strong northerly wind invasion is associated with surface ozone enhancement at night, which normally happens at night and can lead to ozone concentration increase by a factor of up to 1.9 (+19 ppbv) and NO_2 concentrations drop by up to 84% (-44 ppbv). The enhanced ozone level at night can be even higher than daytime maximum. The NOE (nocturnal ozone enhancement) in the urban area of Beijing is contributed by both increased advective transport and mechanical turbulent mixing. The increased mechanical turbulent mixing in PBL is the major and indispensable process that accounts for the NOE in the urban area of Beijing.

The second part of this chapter discusses the role of urban heat in controlling variations of NOx and ozone during the day-to-night transition. Simulations of surface NOx and ozone concentrations often show much sharper curves during the day-to-night transition than observations. It is mainly due to very weak eddy diffusion (turbulent mixing) of chemicals simulated in the model. By adding urban heat effect, represented by the increased ground temperature in the model, the sharp curves in variations of NOx and ozone concentrations during the day-to-night transition are smoothed and, therefore, the biases of concentrations of simulated NOx and ozone in this period are reduced from +75% to +6% and from -68% to +0.7%, respectively. At the same time, a shallow (~100m) convection layer above the ground is formed during the day-to-night transition and the later night, which increases the boundary layer diffusion capacity.

Either large-scale wind or urban heat contributes to the increase of the surface ozone level in the urban area of Beijing during wintertime. They compete against the ozone consumption by intense NOx emissions in the polluted winter boundary layer. Next chapter will focus on the responses of the surface ozone to different formulations of anthropogenic emissions.

4 Responses to anthropogenic emissions

4.1 Introduction

Emissions of pollutants, mostly from anthropogenic sources, release harmful chemical substances into the air and constantly provide 'fuel' for atmospheric chemistry. These pollutants are often emitted on the surface or at a certain height, varying according to the type of sources. For example, tall power plant chimneys emit pollutants at height of hundreds of meters. Heat contained in the flue gas from these chimneys generates buoyancy which pushes the emitted plume to higher altitudes, even above the ABL [90]. To parameterize this process, plume rise model is often used to generate the effective emission heights of individual chimneys [91, 92]. The study by Guevara et al. on the effects of the vertical distribution of emissions on tropospheric chemistry using a global model [92] indicates that the concentrations of surface trace gases in polluted region has much larger sensitivity to vertical distribution of emissions than the concentrations in rural regions and in the free troposphere. Section 4.2 investigates the responses of ozone to vertical injection of emissions during wintertime in the region of Beijing using model simulations.

Emission inventories developed from annually domestic statistic data, e.g. energy consumption, vehicle annual mileage and agricultural activities, provide mostly only yearly total emissions. But the emission of pollutants is a dynamical process not only with annual, but also with seasonal, monthly, weekly and diurnal variations (e.g. diurnal variation of emissions from traffic and residential activities). In densely populated urban areas, emissions are characterized by diurnal and weekly variation. Due to the lack of nation-wide statistical data on shorter time scales, temporal profiles of emission [93, 94] are derived based on field measurements, e.g. traffic flows [95]. In a study of modelled ozone in Europe performed for the summer of 2007, Menut et al. [96] found that the calculation of the night-time ozone concentration is improved by adopting diurnal evolution of emissions while daytime ozone is rather insensitive to this diurnal process. Section 4.3 discusses whether the modelled winter ozone concentration in the urban area of Beijing is significantly modified when the adopted emissions of primary pollutants vary diurnally and weekly.

Obtaining suitable emission inputs for a high-resolution chemical transport model is not easy, because most existing emission inventories have only a spatial resolution of at least 10 kilometers. However, the inhomogeneity of urban environments indicates high spatial variability in emissions in urban areas. High-resolution emissions are therefore important for models to properly treat the nonlinear effects of atmospheric chemistry and reproduce accurate concentrations of atmospheric pollutants. To increase the resolution of emissions in urban areas requires that emissions can be downscaled according to the location of the sources, for example traffic emissions along the main roads and the emissions from the identified chimneys of factories and power plants.

Section 4.4 addresses this issue by downscaling a global gridded emission inventory from 10 kilometers to one kilometer using "proxies" based on information such as land use, locations of industrial facilities and population distribution. The effect of downscaled emissions is also analyzed with a set of simulations.

A special case is discussed in Section 4.5, which is the response of ozone behavior to vast emission reductions during COVID-19 pandemic in China in the first two months of the year 2020. The polluted regions in eastern China experienced the largest reduction of emissions in February 2020, with 20%-30% reductions in emissions of NOx, SO_2 and VOCs [97]. The column NO_2 observed by the satellite TROPOMI in Eastern China, as a result, was reduced by 71.9% from 23 January to 13 February 2020 [98] and by 39.7% in February 2020 [99], comparing with the same period in the year of 2019. The reduction of NO_2 concentrations/emissions mainly occurred over the North China Plain (NCP), which is the most polluted region in China. The observed surface ozone concentration during lockdown, however, increases, for example by a factor of 2 in Northern China, compared with that before lockdown [39]. A slight reduction in observed ozone concentration is observed in the southern part of China during the pandemic [100]. The different changes in surface ozone concentrations were associated with the different chemical regimes in different part of China and has been investigated in several studies [100, 101]. In Section 4.5, the different responses of ozone in Northern and Southern China to NOx emission reduction during COVID-19 pandemic are reproduced with the regional chemical transport model WRF-Chem.

4.2 Vertical injection of emissions

4.2.1 Emission formulation

Warm plumes containing pollutants can rise up to high altitudes due to thermal buoyancy, which is not resolved in the model. Vertical injection of anthropogenic emissions is formulated to account for emissions from tall factory chimneys and human-caused ground fires. In this study, injection heights are differentiated by different sectors of emission sources, as shown in Figure 4-1a. The highest injection level (200 m to 500 m) is associated with power plants with the injection height above most power plant chimneys to account for upward diffusion of warm flue gas from chimneys due to thermal buoyancy [91, 92, 102]. The injection heights used in this study are based on the study in Europe [91] and might not well represent the injection heights in the region of Beijing. But the representation would be adequate to sever the purpose of sensitivity tests The injection heights actually change with different model vertical resolutions. Figure 4-1b shows the vertical distributions of NO emissions fluxes injected into the bottom 6 model layers in a low-resolution model with 37 vertical layers and into the bottom 12 model layers in a high-resolution model with 47 vertical layers, respectively. In the high-resolution model, 37% of total NO emission flux is allocated in the first model and 53% in layers between 77 m and 233 m.

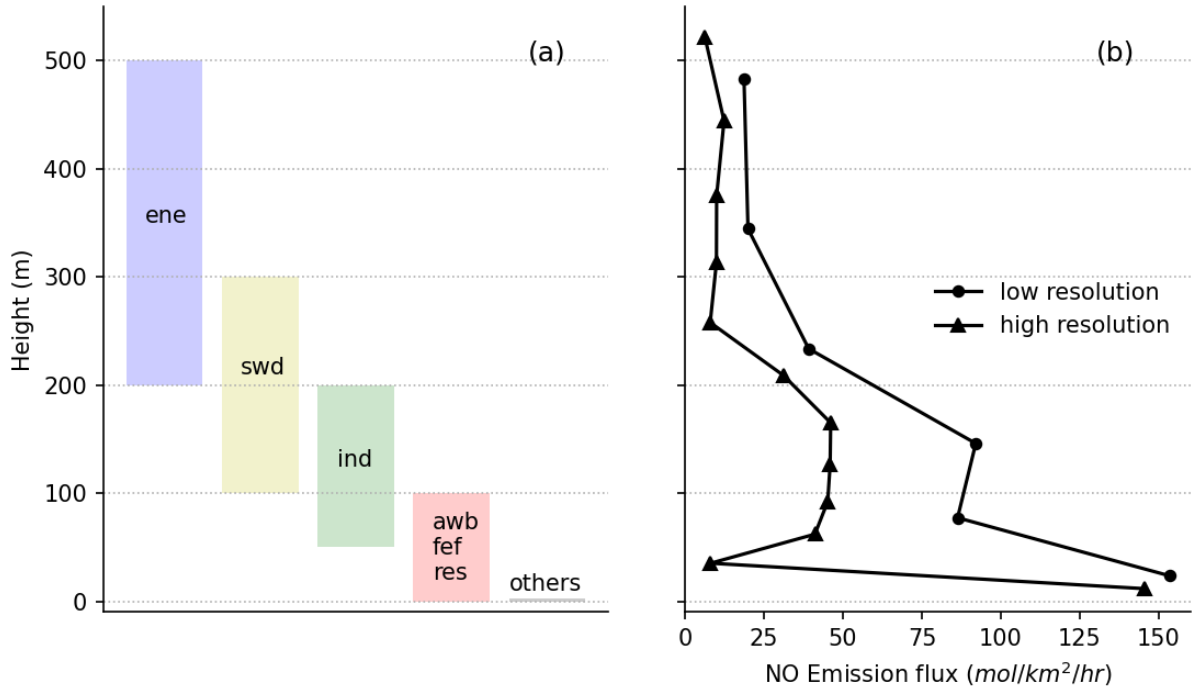

Figure 4-1. Injection heights of different emission sources (a) and vertical distributions of NO emission fluxes in model vertical settings of 37 layers (black line with dots) and 47 layers (black line with triangles) (b). (ene – power plant; swd – solid waste and waste water; ind – industry; awb – agriculture waste burning; fef – fugitive; res - residential).

4.2.2 Simulation

Experiments

The vertical injection of emissions is tested in simulations with two different vertical resolutions. In the control case CTL1, there are in total 37 vertical layers with emissions injected only in the first model layer, while in the test case CTL1_vert, anthropogenic emissions are vertically distributed up to the sixth layer. In another control case CTL2, there are 47 vertical layers, while in the test case CTL2_vert, anthropogenic emissions are injected into 12 layers. The detail on experiments is shown in Table 4-1.

Table 4-1. Experiments for testing vertical injection of emissions

Experiments	Vertical layers	Emission injection layer	Diurnal/weekly variation	Downscaled emission
CTL1	37	surface	no	no
CTL1_vert	37	up to 500m	no	no
CTL2	47	surface	no	no
CTL2_vert	47	up to 500m	no	no

Results

With the first model layer in CTL2 is shallower than that in CTL1, the concentrations of surface NO_2 and NO increase by 5% (2.2 ppbv) and 21% (9.5 ppbv), respectively. In other words, the concentrations of emitted pollutants are enhanced when the first model layer is shallower. Therefore, it is imperative to distributed emissions vertically when the vertical resolution of the model increases.

The model performance of ozone and NO_2 concentrations is improved in experiments with vertical injection of emissions (CTL1_vert and CTL2_vert) (Figure A-5). The biases of ozone are reduced from -21% to 9% in CTL1_vert and from 31% to -2% in CTL2_vert compared to the control cases. The biases of NO_2 in these four experiments are 41%, 16%, 48% and 23%, respectively. Validation of modelled NO concentrations is not possible as no observation data are available.

Surface NO decreases significantly in CTL1_vert and CTL2_vert comparing to the control cases. Too large decrease of NO at night (19:00-6:00) leads to even lower nighttime concentration of NO than daytime (9:00-16:00) (Figure 4-2). The decrease of surface NO_2 concentration after emission injection is also larger at night with a decrease of 6 ppbv and a 8 ppbv in day- and nighttime, respectively, in the CTL1_vert. Similar decrease is observed in the CRL2_vert case. The increase of ozone concentration is also larger at night due to NOx titration controlling ozone chemistry. It is easily inferred that the change of concentration of dispersed gas is larger in a smaller volume when changing the same amount of total mass. By analogy, nocturnal boundary layer at night is shallower than the daytime boundary layer, so with the same reduction of emissions in the first model layer, the consequent change of pollutant concentrations is larger at night than in daytime.

Vertically, the perturbations of emission vertical injection to simulated NO_2, NO and ozone are in layers under around 600 meters and are stronger at night (first column in Figure 4-3). For the experiment with low vertical resolution (CTL1), the concentration of simulated NO_2 in the test case with vertical injection of emissions (CTL1_vert) decreases from the surface up to the height of approximately 150 meters and then increases with the peak value 0.96 ppbv (8%) at the height of 377 meters in daytime and the peak value 3.2 ppbv (17%) at the height of 210 meters at night. On the other hand, the simulated ozone behaves oppositely. Besides the surface, above 150 meters, the maximum reduction of concentration of ozone is -0.8 ppbv (-2%) at the height of 377 m in daytime and -2.5 ppbv (-9%) at the height of 210 m at night. The NO concentration reduces only under 150 meters and does not change significantly above 150 meters, even though NO is constantly injected to those layers, indicating that injected NO above 150 meters is rapidly consumed by the abundant ozone.

Next, the budgets of the pollutants with different components of atmospheric processes are analyzed. In the four columns in the right of Figure 4-3, the budgets of NO_2, NO and ozone with five components, i.e. transport, turbulent mixing, chemistry, dry deposition and emissions, are shown on different model layers, respectively, averaged over daytime period and nighttime period. It is noticeable that the

contribution of turbulent mixing (yellow bars) to the budgets of NO_2, NO and ozone decreases in both daytime and nighttime after injecting emissions vertically. Direct injecting emissions to higher layers reduces the vertical gradients of NOx and ozone and therefore turbulent fluxes of these gases are reduced. In addition, the contribution of transport to the budgets of NO_2 and ozone at night increases above the third model layer, which indicates that the ozone 'cavity' in urban area is enhanced at higher altitude at night when extra ozone is titrated by the injected NO emissions. The results of cases with higher vertical resolution (CTL2 and CTL2_vert) are similar to Figure 4-3 and shown in Figure A-7.

In summary, nighttime ozone and NOx responds stronger to the vertical injection of emissions. The shallowness of the nocturnal stable boundary layer amplifies the responses of surface ozone and NOx concentrations to the reduced emission in the surface layer. In daytime, with the help of strong turbulent mixing, the effect of vertical injection of emissions is not significant. Vertical injection of emissions is particularly meaningful in the winter nighttime boundary layer, especially when the emission is strong or the pollutant concentrations are high.

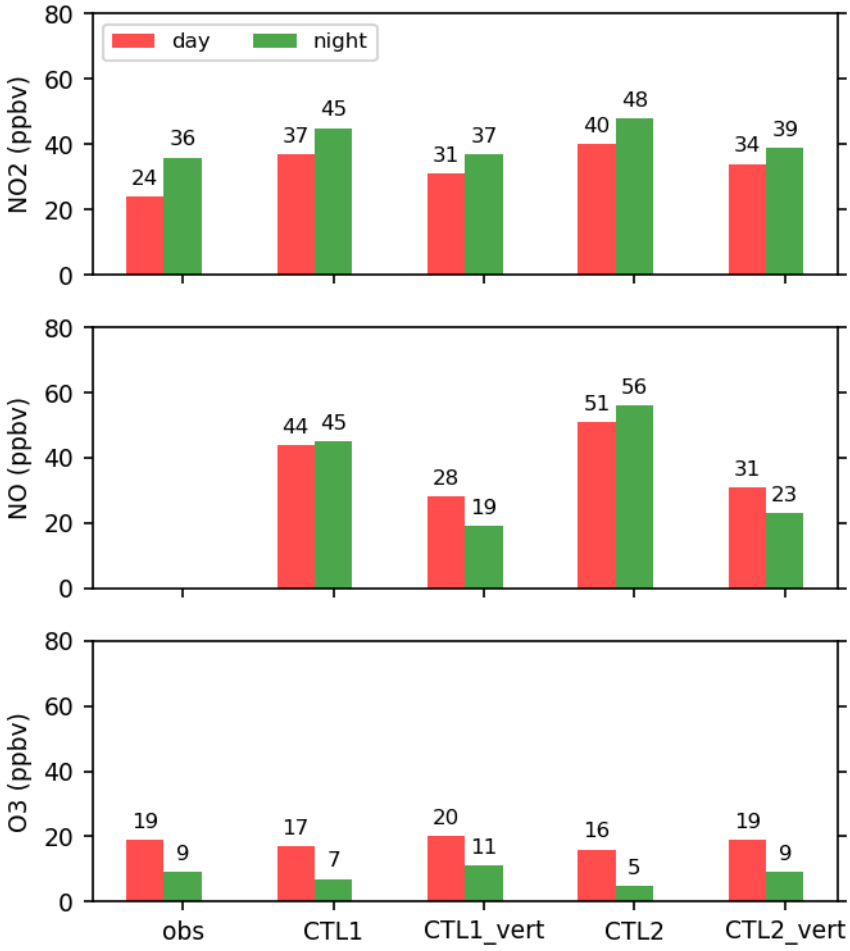

Figure 4-2. Mean mixing ratios of NO_2, NO and ozone in daytime (09:00-16:00) and nighttime (19:00-6:00) in observations and simulations CTL1, CTL1_vert, CTL2, CTL2_vert in the city of Beijing. The observation of NO is not available. Data is averaged over a time period of January 12 to 22, 2019.

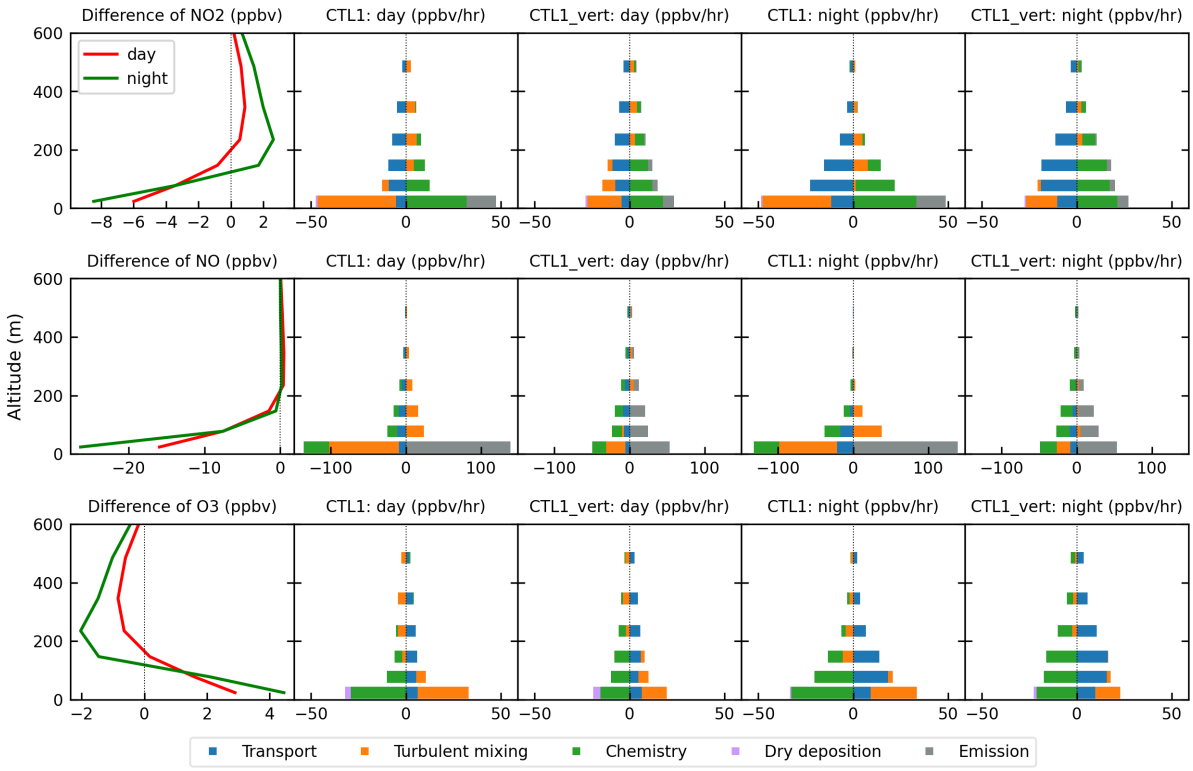

Figure 4-3. First column: difference of vertical profiles of NO_2, NO and ozone between the control case CTL1 and the case CTL1_vert during daytime (09:00-16:00) (red line) and nighttime (19:00-6:00) (green line). Second and third columns: vertical distributions of budget components of NO_2 (first row), NO (second row) and ozone (third row) in daytime for the case CTL1 and the case CTL1_vert, respectively. Fourth and fifth columns: idem but for nighttime. Data is averaged over a time period of January 12 to 22, 2019.

4.3 Diurnal/weekly variation of emissions

4.3.1 Emission formulation

To account for the diurnal/weekly variation of anthropogenic emissions, the sector-based temporal profiles of emissions from Crippa et al. [78] are applied to anthropogenic emissions in this study. In convention, the type of emission source is referred as 'sector'. The applied factors to account for these variations and the resulting diurnal variation of emission fluxes of NO are provided in Figure 4-4. The sector nomenclature in the dataset developed by Crippa et al. follows the Emissions Database for Global Atmospheric Research (EDGAR), which is different from the nomenclature of CAMS emission inventory. The connection between CAMS sectors and EDGAR sectors are shown in Table A-6.

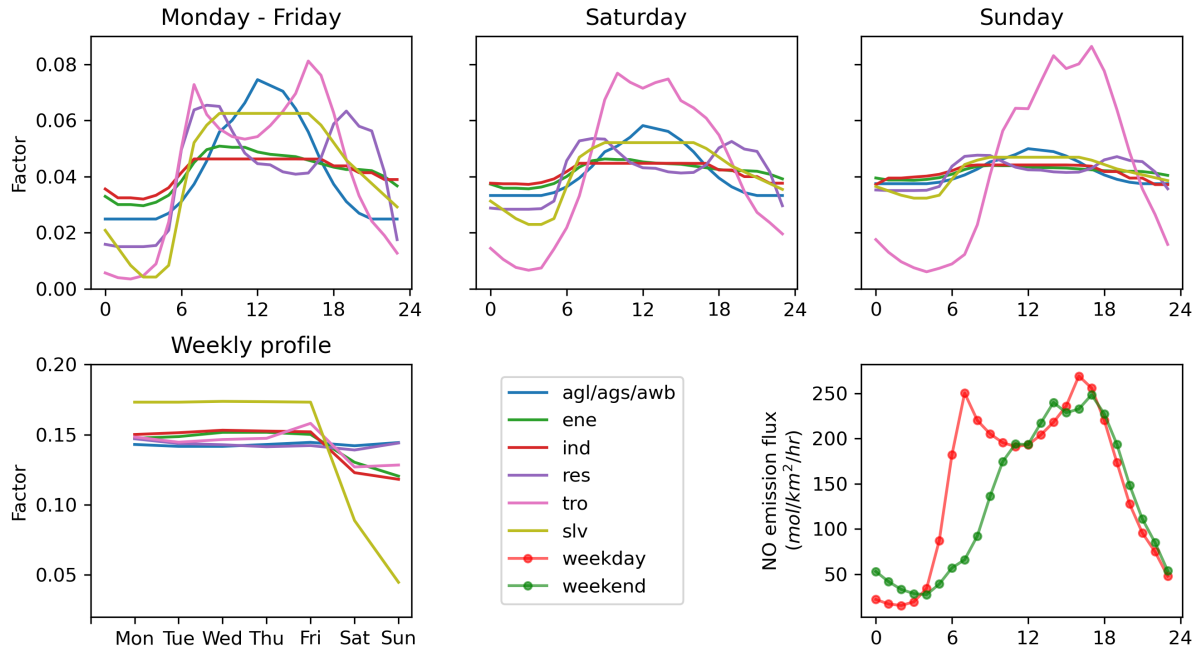

Figure 4-4. First row: sector-based factors applied to emissions in a day for weekdays (Monday to Friday), Saturday and Sunday. Second row left: sector-based factors applied to daily emission in a week. Second row right: diurnal variations of NO emission flux in weekday and weekend. Emission factors are from the dataset developed by Crippa et al. [78]. Four sectors are not shown here, because sectors tnr and fef have only diurnal but no weekly profile, the sector swd has neither of them and the sector shp for ship emissions is not relevant in the studied region.

4.3.2 Simulation

Experiments

Since vertical emission injection improves simulations of surface concentrations of ozone and NOx, the experiment case testing the responses to diurnal/weekly variation of emissions (CTL2_vert_t) is directly based the case CTL2_vert, which has 47 vertical layers and injects anthropogenic emissions vertically. The detailed description of experiments is shown in Table 4-2. It is expected that a combination of higher vertical resolution of the model, resolving vertical variability of emissions and applying diurnal/weekly profiles of emissions leads to a good performance in simulating surface concentrations of ozone and NOx in the urban areas of Beijing.

Table 4-2. Experiments for testing diurnal/weekly variation of emissions

Experiments	Vertical layers	Emission injection layer	Diurnal/weekly variation	Downscaled emission
CTL2_vert	47	up to 500m	no	no
CTL2_vert _t	47	up to 500m	yes	no

Results

Similar to the result of Section 4.2, night-time concentrations of NOx and ozone are more sensitive to diurnal variation of emissions. When the diurnal variation is considered, the nighttime (19:00-6:00) NOx emissions in the first model layer decrease by 49%. The nighttime concentration of surface NO_2 and NO drops considerably by 5.4 ppbv (-14%) and 8.3 ppbv (-35%), respectively. Correspondingly, the average concentration of surface ozone increases by 3.6 ppbv (38%) at night. In daytime (9:00-16:00), the NOx emissions are increased by 48%. The responses of simulated concentrations of surface NO_2 and ozone in daytime to the increased NOx emissions are, however, relatively small. The mean concentration of surface NO_2 increases by 2.8 ppbv (+7.7%), while the mean concentration of surface ozone decreases by 1.4 ppbv (-8%). The diurnal variations of concentrations of simulated NO_2, NO and ozone associated with NO_2 and ozone observations are shown in the upper row of Figure 4-5 and the time series of concentrations of these three species is shown in Figure A-6.

Night-time accumulations of NOx do not happen in the experiment with diurnal/weekly variation of emissions (CTL2_vert_t) with a reduction of 49% in night-time NOx emissions. It is indicated that the emitted NOx is sufficiently diffused in the nocturnal boundary layer; therefore, ozone tends to increase at night. In daytime, despite an increase of 48% in NOx emissions, the boundary layer still has the capacity to diffuse all emitted NOx. At 14:00, although the difference in NOx emissions between the two experiments is huge (159 $mol/(km^2 \cdot hr)$ in CTL2_vert and 246 $mol/(km^2 \cdot hr)$ in CTL2_vert_t), the simulated mean concentrations of NO_2 are comparable (32.2 ppbv in CTL2_vert and 35.2 ppbv in CTL2_vert_t) in two experiments (Table 4-2). The boundary layer diffusion capacity is determined by meteorology and stays the same in two experiments (CTL2_vert and CTL2_vert_t). The relative relationship between the diffusion capacity of the boundary layer and the intensity of emissions determines whether NOx is accumulated or dispersed and ozone changes inversely with NOx.

The strong turbulent diffusion in daytime boundary layer can dampen the large perturbation of emissions variations to surface concentrations of NOx and hence ozone. However, at night, the reduced diffusion capacity due to weak turbulent mixing readily leads to accumulation of NOx, which significantly increases the titration of surface ozone. Therefore, good representation of turbulent mixing in the nocturnal boundary layer and the NOx emission intensity are both important for an accurate simulation of night-time surface ozone concentration during wintertime.

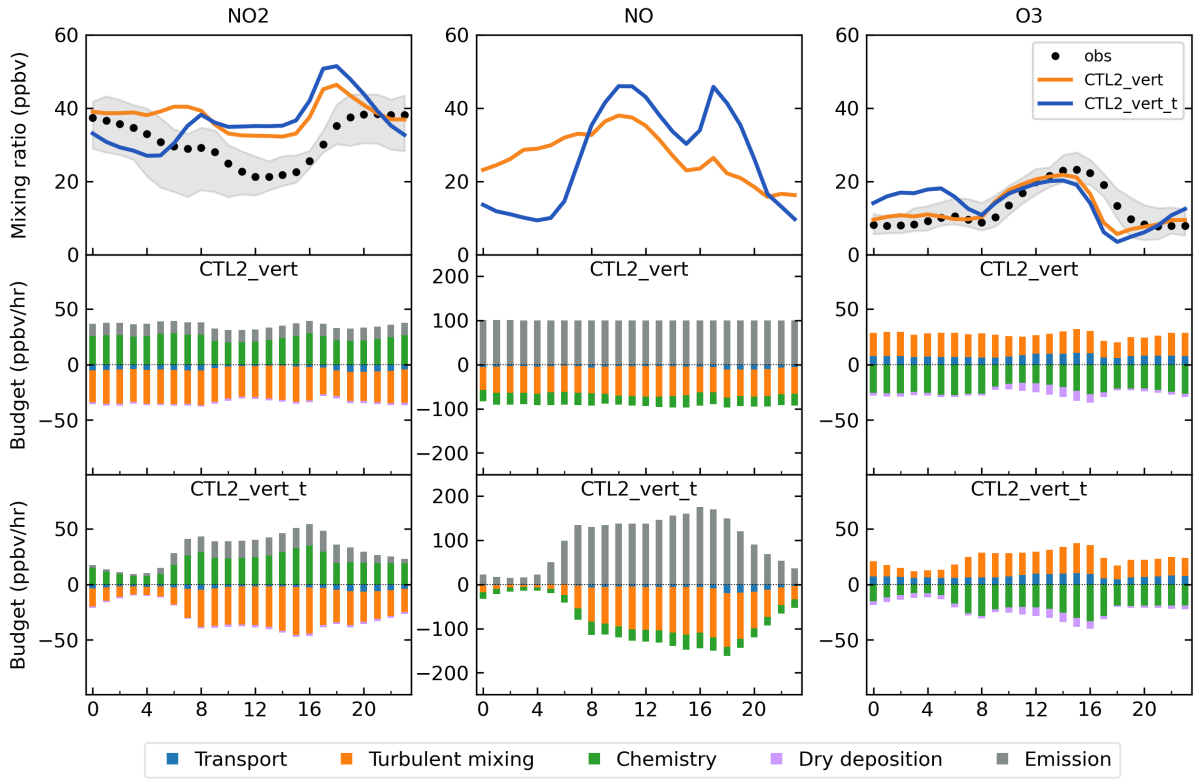

Figure 4-5. First row: Diurnal variation of simulated and observed NO_2 (left) and ozone (right) and simulated NO (middle) in the city of Beijing. Second and third rows: mean diurnal variations of budgets of NO_2, NO and ozone of experiments CTL2_vert, CTL2_vert_t. Data is averaged over a time period of January 12 to 22, 2019.

4.4 Downscaling of emissions

4.4.1 Methodology

With the total emissions conserved, anthropogenic emissions at the resolution of 10km are downscaled horizontally to the resolution of 1 km by the top-down approach in a region centered by the city of Beijing. The original emission inventory used is the global dataset of anthropogenic emissions CAMS-GLOB-ANT v4.2-R1.1 (hereafter CAMS), which has a spatial resolution of 10 km (see Section 2.2.2). The downscaling of the emissions inventory is based on weight factors derived from specific proxies, which are extracted from datasets containing information correlated to specific emission sources. Downscaling of emissions are performed on five emission sources, i.e. agriculture, traffic, residential, power plant and industry. The procedure of downscaling is illustrated in Figure 4-6.

First, several sectors in CAMS emission inventory are lumped together to represent one emission source. Sector lumping of other emission sources are shown in Table 4-3. For example, traffic emissions are a sum of emissions of sectors tro (road transportation) and tnr (off-road transportation). Emissions of four sectors including shp (ships), swd (solid and water waster), fef (fugitives) and slv (solvents) are not downscaled in this study because of their small fractions in the total emissions and lack of specific proxies in the studied region. Five emission sources to be downscaled are then classified into

area sources (spatially continuous emissions) including agriculture and residential, line source including traffic and point sources including power plant and industrial.

Then, the lumped emissions at the original resolution of 10km are resampled into emissions at the resolution of 1km. Based on the type of emission sources, two resampling methods are developed. For emissions from area sources and the line sources, which are spatially coherent, coarse 10-km grids are mapped into fine 1-km grids by spatial bi-linear interpolation. For emissions from point sources, mass conservation is maintained in the process of resampling. More explanations on resampling of point source emissions are discussed in the subsection *Resampling of point source emissions*. Next, a 1-km map of weight factors is derived by calculating one or multi proxies. The deductions of weight factors for five emissions sources are detailed in the subsection *Weight factor*. Then the 1-km map of resampled emissions are weighted by applying the map of weight factors. At the end, the weighted emissions are rescaled in order to conserve the total mass of emissions.

Resampling of point source emission

For point sources, i.e. power plant and industrial factories, the emission flux of one grid represents the sum of emission fluxes of all power plants or industrial factories in that grid. However, as mentioned in Section 2.2.2, the emissions in China in the CAMS emission inventory was compiled by merging the local emission inventory MEIC, which has a resolution of 25km. Thus, it is more appropriate to adopt the 25-km grid in MEIC for resampling. The calculation that is done by CAMS working group to regrid 25-km grids in MEIC into 10-km grids in CAMS is based on mass conservation. The emissions in 25-km grids are generated by reverse the process. Then, the emissions in 25-km grids are resampled into that in 1-km grids by conversing the mass.

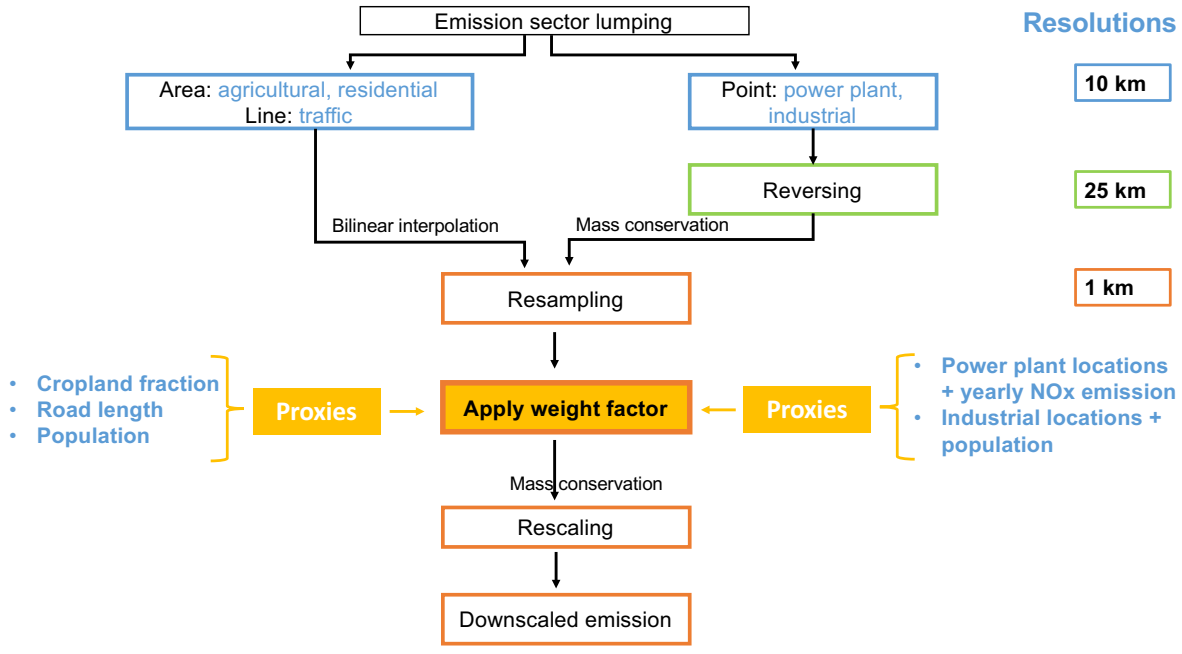

Figure 4-6. Work flow of emission downscaling

Table 4-3. Lumping of emissions sectors for downscaling and proxies used for every lumped sector. Not downscaled sectors are also listed in the end the table.

Type of source	Emission source	CAMS sector	Description	Proxies for downscaling	Data source
Area source	Agariculture	ags	Agriculture soils	Cropland fraction (100m)	Copernicus Global Land v3.0.1 [103]
		agl	Agriculture livestock		
		awb	Agriculture waste burning		
	Residential	res	Residential	Population density (1km)	LandScan 2019 [104]
Line source	Transportation	tnr	Non-road transportation	A sum of road length	Open Street Map [105]
		tro	Road transportation		
Point source	Energy	ene	Power generation	Annual emissions of individual power plants	China Emissions Accounts for Power Plants (CEAP) [106]
	Industrial	ind	Industrial processes	Population density in industrial area	LandScan 2019; Land cover dataset developed by RESDC [107]; Open Street Map
-	Others	shp	Ships	-	-
		swd	Solid and water waste	-	
		fef	Fugitive emissions from solid fuels	-	
		slv	Solvents	-	

Weight factors

Residential and agricultural emissions, as area emission sources, are downscaled with proxies, the population density in LandScan 2019 [104] with a resolution of 1km and the cropland fraction in Copernicus Global Land v3.0.1 [103] with a resolution of 100m, respectively. For residential emissions, the population density nearest to the 1-km downscaling grids is defined as weight factors of that grid. The proxy used for downscaling the agriculture emissions has a spatial resolution of 100m. Thus a sum of crop fractions of all 100-m grids contained by a 1-km downscaling grid is taken as weight factors. On the edges of a 1-km downscaling grid, some 100-m grids are divided and the values of these grids are counted by fractions of area falling in the 1-km downscaling grid.

Traffic emissions are considered as line emission and downscaled with a proxy of road map extracted from OpenStreetMap (OSM) [105] (downloaded from https://download.geofabrik.de/asia.html, last access: 21 July 2022). In the dataset, six principal road types, i.e. motorway, trunk, primary, secondary and tertiary, and railway are chosen. The weight factor is defined as a sum of road length of six weighted road types. Weights of six road types are adopted from the downscaling work by Biggart et al. [108] and are shown in Table 4-4. Rail in railways is assumed to have the same weight as the road type motorway. Then the traffic emission flux after applying weight factors is represented as (4-1):

$$emis_{weighted} = emis_{resample} \cdot \sum_{i=1}^{n} rl_i \cdot w_i \quad (4\text{-}1)$$

, where $emis_{weighted}$ represents the weighted emissions, $emis_{resample}$ stands for the resampled emissions before applying weight factors, n is the number of segments of roads in the 1-km downscaling grid, rl_i is the length of one segment and w_i is the road type weight listed as Table 4-4.

Table 4-4. Weights of six road types

Road type	weight
motorway	0.7
trunk	0.5
primary	0.4
secondary	0.25
tertiary	0.15
rail	0.7

The proxy used for downscaling of power plant emission is from the China Emissions Accounts for Power Plants (CEAP) [106]. This dataset utilizes systematic actual measurements monitored by the network of China's continuous emission monitoring systems (CEMS) to develop annual absolute emissions (mega gram, Mg) of particulate matter (PM), sulfur dioxide (SO_2) and nitrogen oxides (NOx) of individual power plants for the years from 2014 to 2017. The annual absolute emissions of power plants in the

year of 2017 are taken as weight factors. More specifically, the weight factors for downscaling power plant emissions of SO_2, PMs and NOx can be derived directly from the CEAP dataset. The weight factors of other pollutants that are not included in CEAP dataset are assumed to be same as that of NOx. The reason behind is that the annual emissions of NOx of individual power plants in the studied region are well correlated to those of SO_2 and PMs in CEAP dataset, and it is assumed that power plant emissions of NOx are also well correlated to those of other pollutants. The CEAP dataset does not provide geolocations of power plants, so geolocations are obtained manually on internet. The exact Chinese names of power plants are first obtained and then the exact addresses can be found on Chinese websites. At the end, the geolocations of power plants are identified using the Google map.

Due to the lack of emissions of individual industrial factories, downscaling of industrial emissions uses the population density, obtained from LandScan 2019, in areas identified as 'industrial' in the land use data. The weighted emission is calculated as (4-2).

$$emis_{weighted} = emis_{resample} \cdot if industrial \cdot polulation \quad (4\text{-}2)$$

$if industrial$ is an identifier to determine whether the landuse in the grid is of industrial or not. There are three possible values for the variable $if industrial$, i.e. 0 – not industrial area, 0.5 – industrial area and power plant both exist, 1 – industrial area exists but power plant not. The detailed identification process is shown in Figure 4-7. The values of $if industrial$ is determined based on the following three sources:

a) the class 'industrial built-up' in land cover dataset RESDC, in which the class 'industrial built-up' includes factories, mines, large industrial zone, oil fields, salt fields, quarries, airports and so on;

b) the industrial class (including workshops, factories, or warehouses) and the air traffic class (including airport, airfield, helipad and apron) in OSM dataset;

c) geolocations of power plants obtained in this study.

The industrial areas in OSM dataset are much sparser than that in RESDC dataset in the studied region. The land use information in OSM dataset is contributed by volunteers all over the world and hence the information of industrial sites may not be identified thoroughly. But it is still a supplement to industrial areas in the dataset of RESDC. In addition, industrial sites in OSM dataset also includes power plants that are later excluded.

The 1-km downscaling grids containing power plants or industrial factories are assigned with weight factors derived from proxies, while other 1-km grids are assigned with zero weight. Therefore, only those 1-km grids containing power plants or industrial factories in a 25-km grid share the total emissions. In rare cases, there is neither power plants nor industrial factories identified in the entire 25-km grid with used datasets, but it does have non-zero industrial or power plant emissions. In this case, all 1-km downscaling grids in that 25-km grid are not weighted.

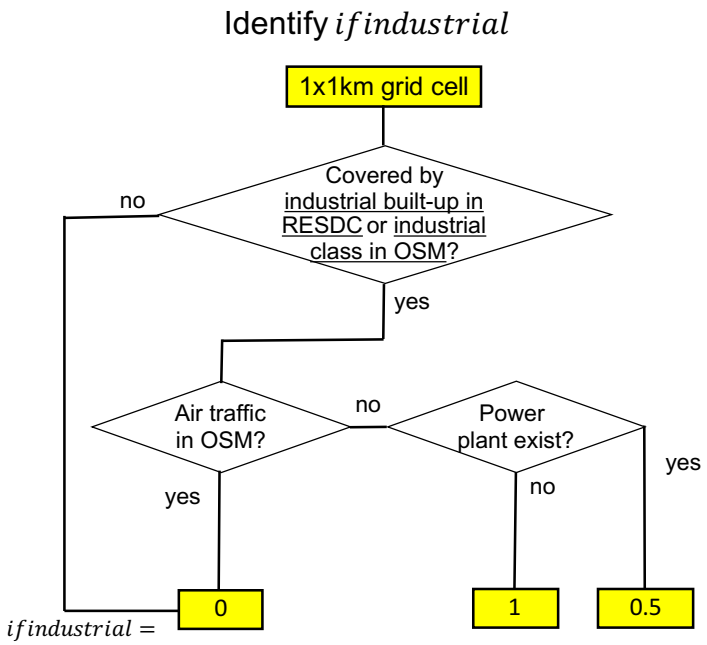

Figure 4-7. Flowchart of identifying the variable $if industrial$.

4.4.2 Downscaled emission

The downscaled emissions of agriculture, transportation and residential sectors are shown in Figure 4-8. It showcases the original emissions, the specific proxies and the downscaled emissions over a 100km x 100km area covering Beijing city center (marked with a white star in Figure 4-8). The maps of original emissions are spatially correlated with the maps of proxies, e.g. agricultural NH_3 emissions in original emission inventory (Figure 4-8a) have lower values on northwest part while cropland fraction (Figure 4-8b) used as the proxy has a similar spatial distribution. After downscaling, it is clearly seen than downscaled emissions retain spatial characteristics of both the original emissions and the proxy used.

For point emission sectors power plant and industrial, results of the downscaled emissions are shown on the entire downscaling region (Figure 4-9). The locations of power plants (Figure 4-9b) corresponds to hotspots of CO emissions in Figure 4-9a. In Figure 4-9c, almost all 25-km grids with emission flux greater than $1x10^{-9}$ $kg/(m^2 \cdot s)$ are successfully downscaled, except several of which the emission flux is not altered due to lack of power plant information. The industrial emissions are more thoroughly downscaled than the power plant emissions (Figure 4-9f).

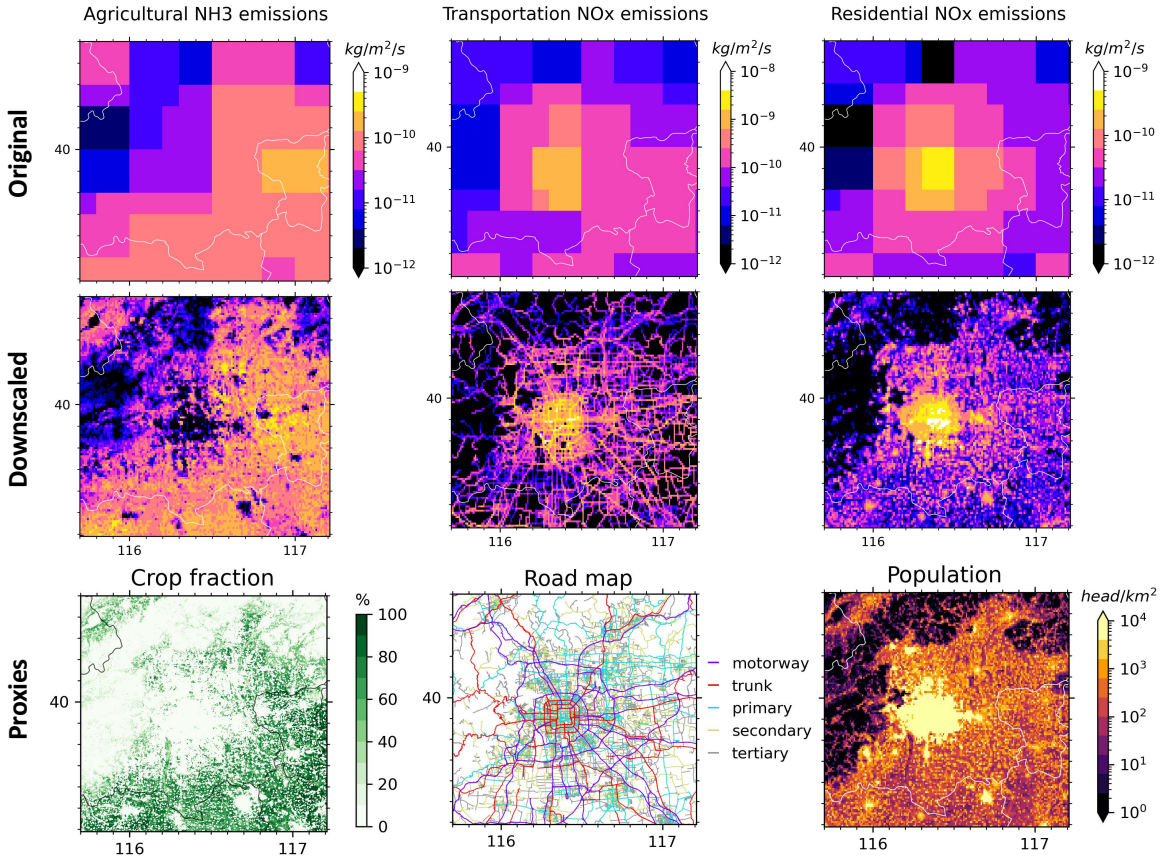

Figure 4-8. First row: original emissions of NH_3 from the source of agriculture and of NOx from the source of transportation and residential at the resolution of 10km. Second row: downscaled emissions corresponding to three plots in the first row. Third row: proxies used for downscaling emissions. The map clip covers the Beijing city and the administrative border is represented by grey lines. Cropland fraction is extracted from Copernicus Global Land v3.0.1 [103]. Road map with five road types is from © OpenStreetMap [105]. Population density is from LandScan 2019 [104].

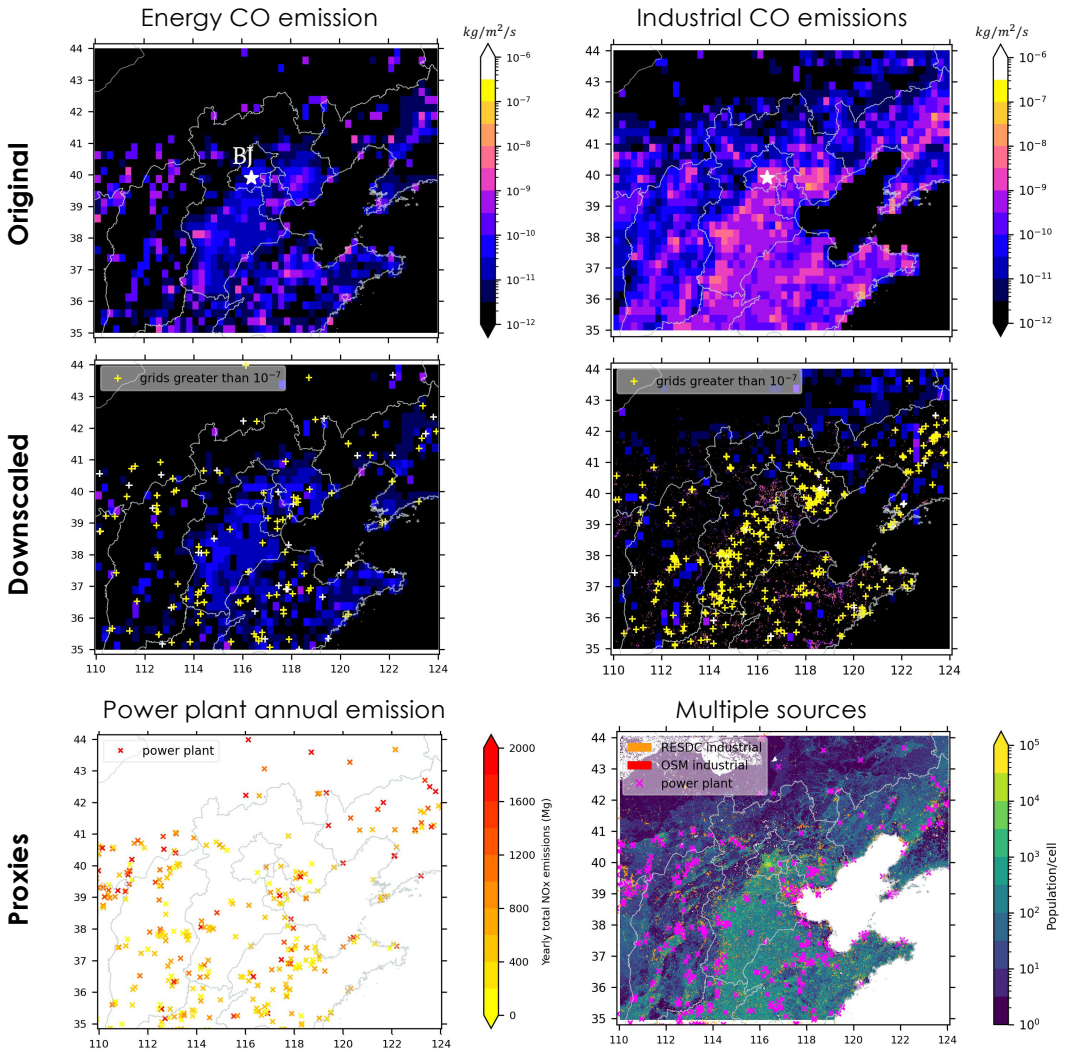

Figure 4-9. Same as Figure 4-8 but here showing CO emissions from energy and industrial in an area slightly larger than Domain 2 in Figure 2-6. The grid size of the original emissions in the upper panel is 25km. In the middle panel, grids with values greater than 1e-7 are marked with colored '+'.

Downscaling uncertainty

Top-down downscaling is based on an assumption that correlative proxies, e.g. land use and population, can explain spatial distribution of emissions at a higher resolution. However, there is intrinsic parts of emissions that cannot be fully explained by proxies. Insufficient and biased information in proxy datasets are also a source of uncertainty in emission downscaling. Table 4-5 shows the changes of total emission rate for NH_3 (agriculture) and CO (the rest of emission sources) before and after downscaling on the entire region as shown in Figure 4-9. The uncertainty of the downscaled NOx emissions is shown in Table A-7.

Table 4-5. Change of total emissions rate (kg/s) of NH_3 for agricultural source and CO for other four emission sources in the downscaled emissions on the entire downscaling region.

Emission source	Emission specie	Original total emission rate (kg/s)	Downscaled total emission rate (kg/s)	Variation (%)
Agriculture	NH_3	43.87	44.05	+0.4
Transportation	CO	224.47	227.54	+1.4
Residential	CO	974.69	980.95	+0.6
Power plant	CO	55.24	54.81	-0.8
Industrial	CO	362.11	375.30	+3.6

4.4.3 Simulation

Experiments

The downscaled emissions are combined with the emissions of four sectors that are not downscaled to form the final anthropogenic emissions inventory used in this study. The experiment applying downscaled emissions is called CTL1_dwns, which is based on the control experiment CTL1. The details of experiments are shown in Table 4-6. The anthropogenic emissions processed for simulations in Domain 3 of two experiments are shown in Figure A-8.

Table 4-6. Experiments for testing downscaled emissions

Experiments	Vertical layers	Emission injection layer	Diurnal/weekly variation	Downscaled emission
CTL1	37	surface	no	no
CTL1_dwns	37	surface	no	yes

Results

In the downscaled emissions, the high values of the emission fluxes are concentrated in smaller grid points, which represent more precise locations of emission sources (Figure 4-10). The simulated NO_2 concentrations in locations covering emission sources increases, especially in the northeast of Beijing (left column in Figure 4-11). Likewise, reduced concentrations of NO_2 are shown in some areas with reduced emissions, e.g.

the west of Beijing, where a reduction of up to 15 ppbv is found all the way to the mountain foothills. Noticeably, there is a long-narrow zone in which the reduction of simulated NO_2 spreads from the west of Beijing to southwest along the mountain foothills (left column in Figure 4-11). When referring to the wind field, there are much stronger northwest wind above mountains, which is originated from the region of Siberia and is typical for the winter time in this region [45]. However, on the low land (the long-narrow area abovementioned), southerly wind is dominated no matter in daytime (stronger) or nighttime (weaker). The mountains block the transport of primary pollutants blown by southerly wind from upstream area. It is indicated that the concentrations in the long-narrow area along the mountains including Beijing not only respond to the local emission changes but also the changes from upstream area. Therefore, the simulated NO_2 concentrations in this long-narrow area show larger sensitivity to the downscaling of emissions than in other areas.

Compared to daytime, the response of the reduction of simulated NO_2 concentrations in the long-narrow area becomes stronger at night. Intuitionally, the blocked air brought by southerly wind to the mountain foot should be less at night because of weaker southerly wind. Less reduction of the simulated NO_2 concentrations in the long-narrow area is therefore expected at night. But in fact, the effect of mountain-plain breeze should not be ignored. In daytime, the plain breeze tends to bring air up to the mountains (southerly wind is observed on the mountains in the upper left plot in Figure 4-11), so it slightly diffuses pollutants brought here by southerly wind. At night, mountain breeze blows against the southerly wind causing the region stagnant, so the blocking effect at night in the long-narrow area becomes larger even with a weaker southerly wind [109, 110]. Additionally, as discussed in Section 4.2.2 and 4.3.2, the shallower PBL at night favoring the accumulation of NOx would amplify the response of simulated NO_2 concentrations to the reduction of emissions, which adds to the blocking effect by southerly wind and mountain breeze in the nighttime. The response of the simulated ozone concentrations to the downscaling of emissions is consistent with that of the simulated NO_2 concentrations but in an opposite way. The two plots in right column in Figure 4-11 clearly show the 'seesaw' relationship between the simulated concentrations of ozone and NO_2 in this region in the winter time. The 'seesaw' relationship is also manifested in the biases of simulated NO_2 and ozone concentrations compared with observations (Figure 4-12).

A reduction of bias of simulated NO_2 and ozone concentrations is observed in the simulation with downscaled emissions (CTL1_dwns) when compared with the control case (CTL1) (Figure 4-12). In the region of Beijing, the mean biases of NO_2 are reduced from the value of 12.6 ppbv in CTL1 to the value of 9.9 ppbv in CTL1_dwns (Figure 4-12a). The mean bias of ozone exhibits similar improvements (Figure 4-12b). In Beijing, the winter season is often characterized by being susceptible to stagnant weather [111]. In total, in 65% of the entire simulation period, the simulated wind speed in Beijing is under 3 m/s (10.8 km/h) and the corresponding value derived from the observation is 79%. NOx ($NO+NO_2$) has a chemical lifetime of around one day in this region in winter time [112]. As a result, the high horizontal heterogeneity of simulated NOx concentrations is expected due to the weak horizontal diffusion and its short lifetime

in winter time. As a result, resolving the emission fluxes in a higher resolution becomes increasingly important if one attempts to simulate the spatial inhomogeneity in the NOx concentrations, specifically during wintertime.

In the experiment with horizontally downscaled emissions to the resolution of 1km (CTL1_dwns), the spatial anomalies of the simulated NO_2 and ozone concentrations are consistent with those in emissions comparing to the control experiment. But in a long-narrow area, extending from the west of Beijing to southwest along mountain foot, NO_2 and ozone respond exclusively strong due to the mountain blocking effect against the southerly wind on the plain. And the nighttime mountain breeze enhances the blocking effect. The biases of NO_2 and ozone simulated in Beijing decrease by 8.5% and 13.5%, respectively, indicating that downscaled emissions well resolve the spatial heterogeneity of anthropogenic emissions in Beijing.

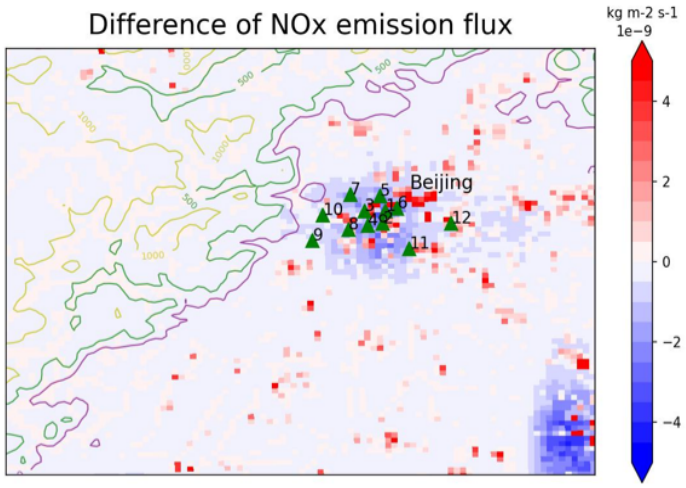

Figure 4-10. Difference of NOx emissions flux between the original emissions and downscaled emissions. Black circles in plots mark Beijing city center. Green triangles labeled by numbers are 12 environmental observation sites. Three terrain height contour lines are plotted with values 250m (purple), 500m (green) and 1000m (yellow). The area shown here expands with longitudes 115.0E-117.2E and with latitudes 39.0N-40.5N.

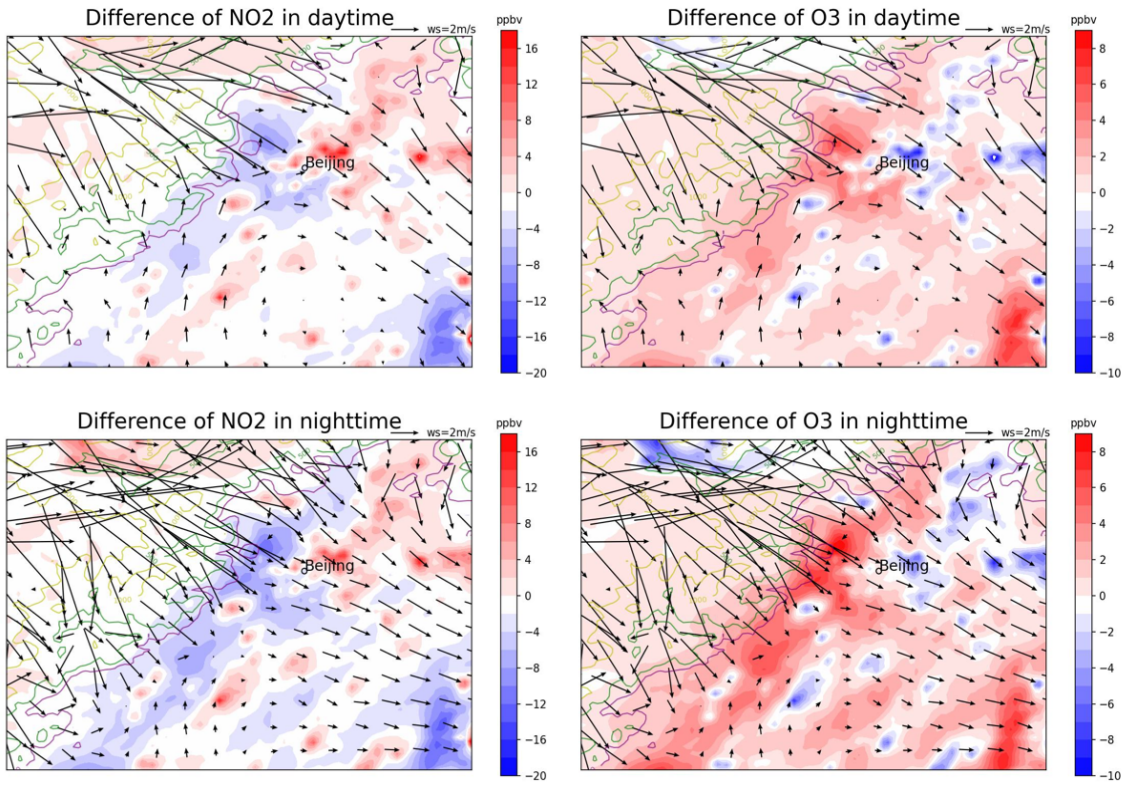

Figure 4-11. Difference of simulated NO_2 mixing ratio (ppbv) between the control case CTL1 and the case CTL1_dwns averaged in daytime (09:00-16:00) and nighttime (19:00-06:00) (left column); idem for ozone (right column). Three terrain height contour lines are plotted with values 250m (purple), 500m (green) and 1000m (yellow). The area shown here expands with longitudes 115.0E-117.2E and with latitudes 39.0N-40.5N. Wind fields are the mean 10-meter surface wind.

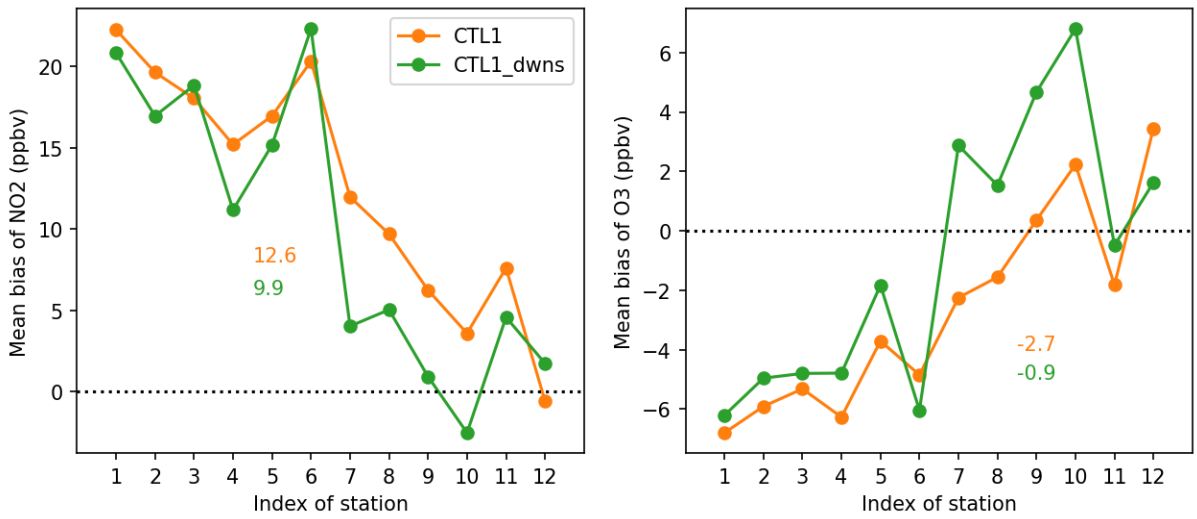

Figure 4-12. Mean bias of 12 environmental observation stations (green triangles in Figure 4-10) in the cases CTL1 (yellow) and CTL1_dwns (green). Dotted horizontal line represents y axis zero. Colored numbers are mean biases of NO_2 and ozone.

4.5 A special case: vast emission reduction during COVID-19 pandemic in China

Publications related to this section:

Gaubert, B., Bouarar, I., Doumbia, T., Liu, Y., Stavrakou, T., Deroubaix, A. M., Darras, S., Elguindi, N., Granier, C., Lacey, F., Müller, J. F., **Shi, X.**, Tilmes, S., Wang, T., & Brasseur, G. P. (2021). Global changes in secondary atmospheric pollutants during the 2020 COVID-19 pandemic. *Journal of Geophysical Research: Atmospheres*, *126*(8), e2020JD034213.

Doumbia, T., Granier, C., Elguindi, N., Bouarar, I., Darras, S., Brasseur, G., Gaubert, B., Liu, Y., **Shi, X**., Stavrakou, T., Tilmes, S., Lacey F., Deroubaix A., & Wang, T. (2021). Changes in global air pollutant emissions during the COVID-19 pandemic: a dataset for atmospheric chemistry modeling. Earth System Science Data Discussions, 1-26.

Stavrakou T., Müller J. F., Bauwens M., Doumbia T., Elguindi N., Darras S., Granier C., Smedt I. D., Lerot C., Von Roozendael M., Franco B., Clarisse L., Clerbaux C., Coheur P. F., Liu Y., Wang T., **Shi X.**, Gaubert B., Tilmes S., Brasseur G. P. (2021). Atmospheric impacts of COVID-19 on NOx and VOC levels over China based on TROPOMI and IASI satellite data and modeling. *Atmosphere*, *12*(8), 946.

Shi, X., & Brasseur, G. P. (2020). The response in air quality to the reduction of Chinese economic activities during the COVID-19 outbreak. *Geophysical Research Letters*, *47*(11), e2020GL088070.

4.5.1 Observation

Starting from January 23, 2020, China puts the whole nation into lockdown to contain the outbreak of COVID-19 pandemic originating from the city of Wuhan in Central China. The air quality of many megacities in China became better responding to the sudden cease of many human activities, i.e. vast reduction of anthropogenic emission. Initially, some pollutant concentrations were observed to reduce significantly, e.g. nitrogen oxides (NOx) and particulate matters (PM). Ground-based routine observations of NOx and $PM_{2.5}$ concentrations collected from more than 800 stations in northern China showed a reduction of 53% (±10%) and 29% (±22%), respectively [39]. In Wuhan, the centre of pandemic outbreak, stricter measures were taken to contain transmission of the CORONA virus. The surface concentrations of NO_2 and $PM_{2.5}$ in Wuhan decreased by 54% (±7%) and 31% (±6%), respectively, according to the data collected from 10 local stations. However, the concentration of ozone increased by a factor of 2.0 (±0.7) in northern China and a factor of 2.2 (±0.2) in Wuhan. Figure 4-13 shows observation of concentrations of NO_2, $PM_{2.5}$ and ozone from ground stations in northern China. In the Pearl River Delta in southern China, the observation of ozone in daytime has shown a reduction of 14% during the pandemic [100].

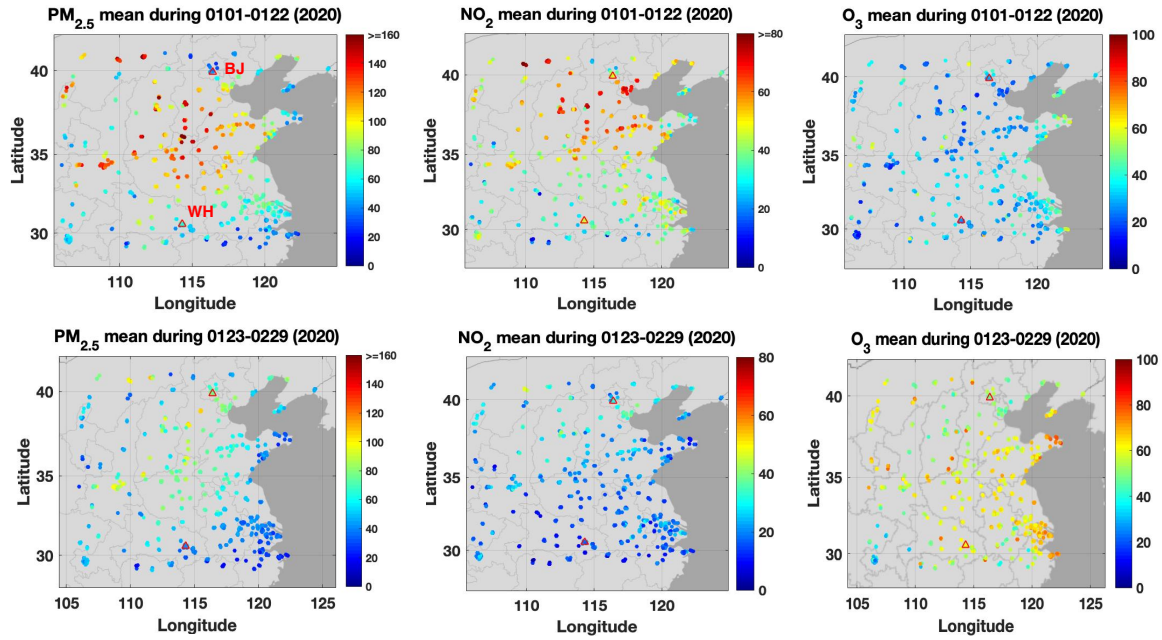

Figure 4-13. Mean concentration (μg/m^3) of $PM_{2.5}$ (left), NO_2 (center), and ozone (right) in Northern China. Upper panels: Averages for the period 1–22 January 2020; lower panel: Averages for the period 23 January–29 February 2020. The empty triangles show locations of the cities of Beijing (BJ) and Wuhan (WH).

4.5.2 Emission reduction

The unprecedented 'clean' atmosphere in China is without a doubt mainly caused by the vase reduction of anthropogenic emissions due to the restriction on human activities. A quantification of reduction of anthropogenic emissions based on emission sources were done by Doumbia et al. [97]. For the whole China in the month of February 2020, the largest reductions of anthropogenic emissions are contributed by the emissions of NOx (-30%), NMVOC (-22%) and SO_2 (-18%). The rest of the world starts to attain the reduction peak of anthropogenic emissions in April 2020 when the global COVID-19 pandemic began (Figure 4-14). The emission adjustment factors designated to apply on emissions in a situation without the occurrence of COVID-19 pandemic are generated based on four emission sources, i.e. traffic (including road, air and ship), industry, residential and power generation. The adjustment factors are compiled into a dataset called CONFORM [97, 113]. Various activity datasets are used to calculate the adjustment factors. In China, the largest reduction of emissions of road traffic emissions around February 10, 2020, which is by 60%. The reduction in industrial emissions in China started from January 23, 2020 and lasted until the beginning of March 2020. After then, industrial emission gradually increases due to the ending of spring festival holiday and the restored industrial production. Power generation experiences as low as 40% reduction in February 2020. Attributed to larger energy consummation of households during pandemic, residential emissions all over the world increase after the pandemic hit specific regions. China has the largest increase in residential emission in the second half of February 2020 by around 10%. The major changes in anthropogenic emissions occur in urban area. In China, Figure 4-15 shows the time series of emission flux of the base case (assume no COVID-19 pandemic) and

covid-19 case (apply adjustment factors to the base case). The reduction of Beijing, the capital of China, has different characteristic from other cities. It sharply decreases right after lockdown on January 23, 2020 and keep a low level of NOx emissions until the end of May, while other cities slowly recover from the middle of February.

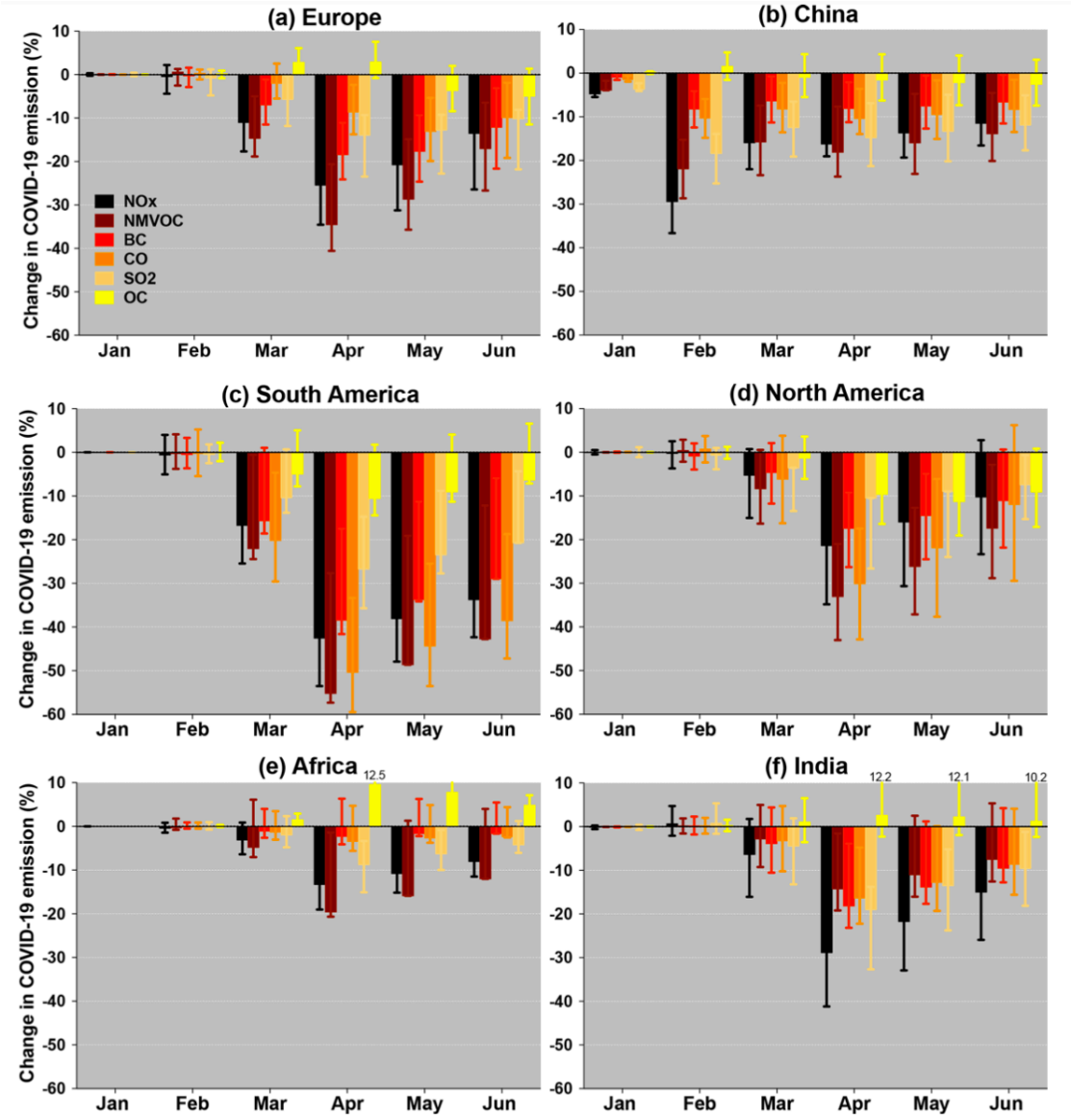

Figure 4-14. Percentage change in total emissions (combination of emissions from ground transportation, industry, power, residential and shipping) as a function of month for selected regions: (a) Europe (35–70° N, 20° W–20° E), (b) eastern China (20–45° N, 80–125° E), (c) South America (60° S–20° N, 90–35° S), (d) North America (20–50° N, 135–35° W), (e) Africa (40° S–30° N, 20° W–40° E) and (f) India (05–30° N, 60–90° E). The vertical lines show the uncertainties associated with the estimated emission adjustment factors [97].

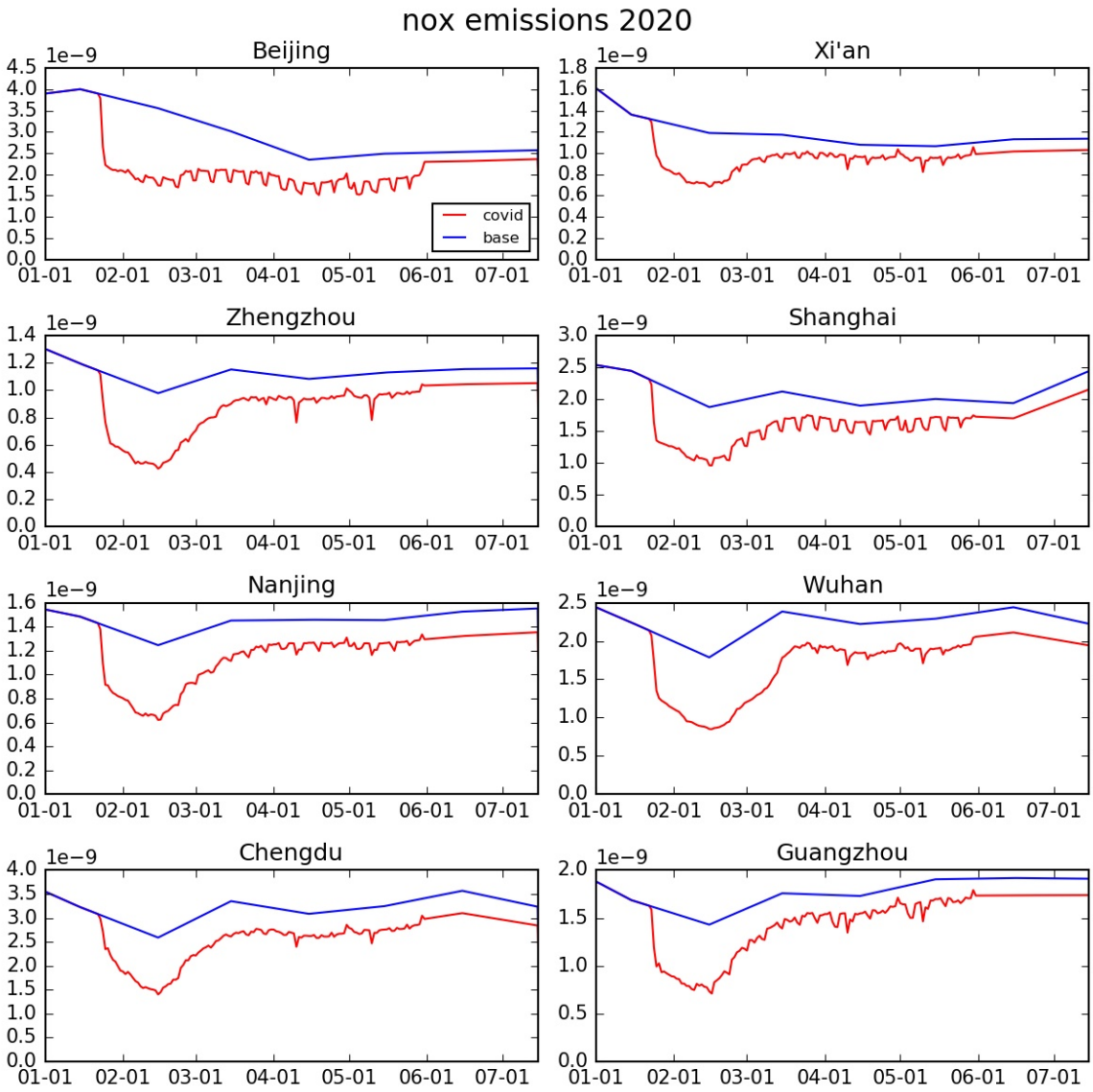

Figure 4-15. Reductions of emission flux ($kg/(m^2 \cdot s)$) of NOx from January 2020 to July 2020 in eight large cities in China derived with daily adjustment factors in the dataset CONFORM.

4.5.3 Model configuration

Common settings

The simulation setting for simulating the COVID-19 pandemic period with the model WRF-Chem is different from the commonly used one described in Section 2.2.2. First of all, only one domain with a horizontal resolution of 12km is adopted, covering the whole eastern part of China and including adjacent ocean area. The domain map is shown in Figure 4-16. There are in total 38 vertical layers with the top layer at the pressure of 50hPa. The whole simulation period is from January 1, 2020 to February 29, 2020 and the first ten days are taken as spin-up period. In order to take urban effects into account, the single urban canopy model is turned on. The chemistry calculation is again a combination of chemical mechanism MOZART-T1 and photolysis model TUV. The important parameterizations used in the model are listed in Table 4-7.

Table 4-7. Parameterizations used in the COVID-19 experiment

	Parameterization	Scheme
Physical	Microphysics	Thompson graupel scheme
	Cumulus	Grell-Freitas [114]
	Radiation	RRTMG
	Planetary boundary layer	YSU
	Surface layer	Revised MM5 Monin-Obukhov scheme
	Land surface	Unified Noah land-surface model
	Urban physics	Single layer urban canopy model [115]
Chemical	Mechanism	MOZART-T1
	Aerosol	GOCART
	Photolysis	TUV photolysis

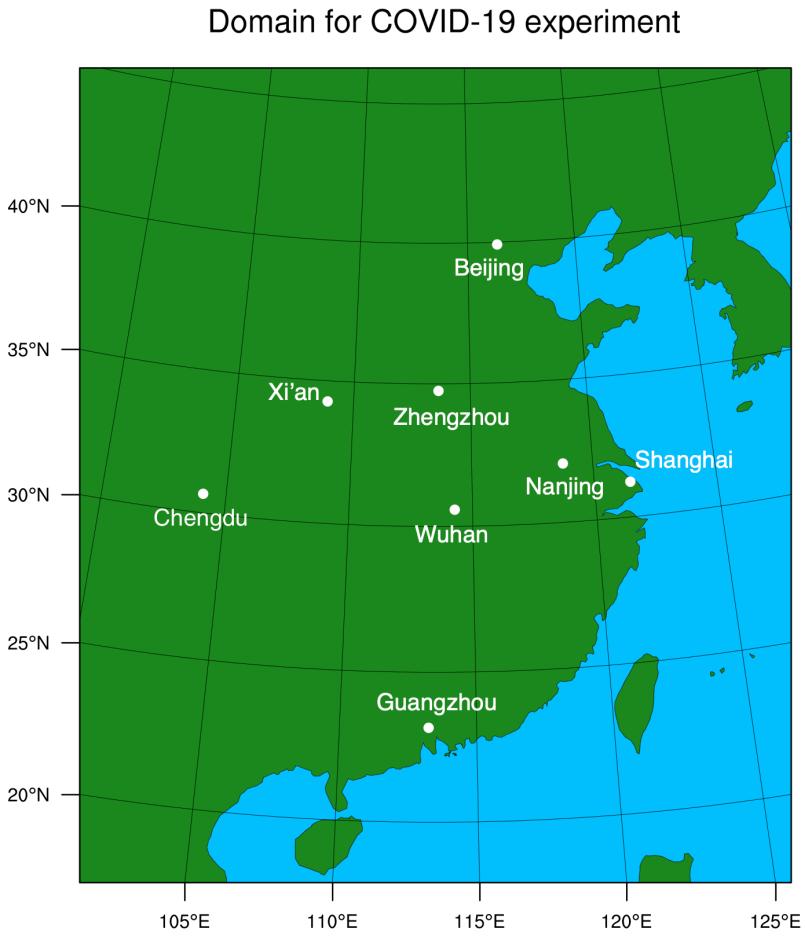

Figure 4-16. Domain for the COVD-19 experiment. White dots mark out eight megacities.

Emissions

The vast reduction of anthropogenic emissions during the pandemic is accounted for by the reductions in the surface anthropogenic emissions and the aircraft emissions. The emissions on surface are from the anthropogenic emission inventory CAMS-GLOB-

ANT v4.2-R1.1 as described in Section 2.2.2, but in the year of 2020. The aircraft emissions are from a separate CAMS dataset called CAMS-GLOB-AIR v1.1, which provides the global aircraft emissions of CO, SO_2 and NO for the surface up to 15km. In model, aircraft emissions are injected to the first to 34th vertical layers. The original CAMS emissions in the year 2020 are developed by assuming no occurrence of the pandemic. The reduction factors for surface anthropogenic emissions and aircraft emissions are from the CONFORM dataset mentioned in Section 4.5.2. Only monthly reduction factors are provided for aircraft emissions on the country level. The aircraft emissions in February are reduced by 54% compared with January. The emissions on surface are reduced on daily basis for five sectors, i.e. industrial, power plant, residential, shipping and transportation. The anthropogenic emissions of NOx of all sectors on surface after the outbreak of COVID-19 pandemic are calculated with the reduction factors in CONFORM dataset and the results in eight megacities are shown in Figure 4-15. The anthropogenic emissions of CO and NO in the whole domain are showcased in Figure A-9. Non-anthropogenic emissions, e.g. biomass burning and biogenic emissions are the same setting as that described in Section 2.2.2.

4.5.4 Simulation

Experiments

With the provided reduction factors of anthropogenic emissions amid COVID-19 pandemic in China, simulations are designed to interpret the change of atmospheric compositions in response to the vast emission reduction. A control case is conducted without implementing the reduction factors, simulating the usual scenario. Another case, named COVID case, is a simulation with reduced emissions due to nation-wide lockdown during the pandemic. Daily reduction factors start to be applied on emissions from January 23, 2020. The main differences of two cases are shown in Table 4-8.

Table 4-8. Experiments for testing the COVID effect

	Control case	**COVID case***
Time period	From 2020-01-10 to 2020-02-29	From 2020-01-23 to 2020-02-29
Anthropogenic emissions	non-COVID emissions	COVID emissions

* The COVID-19 case is a restart run starting with the Control case output at 00:00 (UTC) on Jan 23, 2020.

Result

Figure 4-17 shows the simulation results averaged over the period from January 23 to February 27, 2020. The upper panels show the surface mixing ratios of NO_2 and ozone simulated with reduced emissions. In winter time, less solar radiation causes less ozone production. Instead, high concentration of NOx in the atmosphere titrates ozone. The concentrations of ozone in populated urban areas are lower than in rural areas. The chemical regime of ozone production in urban area with high NOx levels is 'VOC-limited' or 'NOx-saturated'. Especially in North China Plain (NCP) including Beijing,

Tianjin and Hebei province, in winter large emissions from coal burning for winter heating, dense urban settlements and unfavorable topography for pollution diffusion make this region easily trap primary pollutants and accumulate high concentration of NOx. Plus, the low level of HOx (HO2+OH) in this region cannot sufficiently oxidize the high loading of pollutions. Except for NCP, other relatively smaller urban agglomerations, e.g. Yangtz River Delta (YRD), also have the similar property of atmospheric chemistry. When most of human activities suddenly cease during the pandemic, the concentration of NOx in atmosphere quickly decreases as shown in the middle left panel of Figure 4-17. Largest reduction of NO_2 concentrations happens in NCP and YRD, which is as low as -10 ppbv. In Southern China, a reduction of around -4 ppbv is sparsely observed in large cities, e.g. Wuhan (the outbreak center of the pandemic), Chongqing, Guangzhou. Theoretically, a reduction of NOx level in NOx-saturated atmosphere causes an increase of ozone concentration as less ozone is titrated by NOx. So the areas with large NO_2 reduction and with large ozone increase almost spatially overlay (middle row in Figure 4-17). But in the rural areas in Southern and Southwest China, ozone concentrations slightly decrease by 1-3 ppbv. To be noted, ozone concentrations in large cities in Southern China still increase. These two regions, called Region 1 and Region 2, with different ozone responses to emission reductions are shown in the ozone difference map in the middle right panel of Figure 4-17. Figure 4-18 shows the time series of the region-averaged NO_2 and ozone concentrations, respectively, simulated in the control case and the COVID case. In two regions, the simulated NO_2 concentrations in the COVID case is reduced by 28% and 25% in Region 1 and 2, respectively, compared to the control case. The simulated ozone increases by 22% in Region 1, while slightly decreases by 0.4% in the Region 2.

In NOx-limited areas in the NOx-limited regime, i.e. rural areas, the reduction of NOx emissions directly leads to the reduction of ozone formation, because the photolysis of NO_2 by the reaction (1-19) produces $O(^1D)$ that combines with one oxygen molecule to form ozone by the reaction (1-20). NOx emissions are related to intensive human activities in large cities, and while regions with low concentrations of NOx are normally covered by high percentage of vegetation, especially in Southern China, where evergreen plants emit large quantity of isoprene in winter [116]. Isoprene emissions accounts for most of VOCs emissions in rural areas [117]. In the low-NOx condition, an important loss of isoprene is by reacting with ozone (ozonolysis) [24]. So when ozone level is reduced in Southern China, isoprene in vegetated region increase as shown in the bottom right panel of Figure 4-17. For the response of hydrogen radicals HOx ($OH+HO_2$) to the reduced NOx emission during the pandemic, the spatial differentiation between the HOx-increase region (south and southwest) and the HOx-decrease region (north) is very similar to that for ozone response. The responses of HOx are also different in two chemical regimes, i.e NOx-saturated and NOx-limited. In high NOx condition, HOx source is dominated by the photolysis of formaldehyde (HCHO) and the photolysis of nitrous acid (HONO) [118]. The study by Li K. et al [119] has shown that the dominant chemical source of HOx in NCP changes from HONO photolysis before lockdown to HCHO photolysis after lockdown (Figure 4-19), because the reduction of NOx emissions reduces the production of HONO:

$$2NO_2\ (uptake) + H_2O \rightarrow HONO + HNO_3(s) \quad (4\text{-}3)$$

and the sink of HOx by the reaction in (1-24). Increased HOx level oxidizes more VOCs and produces secondary HCHO. Then the photolysis of HCHO

$$HCHO + 2O_2 + hv \rightarrow CO + 2HO_2 \quad (4\text{-}4)$$

produces more HOx and further boosts oxidation of VOCs to form HCHO. Hence, a chemical cycling of HCHO continuously increases the HOx level after the cycle is initiated by the reduction of NOx emissions in the NOx-saturated urban areas. Especially in urban areas with large emissions of both NOx and VOCs, e.g. cities along the southeast coast of mainland China and in Northwest Taiwan, the significant increase of HOx (bottom left panel of Figure 4-17) is attributed to much larger VOC emissions and stronger solar radiation to generate more HCHO. The region with reduced HOx level is controlled by NOx-limited region, where the source of HOx is photolysis of ozone by the reactions (1-29) and (1-30). So the slight reduction of HOx is due to the slight reduction of ozone in this region.

In summary, NOx emissions decreased significantly during the COVID-19 pandemic, and corresponding ozone responses behaves differently in the polluted areas (mainly North China) and the rural areas (mainly South and Southwest China). This is due to the different dominating reactions of ozone chemistry under the different chemical regimes, which depends on the level of NOx. In polluted areas with the 'NOx-saturated' chemical regime, ozone concentrations increase as NOx levels decrease. And in rural areas with the 'NOx-limited' chemical regime, ozone concentrations decreases slightly with reduced NOx level. In the "NOx-saturated" area, mainly in Northern China, HOx levels increase concurrently with ozone during the pandemic. In the study by Li K. et al, it was emphasized that when NOx is significantly reduced during the pandemic, the dominate production pathway of HOx changes from NO_2 uptake to HCHO photolysis. The reaction cycle of HCHO and HOx boosts the increase of HOx production: photolysis of HCHO produces HOx, which oxidizes VOCs to produce more HCHO. The increase in HOx then enhances ozone production.

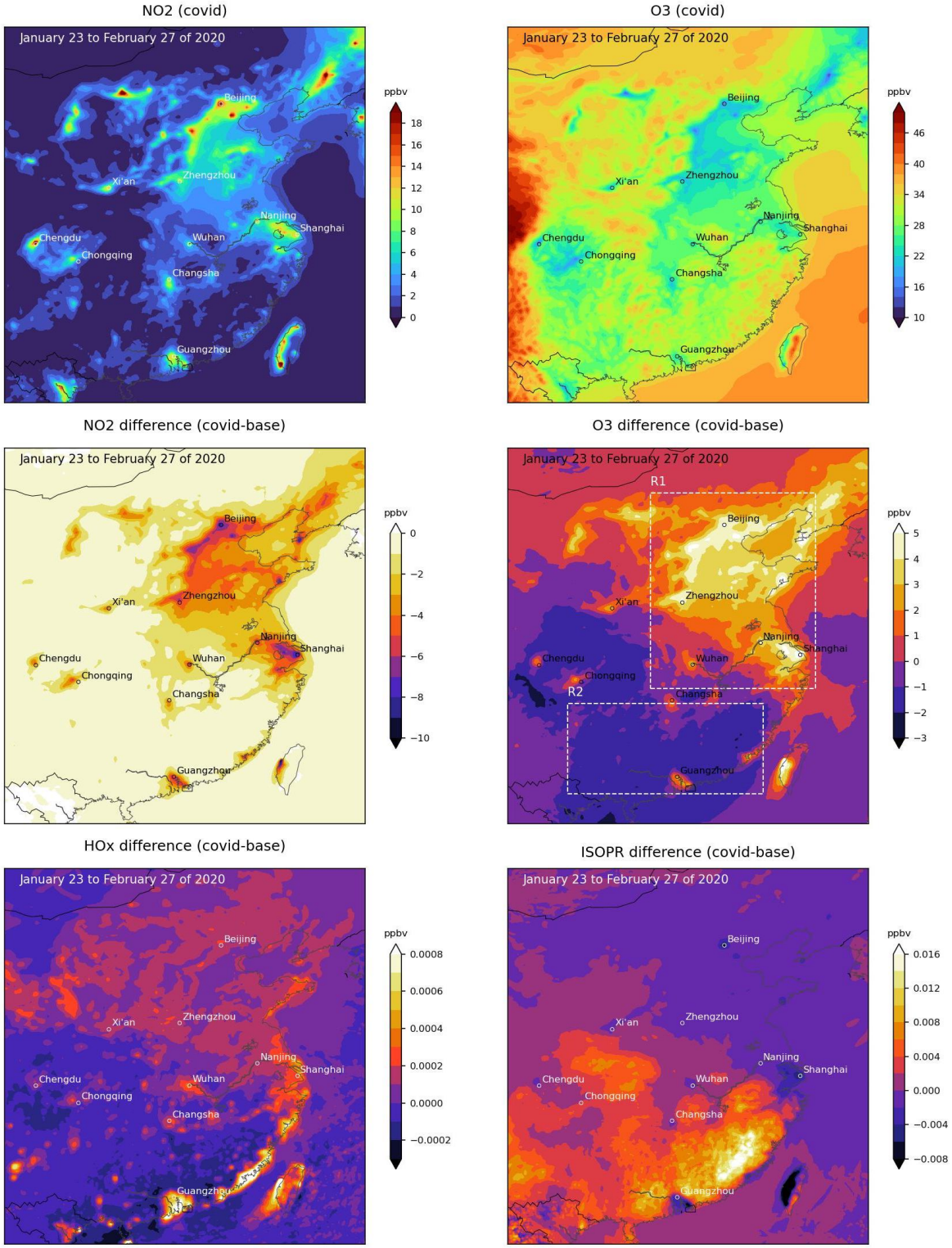

Figure 4-17. Upper row: spatial distributions of simulated NO_2 and ozone in the COVID case. Middle row: anomalies of simulated NO_2 and ozone between the COVID case and control case. Lower row: idem but for HOx and isoprene (ISOPR). White boxes in the right plot of the middle row frame two regions, named R1 and R2, which have distinct ozone responses to the emission reductions during the pandemic. Data is average over a period from January 23, 2020 to February 27, 2020.

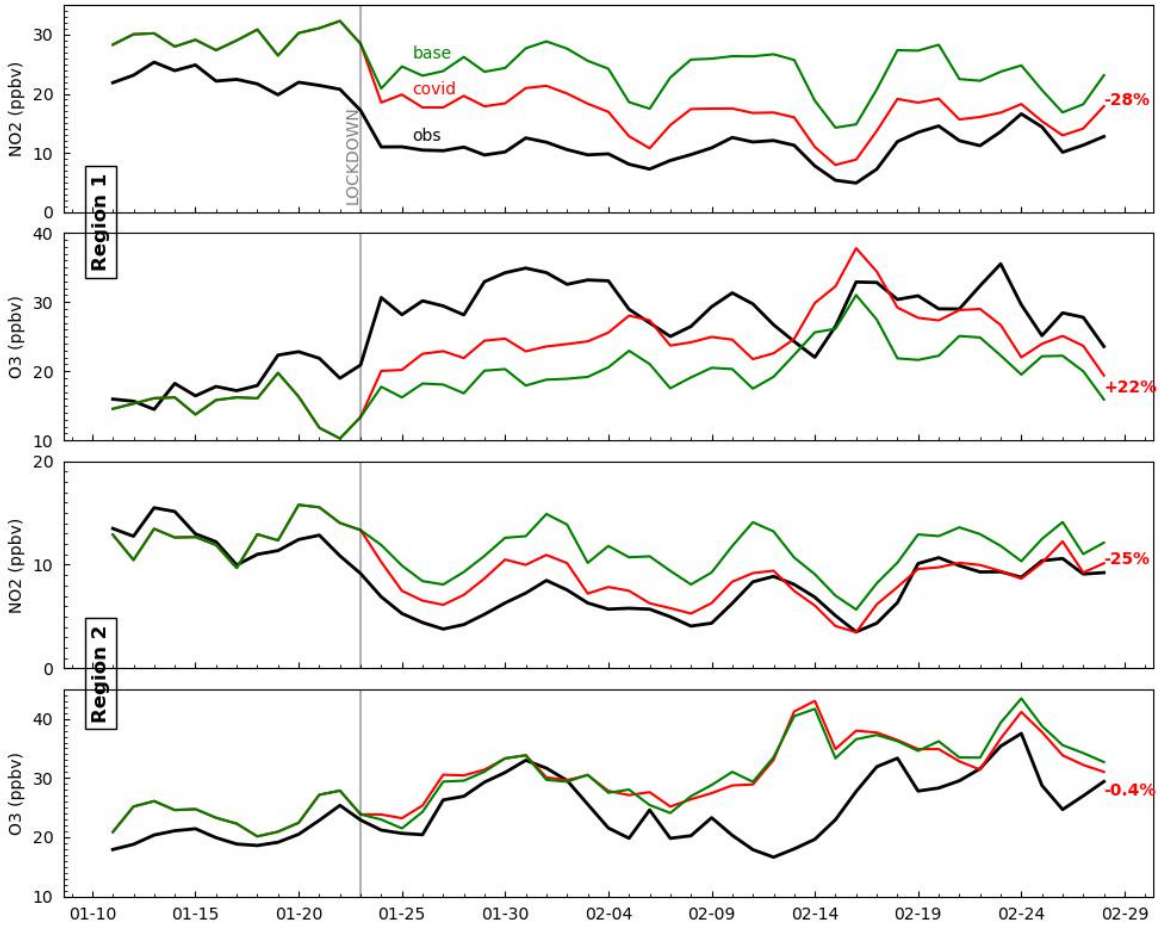

Figure 4-18. Time series of observations (black line) and simulations (green and red line) of NO_2 and ozone averaged in the Region 1 and the Region 2 shown in Figure 4-17. The red number in each plot represents the average difference of simulated NO_2/ozone between the COVID case and the control case after the lockdown on January 23, 2020 (marked with vertical grey lines).

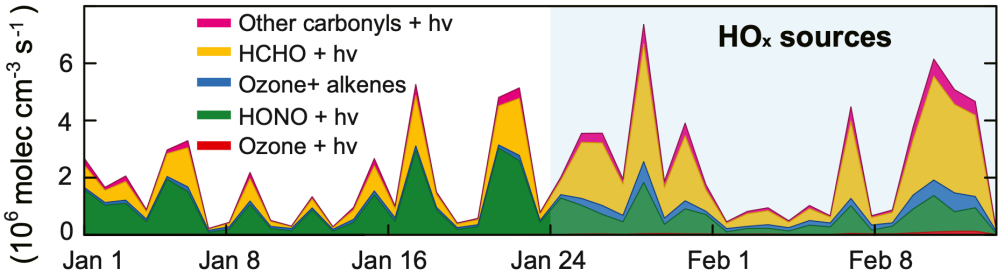

Figure 4-19. The chemical sources of HOx in Beijing simulated by the model GEOS-Chem in January and February of 2020. The shadow area covers the period of the COVID-19 lockdown [119].

4.6 Conclusions

This chapter investigates the ozone responses to different formulations of anthropogenic emissions including a special case focusing on the early period of the COVID-19 pandemic in China with a vast reduction of anthropogenic emissions.

The modeled concentrations of ozone and NOx show greater variability at night than during daytime in response to the vertical (Section 4.2) and temporal (Section 4.3) redistribution of emissions. By injecting emissions from the surface up to 500 meters, the concentration of simulated surface ozone decreases by 75% at night and by 19% during the day. When the emissions are redistributed more in daytime than in nighttime to mimic the real diurnal cycle of anthropogenic emissions, the calculated concentrations of surface NO_2 and ozone are more significantly affected at night too. The low diffusion capacity of the nocturnal boundary layer in winter is often not sufficient to diffuse the emitted NOx efficiently and therefore leads to NOx accumulation and hence ozone depletion in the surface layer at night. When NOx emissions are reduced to a level that can be sufficiently diffused in the nocturnal boundary layer, the ozone level even starts to increase in the nighttime instead of staying low in the case of high NOx emissions.

In order to see the impact of high-resolution emissions to ozone response, the anthropogenic emission is downscaled to a resolution of 1 km by a top-down method developed based on emission-source-based weight factors for specific emissions by proxies (Section 4.4). The simulation with downscaled emissions lowers the bias of NO_2 by 9% and the bias of ozone by 14% in the city of Beijing. The simulated NO_2 in a long-narrow zone, from Beijing to the southwest along the western mountains, shows exclusively large sensitivity to the downscaling of emissions due to the low diffusion capacity of this zone by the blocking of southerly wind by the western mountains. The blocking is enhanced at night by the mountain breeze.

The last part of this chapter is a separate simulation study on the ozone responses to the vast emission reductions during the COVID-19 pandemic in China in the first two months of 2020 (Section 4.5). Both the observed and simulated level of NOx was significantly reduced after the outbreak of the pandemic. In the polluted northern China, the observed NOx concentrations decreased by 53%. Observations also show that ozone leveled up by a factor of 2 in Northern China. However, ozone concentrations in rural areas with low NOx emissions slightly decreased, for example by 0.4% in Region 2 shown in Figure 4-17. The different responses of ozone to large NOx emission reduction during the pandemic depends on the chemical regimes of the regions. In 'NOx-limited' regime, mostly in rural area, the reduction of NOx limits ozone production. While in 'NOx-saturated' regime, i.e. in polluted urban areas, ozone is reduced due to less NOx titration. In the polluted region with increased ozone level, the model also captured HOx increase, which is also simulated by previous studies and is attributed to the change of production pathway of HOx in response to the significant reduction in NOx emissions.

In conclusions, the surface ozone and NO_2 concentrations respond to the vertical/temporal redistribution of emissions more intensively at night than in daytime during wintertime in the region of Beijing, as the winter nocturnal boundary layer in the region of Beijing has very low diffusion capacity. Emissions with increased spatial heterogeneity improve model simulations of surface ozone in the region of Beijing, especially a long-narrow zone along the mountains. The increase in ozone concentrations in response to significant reduction in NOx emissions during the first two months of the COVID-19 pandemic in China is not only attributed to the reduction of NOx titration, but also the enhanced ozone production by increased HOx level.

5 Conclusions

The thesis focuses on the winter ozone behavior in the polluted urban boundary layer. The studied regions are mainly based on the city of Beijing, the capital of China, and its surrounding areas. Three forcing factors are identified as important in determining the ozone budget in polluted winter boundary layer, which are *large-scale wind, urban heating, anthropogenic emissions*. At first, three scientific questions are raised in the introduction:

- How do large-scale winds influence the ozone behavior during wintertime?
- What is the role of urban heating in controlling the fate of ozone and NOx during the day-to-night transition?
- How does ozone respond to anthropogenic emissions?

The first part of Chapter 2 (Section 2.1) describes the background of the city of Beijing, including topography, climate, air pollution, emissions and urban heat island effect, with the emphasis on wintertime. Beijing is surrounded by mountainous areas to the north and west and by plain to the east and south. The strong northerly wind prevails during wintertime in this region under the control of East Asia winter monsoon. High demands of heating in winter make Beijing subject to large quantity of air pollutant emissions and urban heat emissions. Then the regional chemical transport model WRF-Chem and the specific configurations for studies in this thesis are covered in the second part of Chapter 2 (Section 2.2). Numerical experiments designed for the investigations of three scientific questions are summarized at the end of Section 2.2. Chapter 3 investigates the first two scientific questions about large-scale wind and urban heat, namely the mechanical forcing and the thermal forcing of the boundary layer turbulence. The last scientific question regarding anthropogenic emissions is discussed in Chapter 4, which is ended with a special case on ozone responses to vast emission reductions following the outbreak of COVID-19 pandemic in China in the first two months of 2020. Next, main conclusions of this thesis are presented with answers to three scientific questions.

- **Question 1: How do large-scale winds influence ozone behavior in winter?**

Due to ozone depletion by high-loading NOx, ozone concentrations in the urban boundary layer are lower than in the surrounding rural areas and in the vertical portion at higher altitudes in winter. In most cases, the atmospheric processes, advective transport and vertical turbulent mixing, cause the increase of ozone concentrations in the urban boundary layer. The influence of advective transport by the northerly wind on the increase in urban ozone concentrations is greater than that by the southerly wind due to the higher wind speed of northerly wind and the higher ozone concentrations in the rural mountainous areas to the north and west of Beijing. Large-scale wind, as a mechanical force, also generates turbulent mixing in the urban boundary layer, which increases the ozone concentrations in the surface layer. Under

the winter monsoon's control, invasions of massive strong northerly wind often occur. During these invasion events, the ozone level in the urban boundary layer is significantly enhanced by a factor of up to 1.9 (+19ppbv) occurring in the nocturnal time, while the NO_2 level drop by up to 84% (-44ppbv). It is concluded that the nocturnal ozone enhancement in winter in the urban area of Beijing is mainly explained by the increased mechanical turbulent mixing during the invasions of strong northerly wind.

- **Question 2: What is the role of urban heating in controlling the fate of ozone and NOx during the day-to-night transition?**

As solar radiation fades during the day-to-night transition, urban heat partially compensates for the loss of radiative energy from the ground surface, ensuring that the ground surface is warmer than the atmosphere above. This maintains a shallow convective layer at the bottom of the urban boundary layer, which significantly increases the diffusion capacity of the urban boundary layer for air pollutants. In contrast, without the urban heat effect, the boundary layer may develop the lowest eddy diffusivity over the course of the day during the day-to-night transition, as the rapid transition from the 'unstable' condition to the 'stable' condition causes the turbulent mixing to be thermally suppressed and the not yet established wind shear in the residual layer indicates that there is fairly small mechanical source for turbulent mixing. In the simulations without urban heat effect in this study, the eddy diffusivity decreases by 77%-94% during the day-to-night transition, reaching the lowest values of 0.5 to 1.6 m^2/s. As a result, NOx accumulates quickly and the NOx concentrations peak high during the day-to-night transition, while ozone is depleted sharply to very low levels. This is not consistent with the NOx and ozone observations. However, the simulation with the urban heat effect in this study mitigates the accumulation of NOx (the bias of NO_2 is reduced from +75% to +6%) as well as ozone depletion (the bias of ozone is reduced from -68% to +0.7%) during the day-to-night transition.

- **Question 3: How does ozone react to anthropogenic emissions?**

The anthropogenic emissions formulations tested in this study include vertical injection, diurnal/weekly temporal redistribution, and downscaling (horizontal redistribution). Ozone and NOx concentrations respond more strongly to changes in anthropogenic emissions in the nocturnal boundary layer than during the day. Spatially, a long-narrow region along the mountain foot southwest of Beijing is more sensitive to the downscaled emissions compared to other regions because of reduced diffusion capacity caused by the blocking of the southerly wind by the western mountains. It is concluded that the response of ozone concentrations to changes in anthropogenic emissions is amplified by the reduced diffusion capacity of the boundary layer in the polluted region in winter. As a special case, a natural experiment of emission reductions is discussed in the end: the vast emission reductions following the outbreak of the COVID-19 pandemic in China in the first two months of 2020. In response to 30% reduction in NOx emissions in China in February 2020, the ozone concentrations in polluted urban areas increased, for example by a factor of 2 in Northern China, while in rural areas ozone concentrations decreased slightly, on average, by 0.4% in the

southern part of China, which is mostly covered by vegetation. The explanations of the different ozone responses are based on the chemical regime of ozone production. In 'NOx-saturated' regime, which mainly represents the polluted urban areas, ozone concentrations increased due to reduced NOx titration and increased ozone production due to the simultaneously increased HOx level. In contrast, the decrease of NOx concentrations directly limits ozone production in the rural areas represented by the 'NOx-limited' regime.

6 Outlook

Ozone, as a secondary pollutant, is the focused chemical species in the urban boundary layer in summer due to its high ambient abundance. During the cold wintertime, the solar radiation associated with ozone production is much reduced and thus a low level of ozone is expected. Its behavior in the winter boundary layer are quite different from those in summer. Investigating the related atmospheric processes that mainly controls ozone fates in the polluted and cold winter boundary layer help understand potential ozone responses to meteorological anomaly, urbanization and pollutant emissions.

With changing climate, weather conditions tend to be increasingly intensified in an unexpected way. For example, extreme cold winters in China are associated with the warming Arctic and the strengthened Siberia High [120]. Remotely transported high-ozone plume from the mountainous area to the urban areas of Beijing by the enhanced winter monsoon can significantly increase the surface ozone concentrations at night that can be even higher than the daytime maximum. Urban heat increase in the development of urbanization perturbs the boundary layer stability and local wind intensity [121]. The study in this thesis give insights into the changes of ozone budget in the winter boundary layer disturbed by urban heat. Due to the efforts of emission mitigation in China, the ozone trend has been positive over the last decade [122], which enhances the ozone pollutions in summer and, in recent years, also in the late winter [119]. Combined with the abnormally enhanced winter monsoon, the continuing increase of urban heat release and the mitigation of pollutant emissions, ozone pollutions might occur and increase in winter in cities similar to Beijing.

Following the still unknown area in this work, further work can be proceeded as follows:

- To identify winter ozone enhancement events in extreme cold winters and evaluate their occurrence, intensities and formation mechanisms.
- To simulate ozone with IPCC warming scenarios with extreme meteorological anomalies, for example much enhanced winter monsoon.
- To simulate the effect of urban heat in an explicit way and quantify the effect on surface ozone and emitted pollutants.
- To seek for a better formulation of anthropogenic emission in order to improve the model simulation in the studied region.

Appendixes

Appendix for Section 2.2.3

Mean bias (MB) is calculated by

$$MB = \frac{\sum_{t=0}^{T}\sum_{n=0}^{N} M_{n,t}}{N \cdot T} - \frac{\sum_{t=0}^{T}\sum_{n=0}^{N} O_{n,t}}{N \cdot T} \quad \text{(A-1)}$$

, where $M_{n,t}$ denotes the model value at site n and on the hour t. And $O_{n,t}$ is the observation. MB is the mean of bias of individual site n and hour t on all sites N and across all time T. In order demonstrate bias of wind vector, the root-mean-square error of vector wind difference (VMD) is defined as

$$VMD = \sqrt{\frac{\sum_{t=0}^{T}\sum_{n=0}^{N}\left(\left(UM_{n,t} - UO_{n,t}\right)^2 + \left(VM_{n,t} - VO_{n,t}\right)^2\right)}{N \cdot T}} \quad \text{(A-2)}$$

The west-east component of wind is denoted by UM for model and UO for observation and the south-north component by VM for model and VO for observation. Another one is root-mean-square deviation (RMSD) defined as

$$RMSD = \sqrt{\frac{\sum_{t=0}^{T}\sum_{n=0}^{N}\left(M_{n,t} - O_{n,t}\right)^2}{N \cdot T}} \quad \text{(A-3)}$$

Table A-1. Comparison of layer heights under 1520m in the settings of total 37 model layers and total 47 model layers. AGL represents the altitude above ground level.

Index_37	AGL (m)	AGL (m)	Index_47
0	0.00	0.00	0
		22.83	1
1	45.72	45.72	2
		74.89	3
2	104.17	104.15	4
		141.25	5
3	178.53	178.49	6
		225.39	7
4	272.59	272.51	8
		331.37	9
5	390.77	390.61	10
		463.80	11
6	537.79	537.55	12
		627.45	13
7	718.77	718.16	14
		827.02	15
8	939.23	937.15	16
		1067.23	17
9	1204.53	1199.56	18
		1353.18	19
10	1518.05	1510.17	20

Table A-2. A list of CAMS sectors.

CAMS sector	Description
agl	Agricultural livestock
ags	Agricultural soils
awb	Agricultural waste burning
ene	Power generation
ind	Industrial processes
res	Residential
tnr	Off-road transportation
tro	road transportation
fef	Fugitives
slv	Solvents
swd	Solid and water waste
shp	Ships

Table A-3. Mapping from chemical species in the CAMS inventory (lower case letters) to that in the chemical scheme MOZART-T1 (upper case letters).

MOZART-T1	Meaning	CAMS
CO	carbon monoxide	co
NO	nitric oxide	0.9*nox
NO2	nitrogen dioxide	0.1*nox
SO2	sulfur dioxide	0.975*so2
NH3	ammonia	nh3
C2H5OH	ethanol	0.85*voc1
CH3OH	methanol	0.15*voc1
C2H6	ethane	voc2
C3H8	propene	voc3
BIGALK	lumped alkanes C>3 (C5H12)	voc4+voc5+voc6+voc18+voc19
C2H4	ethene	voc7
C3H6	propene	voc8
ISOP	isoprene (C5H8)	voc10
BIGENE	lumped alkenes C>3 (C4H8)	voc12
TOLUENE	toluene (C7H8)	voc14
CH2O	formaldehyde	voc21
CH3CHO	acetaldehyde	voc22
CH3COCH3	acetone	0.2*voc23
MEK	methyl ethyl ketone (C4H8O)	0.8*voc23
HCOOH	formic acid	0.5*voc24
CH3COOH	acetic acid	0.5*voc24
CH3CN	acetonitrile	0.002*co
HCN	hydrogen cyanide	0.003*co
APIN	alpha-pinene (C10H16)	voc11
BENZENE	benzene (C6H6)	voc13
XYLENE	lumped xylenes (C8H10)	voc15+voc16+voc17
C2H2	ethyne (acetylene)	voc9
OC	organic carbon	oc
BC	black carbon	bc

Table A-4. A list of VOCs in CAMS inventory

VOCs in CAMS	Name
voc1	alcohols
voc2	ethane
voc3	propane
voc4	butanes
voc5	pentanes
voc6	hexanes
voc7	ethene
voc8	propene
voc9	ethyne
voc10	isoprenes
voc11	monoterpenes
voc12	other alkenes and
voc13	benzene
voc14	toluene
voc15	xylenes
voc16	trimethylbenzenes
voc17	other aromatics
voc18	esters
voc19	ethers
voc20	chlorinated
voc21	formaldehyde
voc22	other aldehydes
voc23	total ketones
voc24	total acids
voc25	other VOCs

Table A-5. The connection of emission sectors between CAMS and EDGAR v5 in estimating PMs emissions. The meanings of CAMS sectors refer to Table A-2. The linkage is based on IPCC1996 [123] sector codes reported in documentations of both emission inventories.

CAMS sector	**EDGAR v5 sector**	**Description in EDGAR v5**
ene	ENE	Power industry
res	RCO	Energy for buildings
tro	TRO_noRES+TRO_RES	Road transportation with/without resuspension
tnr	TNR_other	Railways, pipelines, off-road transport
ind	REF_TRF+IND	Oil refineries and Transformation industry, Combustion for manufacturing
shp	TNR_ship	Shipping

Table A-6. The connection of emission sectors between CAMS and EDGAR in applying EDGAR temporal profiles of emissions to CAMS emissions. The meaning of CAMS sectors refer to Table A-2. The linkage is based on IPCC1996 [123] sector codes reported in documentations of both emission inventories. The EDGAR sector nomenclature here used in the study of Crippa et al. [78] is slightly different from that used in the emission inventory EDGAR v5 as Table A-5.

CAMS sector	**EDGAR sector#**	**Description in EDGAR**
agl	ENF	Enteric fermentation
ags	AGS	Agricultural soils
awb	AWB	Agricultural waste burning
ene	ENE	Energy industry
ind	TRF^	Transformation industry
res	RCO	Residential
tnr	TNR*	Non-road transport
tro	TRO	Road transport
fef+	PRO	Fuel production/transmission
slv	SOL	Application of solvents
swd	SWD	Solid waste disposal
shp	TNR	Shipping

A full list of EDGAR sectors refers to [78].
^ ind (CAMS sector) = REF+TRF+IND+IRO+NFE+CHE+NMM+NEU+PRU+RAP+FOO (EDGAR sectors). Linking TRF to ind is because only TRF has both of diurnal and weekly profiles.
* TNR (EDGAR sector) includes railway, ship, aviation and others. 'tnr' (CAMS sector) includes railway and others.
+ fef (CAMS sector) = PRO (EDGAR sector) + FFF (EDGAR sector). Since FFF has no weekly and diurnal profiles, fef is linked to PRO.

Table A-7. Change of total emissions rate (kg/s) of NOx for four emission sources in the downscaled emissions on the entire downscaling region.

Emission source	Emission specie	Original total emission rate (kg/s)	Downscaled total emission rate (kg/s)	Variation (%)
Transportation	NOx	43.49	42.83	-1.5
Residential	NOx	10.14	10.04	-1.0
Power plant	NOx	29.64	28.89	-2.5
Industrial	NOx	64.61	62.70	-3.0

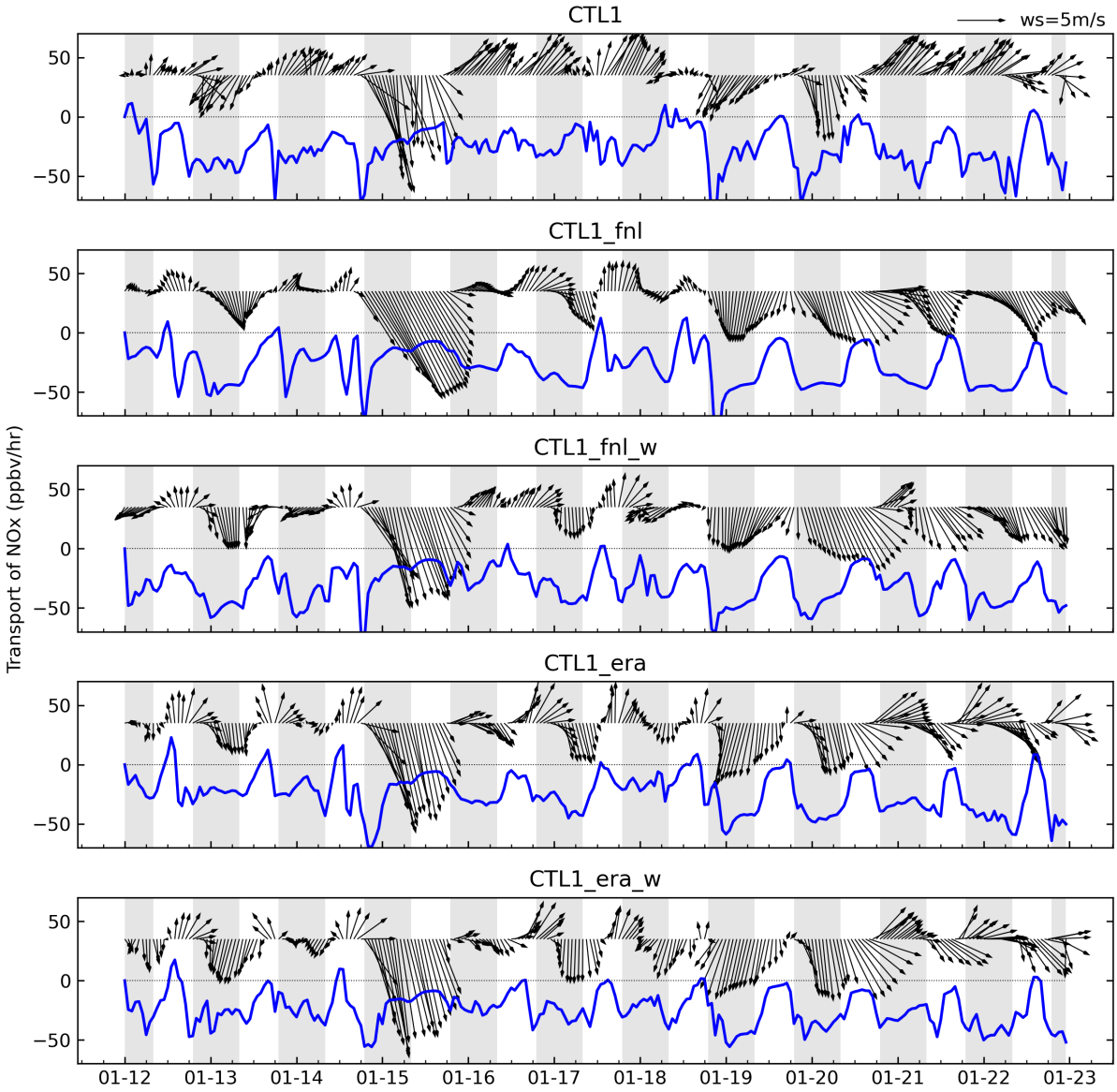

Figure A-1. Transport contribution to NOx concentration in the simulation period and the surface wind vector. Shading areas represent night-time 19:00-08:00 (LCT).

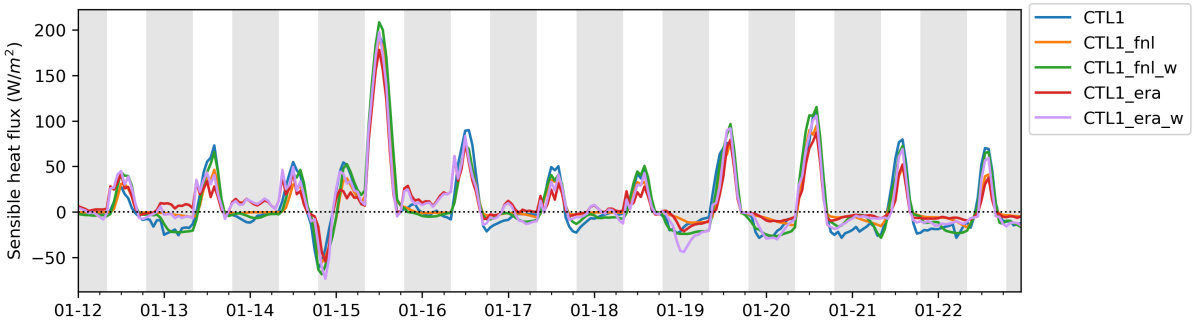

Figure A-2. Time series of sensible heat flux in Beijing in five experiment. Shading areas represent night-time 19:00-08:00 (LCT).

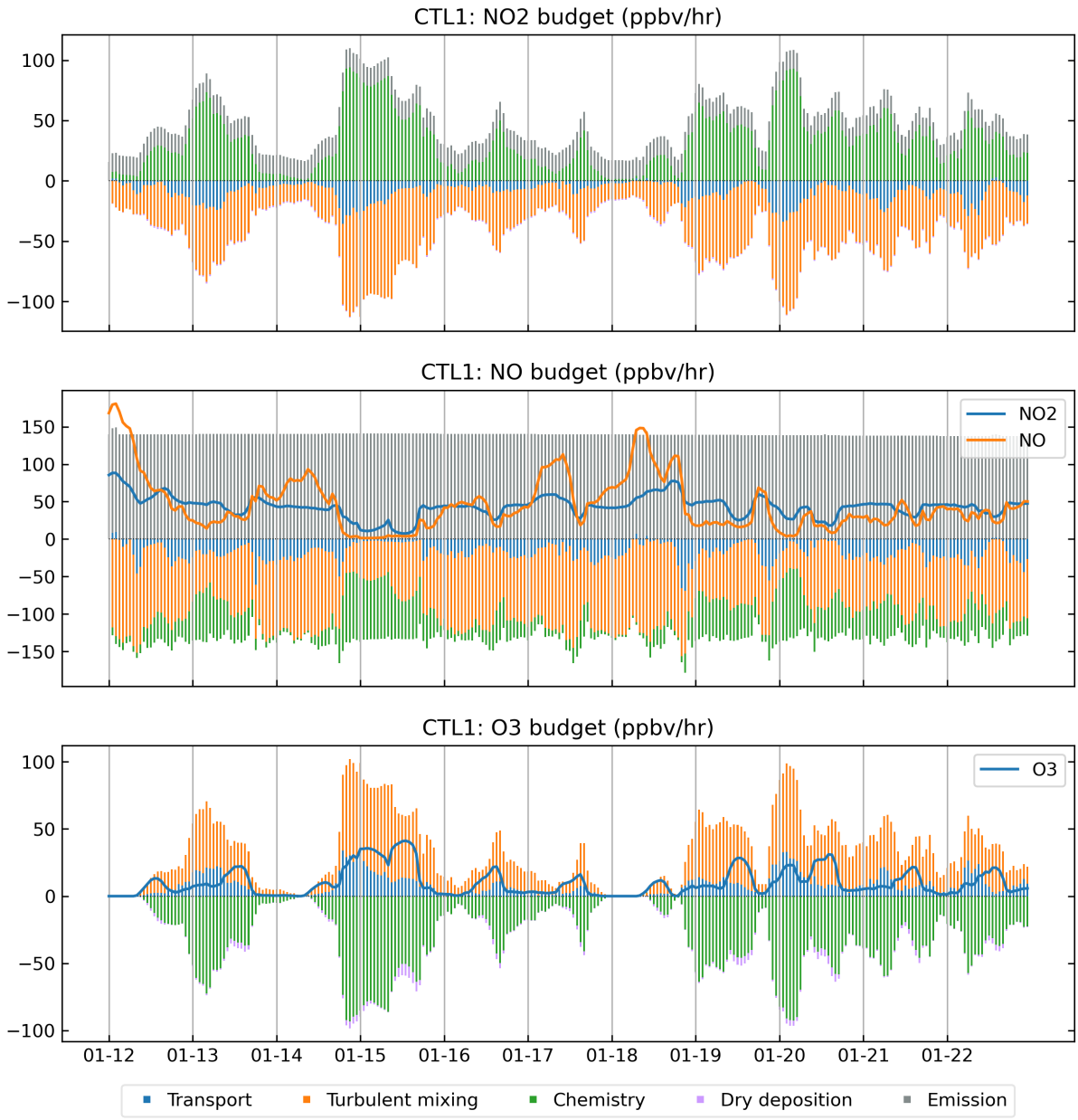

Figure A-3. Time series of budgets of NO_2, NO and ozone in simulation of CTL1.

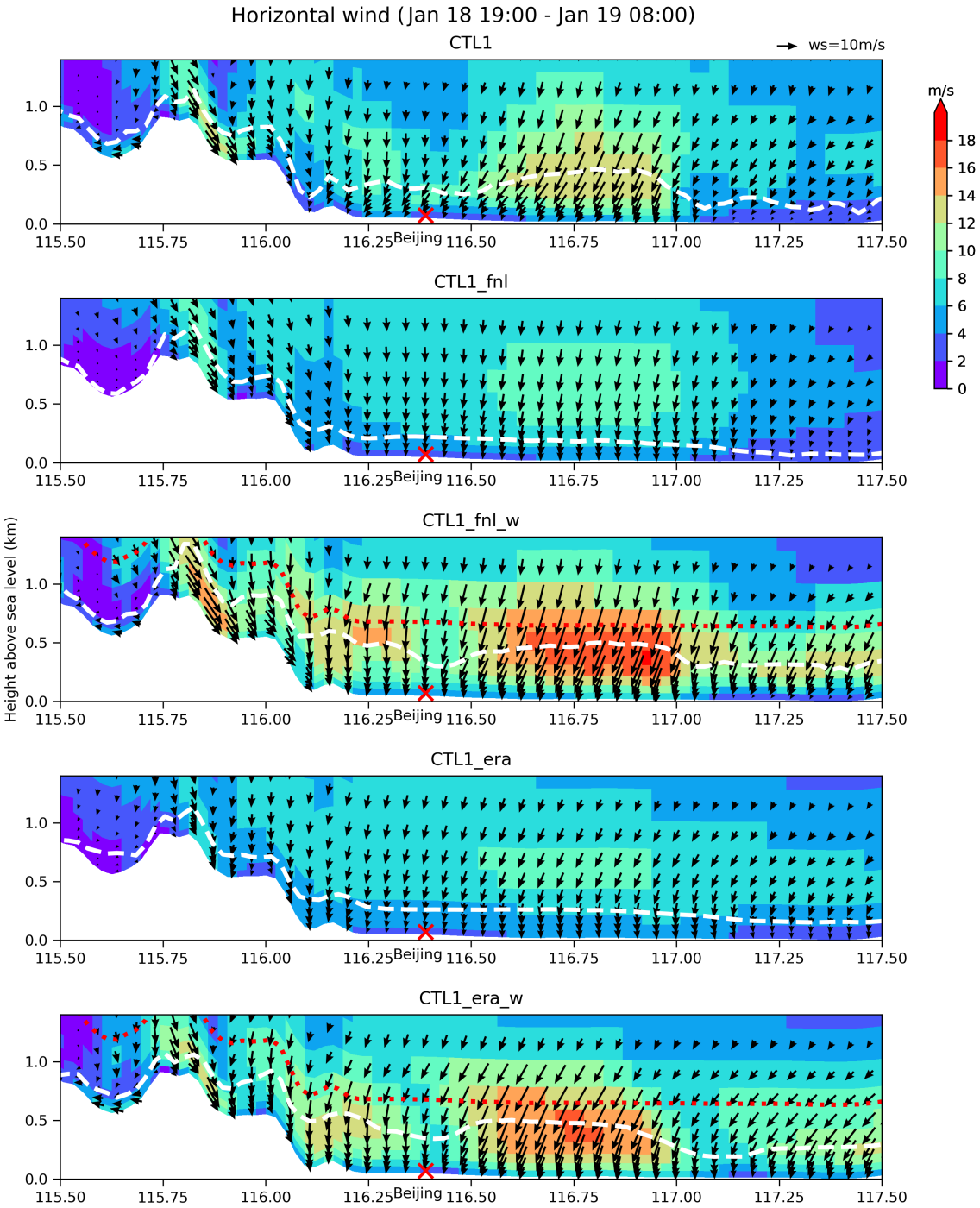

Figure A-4. Longitude-height cross section of horizontal wind speed (shading) and wind vector (black arrow) simulated in the period from 19:00, January 18 to 8:00, January 19. White dashed line is the boundary layer height. Red dotted line is the height of 600m above ground.

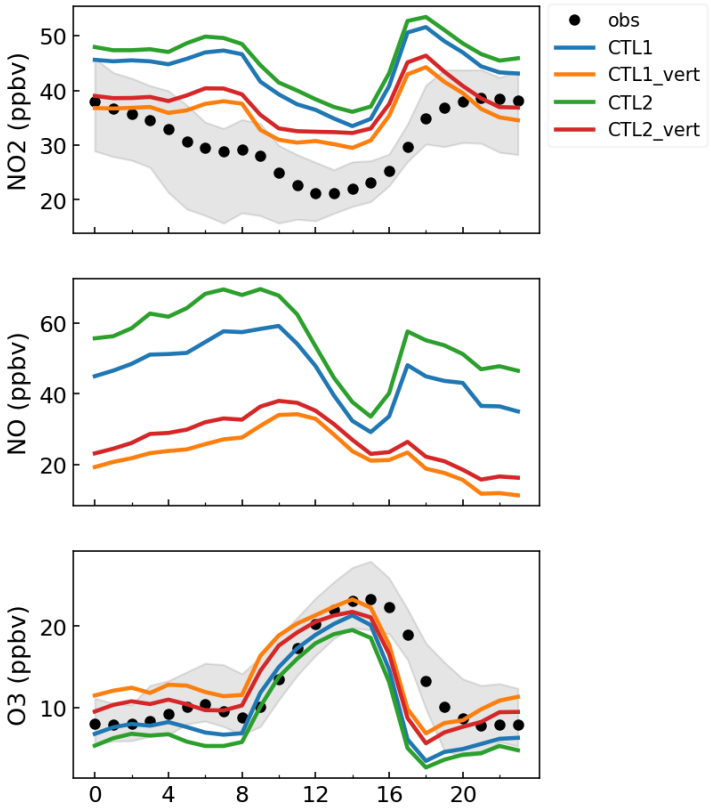

Figure A-5. Diurnal variation of NO_2, NO and ozone concentrations simulated in CTL1, CTL1_vert, CTL2 and CTL2_vert and observations of NO_2 and ozone in the city of Beijing. Shadows under black dots are the range of observation sites. Data is averaged over the period of January 12 to 22, 2019.

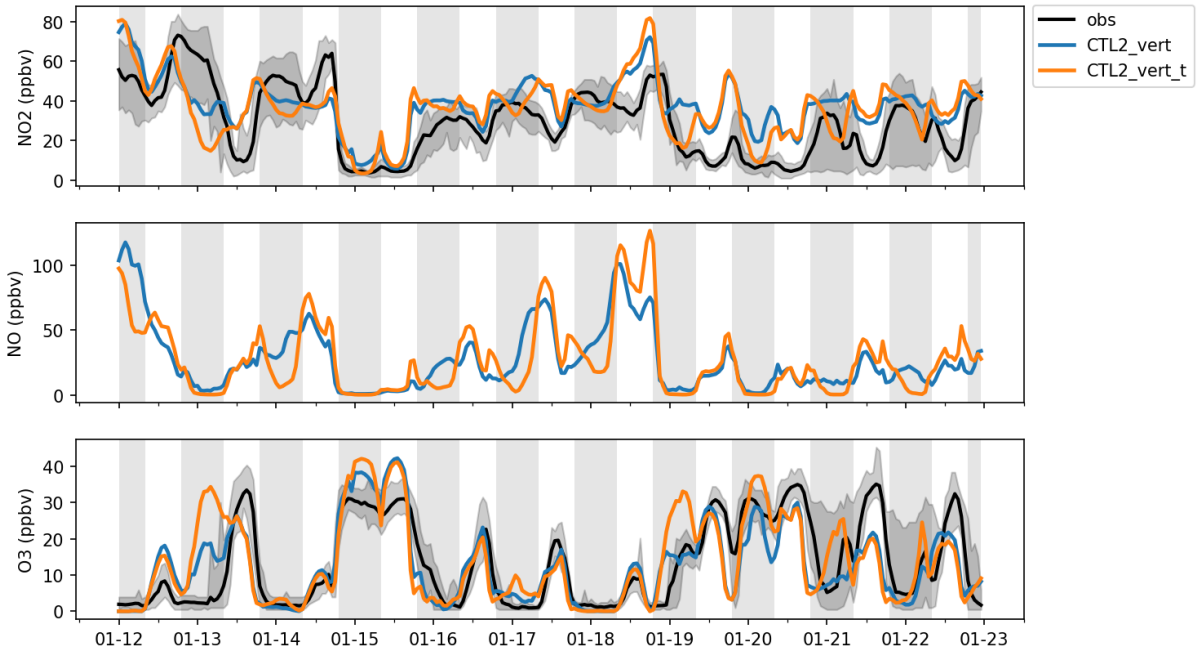

Figure A-6. Time series of NO_2, NO and ozone simulated in CTL2_vert and CTL2_vert_t in a time period of January 12 to 22, 2019. Shading areas represent night-time 19:00-08:00 (LCT).

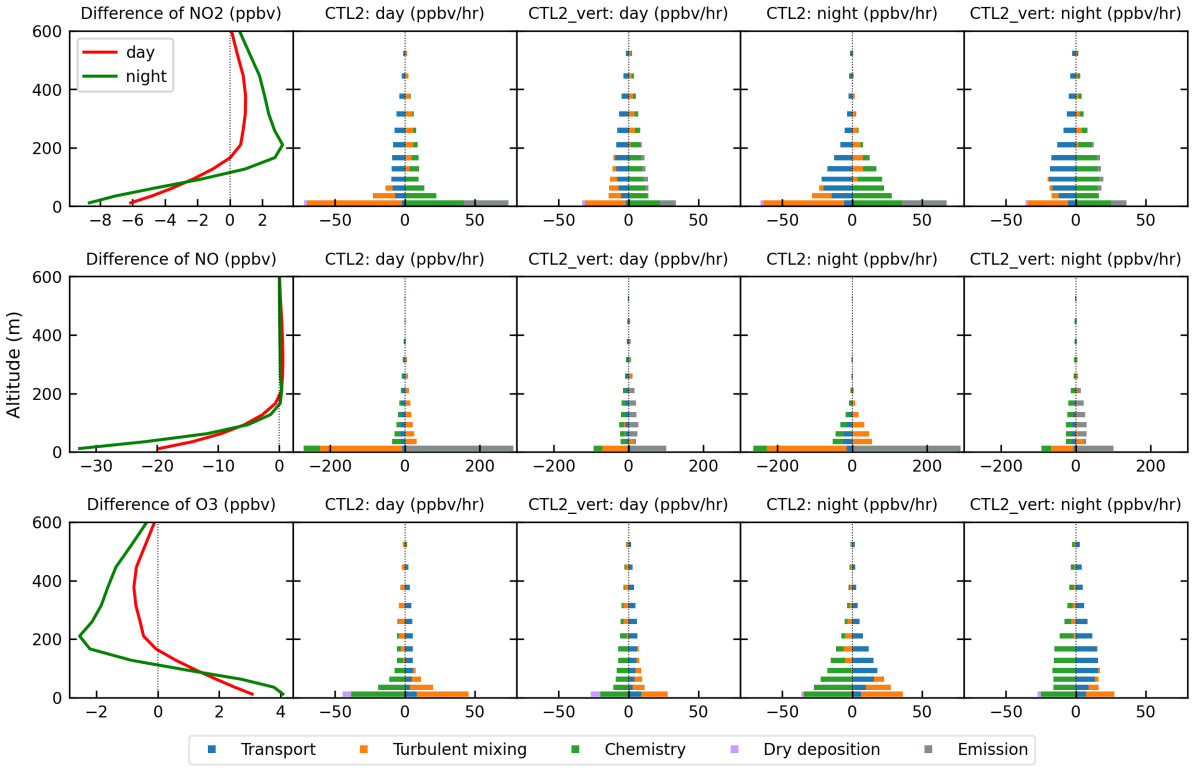

Figure A-7. Idem as Figure 4-3 but for the results in cases CTL2 and CTL2_vert.

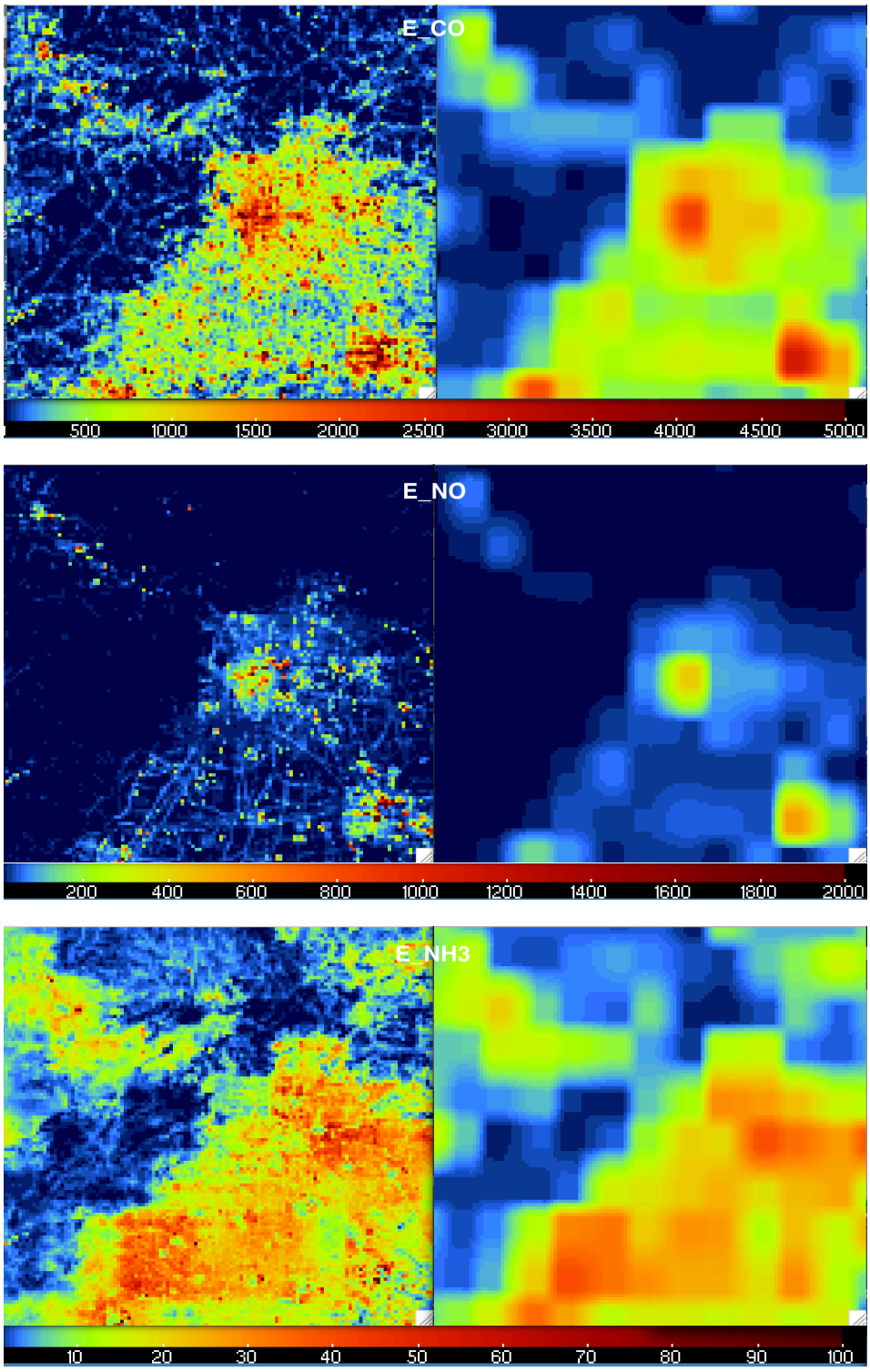

Figure A-8. Anthropogenic emission flux ($mol/(km^2 \cdot hr)$) of CO, NO and NH_3 in experiments CTL1 (right) and CTL1_dwns (left) in the Domain 3.

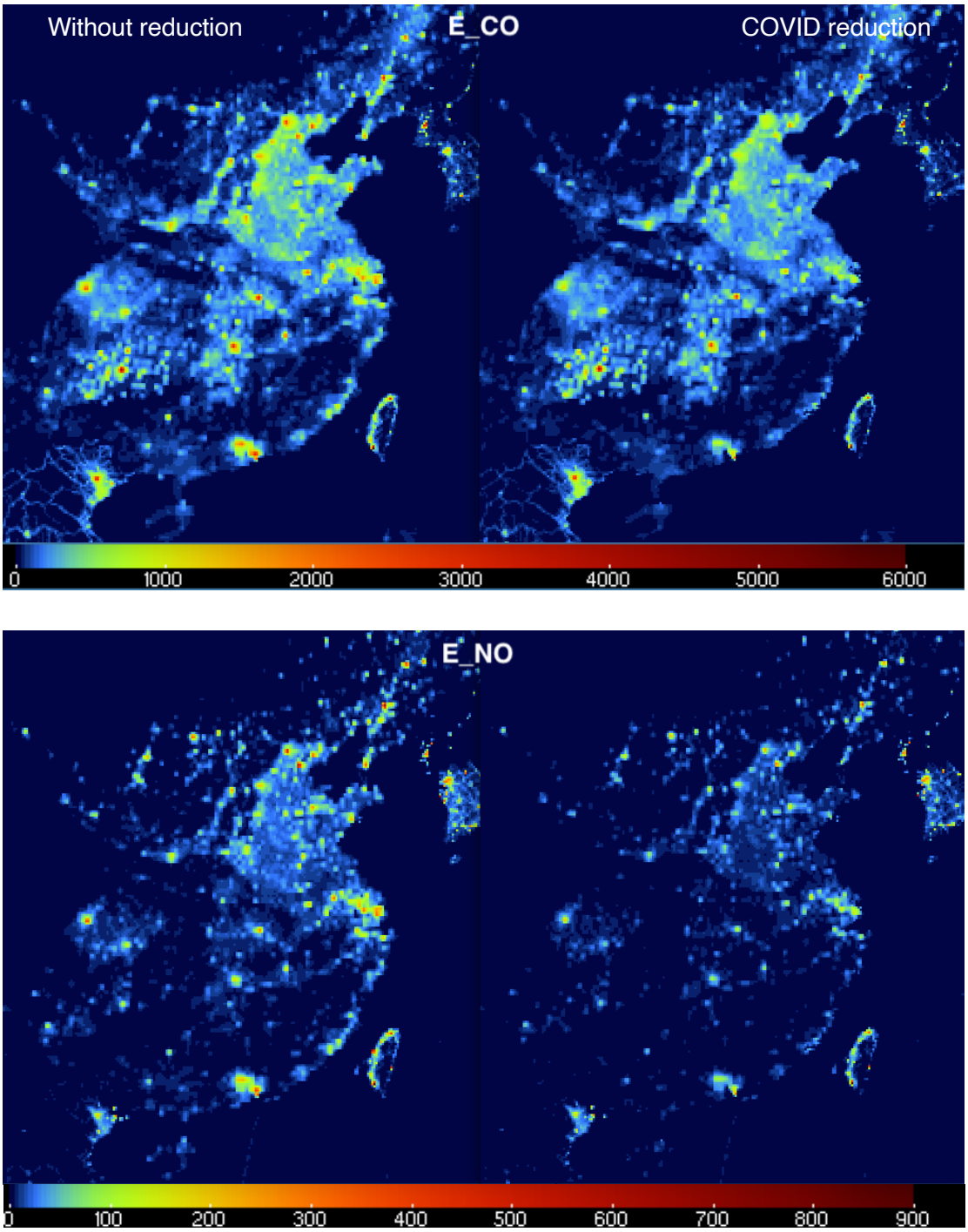

Figure A-9. Anthropogenic emission flux ($mol/(km^2 \cdot hr)$) of CO and NO in the COVID experiments. Left column is for the simulation without reduction factors and the right column with reduction factors.

References

[1] C. Jacobs and W. J. Kelly, Smogtown: the lung-burning history of pollution in Los Angeles, Abrams, 2008.

[2] G. P. Brasseur, The ozone layer: from discovery to recovery, Boston: American Meteorological Society, 2020.

[3] J. A. Salmond, "Wavelet analysis of intermittent turbulence in a very stable nocturnal boundary layer: implications for the vertical mixing of ozone," *Boundary-Layer Meteorology,* vol. 114, pp. 463-488, 2005.

[4] P. S. Kulkarni, D. Bortoli, A. M. Silva and C. E. Reeves, "Enhancements in nocturnal surface ozone at urban sites in the UK," *Environmental Science and Pollution Research,* vol. 22, pp. 20295-20305, 2015.

[5] H. Yang, C. Lu, Y. Hu, P. W. Chan, L. Li and L. Zhang, "Effects of horizontal transport and vertical mixing on nocturnal ozone pollution in the Pearl River Delta," *Atmosphere,* vol. 13, no. 8, p. 1318, 2022.

[6] J. M. Wallace and P. V. Hobbs, Atmospheric science: an introductory survey, vol. 92, Elsevier, 2006.

[7] R. B. Stull, An introduction to boundary layer meteorology, vol. 13, Springer Science & Business Media, 1988.

[8] P. Sheng, J. Mao, J. Li, Z. Ge, A. Zhang, J. Sang, N. Pan and H. Zhang, Atmospheric physics (in Chinese), Peking University Press, 2013.

[9] L. Prandtl, "Report on investigation of developed turbulence," *Zeitschrift fuer Angewandte Matematik und Mechanik,* vol. 5, no. NACA-TM-1231, 1949.

[10] A. S. Monin and A. M. Obukhov, "Basic laws of turbulent mixing in the surface layer of the atmosphere," *Contrib. Geophys. Inst. Acad. Sci. USSR,* vol. 151, no. 163, p. e187, 1954.

[11] J. A. Businger, J. C. Wyngaard, Y. Izumi and E. F. Bradley, "Flux-profile relationships in the atmospheric surface layer," *Journal of the atmospheric Sciences,* vol. 28, no. 2, pp. 181-189, 1971.

[12] A. Dyer, "A review of flux-profile relationships," *Boundary-Layer Meteorology,* vol. 7, pp. 363-372, 1974.

[13] A. J. Haagen-Smit, "Chemistry and physiology of Los Angeles smog," *Industrial & Engineering Chemistry,* vol. 44, no. 6, pp. 1342-1346, 1952.

[14] K. Westberg, N. Cohen and K. W. Wilson, "Carbon monoxide: Its role in photochemical smog formation," *Science,* vol. 171, no. 3975, pp. 1013-1015, 1971.

[15] National Research Council, "VOCs and NOx: Relationship to Ozone and Associated Pollutants.," *Rethinking the Ozone Problem in Urban and Regional Air Pollution,* pp. 163-186, 1991.

[16] Z. Liu, Y. Wang, B. Hu, K. Lu, G. Tang, D. Ji, X. Yang, W. Gao, Y. Xie, J. . Liu and Y. Zhang, "Elucidating the quantitative characterization of atmospheric oxidation capacity in Beijing, China," *Science of the Total Environment,* vol. 771, p. 145306, 2021.

[17] B. J. Finlayson-Pitts and J. N. Pitts Jr, Chemistry of the upper and lower atmosphere: theory, experiments, and applications, Elsevier, 1999.

[18] G. P. Brasseur and D. J. Jacob, Modeling of atmospheric chemistry, Cambridge University Press, 2017.

[19] F. Chen, X. Yang and J. Wu, "Simulation of the urban climate in a Chinese megacity with spatially heterogeneous anthropogenic heat data," *Journal of Geophysical Research: Atmospheres,* vol. 121, no. 10, pp. 5193-5212, 2016.

[20] Y. L. Zhang and F. Cao, "Fine particulate matter (PM2. 5) in China at a city level," *Scientific reports,* vol. 5, no. 1, pp. 1-12, 2015.

[21] National Development and Reform Commission of China; National Energy Administration of China; Ministry of Finance of the People's Republic of China, "The plan of clean winter heating in northern China (2017-2021) (in Chinese)," 5 12 2017. [Online]. Available: http://www.gov.cn/xinwen/2017-12/20/content_5248855.htm. [Accessed 3 10 2023].

[22] Z. Zong, Y. Tan, X. Wang, C. Tian, J. Li, Y. Fang, Y. Chen, S. Cui and G. Zhang, "Dual-modelling-based source apportionment of NOx in five Chinese megacities: Providing the isotopic footprint from 2013 to 2014," *Environment international,* vol. 137, p. 105592, 2020.

[23] W. Wang, R. van der A, J. Ding, M. van Weele and T. Cheng, "Spatial and temporal changes of the ozone sensitivity in China based on satellite and ground-based observations," *Atmospheric Chemistry and Physics,* vol. 21, no. 9, pp. 7253-7269, 2021.

[24] J. Mao, F. Paulot, D. J. Jacob, R. C. Cohen, J. D. Crounse, P. O. Wennberg, C. Keller, R. Hudman, M. Barkley and L. W. Horowitz, "Ozone and organic nitrates over the eastern United States: Sensitivity to isoprene chemistry," vol. 118, no. 19, pp. 11-256, 2013.

[25] L. I. Kleinman, "Seasonal dependence of boundary layer peroxide concentration: The low and high NO x regimes.," *Journal of Geophysical Research: Atmospheres,* vol. 96, no. D11, pp. 20721-20733, 1991.

[26] X. M. Hu, P. M. Klein, M. Xue, F. Zhang, D. C. Doughty, R. Forkel, E. Joseph and J. D. Fuentes, "Impact of the vertical mixing induced by low-level jets on boundary layer ozone concentration," *Atmospheric Environment,* vol. 70, pp. 123-130, 2013.

[27] J. A. Salmond and I. G. McKendry, "A review of turbulence in the very stable nocturnal boundary layer and its implications for air quality," *Progress in Physical Geography,* vol. 29, no. 2, pp. 171-188, 2005.

[28] Y. Zhou, S. Cheng, D. Chen, J. Lang, G. Wang, T. Xu, X. Wang and S. Yao, "Temporal and spatial characteristics of ambient air quality in Beijing, China," *Aerosol and Air Quality Research,* vol. 15, no. 5, pp. 1868-1880, 2015.

[29] G. Zhang, L. Xia, K. Zang, W. Xu, F. Zhang, L. Liang, B. Yao, W. Lin and Y. Mu, "The abundance and inter-relationship of atmospheric peroxyacetyl nitrate (PAN), peroxypropionyl nitrate (PPN), O3, and NOy during the wintertime in Beijing, China," *Science of the Total Environment,* vol. 718, p. 137388, 2020.

[30] C. He, X. Lu, H. Wang, H. Wang, Y. Li, G. He, Y. Wang, Y. Zhang, Y. Liu and S. Fan, "The unexpected high frequency of nocturnal surface ozone enhancement events over China: characteristics and mechanisms," *Atmospheric Chemistry and Physics,* vol. 22, no. 23, pp. 15243-15261, 2022.

[31] W. Kuang, Z. Li and R. Hamdi, "Comparison of surface radiation and turbulent heat fluxes in Olympic Forest Park and on a building roof in Beijing, China," *Urban Climate,* vol. 31, p. 100562, 2020.

[32] H. Fan and D. J. Sailor, "Modeling the impacts of anthropogenic heating on the urban climate of Philadelphia: a comparison of implementations in two PBL schemes," *Atmospheric environment,* vol. 39, no. 1, pp. 73-84, 2005.

[33] T. R. Oke, G. Mills, A. Christen and J. A. Voogt, Urban climates, Cambridge University Press, 2017, p. 233.

[34] T. R. Oke, "The heat island of the urban boundary layer: characteristics, causes and effects," in *Wind climate in cities*, Springer Science & Business Media, 1995, pp. 81-107.

[35] T. Stocker, "Climate change 2013: the physical science basis: Working Group I contribution to the Fifth assessment report of the Intergovernmental Panel on Climate Change," Cambridge university press, 2014.

[36] K. Mariano, "COVID-19 cancels more than 200,000 flights to, from and within China," 28 2 2020. [Online]. Available: https://www.traveldailymedia.com/covid-19-cancels-more-than-200000-flights-to-from-and-within-china. [Accessed 3 10 2023].

[37] R. Zhang, Y. Zhang, H. Lin, X. Feng, T. M. Fu and Y. Wang, "NOx emission reduction and recovery during COVID-19 in East China," *Atmosphere,* vol. 11, no. 4, p. 433, 2020.

[38] B. Zheng, Q. Zhang, G. Geng, C. Chen, Q. Shi, M. Cui, Y. Lei and K. He, "Changes in China's anthropogenic emissions and air quality during the COVID-19 pandemic in 2020," *Earth System Science Data,* vol. 13, no. 6, pp. 2895-2907, 2021.

[39] X. Shi and G. P. Brasseur, "The response in air quality to the reduction of Chinese economic activities during the COVID-19 outbreak," *Geophysical Research Letters,* vol. 47, no. 11, p. e2020GL088070, 2020.

[40] P. Si, M. Wang, M. Li, Y. Wang, Y. Guo, Y. Yang and J. Wang, "The observed features and some possible reasons of annual temperature extremes over Beijing-Tianjin-Hebei region for a century long-term based on newly constructed daily observations," *International Journal of Climatology,* vol. 43, no. 9, pp. 4248-4268, 2023.

[41] Z. Shi, G. Jia, Y. Hu and Y. Zhou, "The contribution of intensified urbanization effects on surface warming trends in China," *Theoretical and Applied Climatology,* vol. 138, pp. 1125-1137, 2019.

[42] P. Yang, G. Ren, P. Yan and J. Deng, "Urbanization reduces frequency of light rain: an example from Beijing City," *Theoretical and Applied Climatology,* vol. 145, no. 1-2, pp. 763-774, 2021.

[43] Y. Yuan, P. Zhai, Y. Chen and J. Li, "Hourly extreme precipitation changes under the influences of regional and urbanization effects in Beijing," *International Journal of Climatology,* vol. 41, no. 2, pp. 1179-1189, 2021.

[44] K. Qin, L. Wang, J. Xu, H. Letu, K. Zhang, D. Li, J. Zou and W. Fan, "Haze optical properties from long-term ground-based remote sensing over Beijing and Xuzhou, China," *Remote Sensing,* vol. 10, no. 4, p. 518, 2018.

[45] X. Hu, X. Cai, X. Wang, Y. Song, X. Wang, L. Kang and H. Zhang, "Surface wind climates in the North China Plain: Implications for air quality," *International Journal of Climatology,* vol. 42, no. 16, pp. 10322-10336, 2022.

[46] N. Cheng, Y. Li, B. Cheng, X. Wang, F. Meng, Q. Wang and Q. Qiu, "Comparisons of two serious air pollution episodes in winter and summer in Beijing," *Journal of Environmental sciences,* vol. 69, pp. 141-154, 2018.

[47] L. Wang, F. Zhang, E. Pilot, J. Yu, C. Nie, J. Holdaway, L. Yang, Y. Li, W. Wang, S. Vardoulakis and T. Krafft, "Taking action on air pollution control in the Beijing-Tianjin-Hebei (BTH) region: progress, challenges and opportunities," *International journal of environmental research and public health,* vol. 15, no. 2, p. 306, 2018.

[48] J. Lang, Y. Zhang, Y. Zhou, S. Cheng, D. Chen, X. Guo, S. Chen, X. Li, X. Xing and H. Wang, "Trends of PM2. 5 and chemical composition in Beijing, 2000-2015.," *Aerosol and Air Quality Research,* vol. 17, no. 2, pp. 412-425, 2017.

[49] Z. Wen, C. Wang, Q. Li, W. Xu, L. Lu, X. Li, A. Tang, J. Collett Jr and X. Liu, "Winter air quality improvement in Beijing by clean air actions from 2014 to 2018," *Atmospheric Research,* vol. 259, p. 105674, 2021.

[50] J. Hong, W. Wang, Z. Bai, J. Bian, M. Tao, P. Konopka, F. .Ploeger, R. Müller, H. Wang, J. Zhang, S. Zhao and J. Zhu, "The Long-Term Trends and Interannual Variability in Surface Ozone Levels in Beijing from 1995 to 2020," *Remote sensing,* vol. 14, no. 22, p. 5726, 2022.

[51] W. Wang, D. D. Parrish, S. Wang, F. Bao, R. Ni, X. Li, S. Yang, H. Wang, Y. Cheng and H. Su, "Long-term trend of ozone pollution in China during 2014–2020: Distinct seasonal and spatial characteristics and ozone sensitivity," *Atmospheric Chemistry and Physics,* vol. 22, no. 13, pp. 8935-8949, 2022.

[52] A. Soulie, C. Granier, S. Darras, N. Zilbermann, T. Doumbia, M. Guevara, J. Jalkanen, S. Keita, C. Liousse, M. Crippa, D. Guizzardi, R. Hoesly and S. Smith, "Global Anthropogenic Emissions (CAMS-GLOB-ANT) for the Copernicus Atmosphere Monitoring Service Simulations of Air Quality Forecasts and Reanalyses," *Earth System Science Data Discussions,* vol. 2023, pp. 1-45, 2019.

[53] F. Huang, W. Zhan, J. Voogt, L. Hu, Z. Wang, J. Quan, W. Ju and Z. Guo, "Temporal upscaling of surface urban heat island by incorporating an annual

temperature cycle model: A tale of two cities," *Remote Sensing of Environment,* vol. 186, pp. 1-12, 2016.

[54] M. Biggart, J. Stocker, R. M. Doherty, O. Wild, D. Carruthers, S. Grimmond, Y. Han, P. Fu and S. Kotthaus, "Modelling spatiotemporal variations of the canopy layer urban heat island in Beijing at the neighbourhood scale," *Atmospheric Chemistry and Physics,* vol. 21, no. 17, pp. 13687-13711, 2021.

[55] R. Sun, Y. Wang and L. Chen, "A distributed model for quantifying temporal-spatial patterns of anthropogenic heat based on energy consumption," *Journal of Cleaner Production,* vol. 170, pp. 601-609, 2018.

[56] J. G. Powers, J. B. Klemp, W. C. Skamarock, C. A. Davis, J. Dudhia, D. O. Gill, J. Coen, D. Gochis, R. Ahmadov, S. Peckham, G. Grell, M. J., T. S., B. S. G., A. C. R., D. G. J., Wang W., S. C. S., R. G. S., L. Z., S. C., C. F., B. M. J., Y. W. and M. G. Duda, "The weather research and forecasting model: Overview, system efforts, and future directions," *Bulletin of the American Meteorological Society,* vol. 98, no. 8, pp. 1717-1737, 2017.

[57] S. Peckham, R. Schmitz, S. McKeen, G. Frost, W. Skamarock and B. Eder, "Fully coupled 'online' chemistry in the WRF model," *Atmos. Environ.,* vol. 39, pp. 6957-6976, 2005.

[58] J. Fast, W. Gustafson Jr, R. Easter, R. Zaveri, J. Barnard, E. Chapman, G. Grell and S. Peckham, "Evolution of ozone, particulates, and aerosol direct forcing in an urban area using a new fully-coupled meteorology, chemistry, and aerosol model," *J. Geophys. Res,,* vol. 111, no. 5, p. D21305, 2006.

[59] National Centers for Environmental Prediction/National Weather Service/NOAA/U.S. Department of Commerce, "NCEP FNL Operational Model Global Tropospheric Analyses," Research Data Archive at the National Center for Atmospheric Research, Computational and Information Systems Laboratory, Boulder, Colo., 2000. [Online]. Available: https://doi.org/10.5065/D6M043C6. [Accessed 11 3 2022].

[60] H. Hersbach, B. Bell, P. Berrisford, S. Hirahara, A. Horányi, J. Muñoz-Sabater, J. Nicolas, C. Peubey, R. Radu, D. Schepers and A. Simmons, "The ERA5 global reanalysis," *Quarterly Journal of the Royal Meteorological Society,* vol. 146, no. 730, pp. 1999-2049, 2020.

[61] R. R. Buchholz, L. K. Emmons, S. Tilmes and C. D. T. The, "CESM2.1/CAM-chem Instantaneous Output for Boundary Conditions," UCAR/NCAR - Atmospheric Chemistry Observations and Modeling Laboratory., 28 1 2021. [Online]. Available: https://doi.org/10.5065/NMP7-EP60.

[62] D. R. Stauffer and N. L. Seaman, "Use of four-dimensional data assimilation in a limited-area mesoscale model. Part I: Experiments with synoptic-scale data," *Monthly Weather Review,* vol. 118, no. 6, pp. 1250-1277, 1990.

[63] G. Thompson, P. R. Field, R. M. Rasmussen and W. D. Hall, "Explicit forecasts of winter precipitation using an improved bulk microphysics scheme. Part II: Implementation of a new snow parameterization," *Monthly Weather Review,* vol. 136, no. 12, pp. 5095-5115, 2008.

[64] G. A. Grell, "Prognostic evaluation of assumptions used by cumulus parameterizations," *Monthly weather review,* vol. 121, no. 3, pp. 764-787, 1993.

[65] G. A. Grell and D. Dévényi, "A generalized approach to parameterizing convection combining ensemble and data assimilation techniques," *Geophysical Research Letters,* vol. 29, no. 14, pp. 38-1, 2002.

[66] M. J. Iacono, J. S. Delamere, E. J. Mlawer, M. W. Shephard, S. A. Clough and W. D. Collins, "Radiative forcing by long-lived greenhouse gases: Calculations with the AER radiative transfer models," *Journal of Geophysical Research: Atmospheres,* vol. 113, no. D13, 2008.

[67] S. Y. Hong, Y. Noh and J. Dudhia, "A new vertical diffusion package with an explicit treatment of entrainment processes," *Monthly weather review,* vol. 134, no. 9, pp. 2318-2341, 2006.

[68] K. Mitchell, E. K. Mike, W. Vince, L. Dag and R. Paul, *The Community. Noah Land-Surface Model (LSM). User's Guide. Public Release Version 2.7. 1.,* vol. 26, NCEP/EMC Doc, 2005.

[69] P. A. Jiménez, J. Dudhia, J. F. González-Rouco, J. Navarro, J. P. Montávez and E. García-Bustamante, "A revised scheme for the WRF surface layer formulation," *Monthly weather review,* vol. 140, no. 3, pp. 898-918, 2012.

[70] C. Knote, A. Hodzic, J. Jimenez, R. Volkamer, J. Orlando, S. Baidar, J. Brioude, J. Fast, D. Gentner, A. Goldstein and P. Hayes, "Simulation of semi-explicit mechanisms of SOA formation from glyoxal in aerosol in a 3-D model," *Atmospheric Chemistry and Physics,* vol. 14, no. 12, pp. 6213-6239, 2014.

[71] M. Chin, P. Ginoux, S. Kinne, O. Torres, B. Holben, B. Duncan, R. Martin, J. Logan, A. Higurashi and T. Nakajima, "Tropospheric aerosol optical thickness from the GOCART model and comparisons with satellite and Sun photometer measurements," *Journal of the atmospheric sciences,* vol. 59, no. 3, pp. 461-483, 2002.

[72] S. Madronich, "The Atmosphere and UV-B Radiation at Ground Level," in *Environmental UV Photobiology*, Boston, MA: Springer, 1993, pp. 1-39.

[73] B. Zheng, D. Tong, M. Li, F. Liu, C. Hong, G. Geng, H. Li, X. Li, L. Peng, J. Qi and L. Yan, "Trends in China's anthropogenic emissions since 2010 as the consequence of clean air actions," *Atmospheric Chemistry and Physics,* vol. 18, no. 19, pp. 14095-14111, 2018.

[74] G. Zhou, J. Xu, Y. Xie, L. Chang, W. Gao, Y. Gu and J. Zhou, "Numerical air quality forecasting over eastern China: An operational application of WRF-Chem," *Atmospheric Environment,* vol. 153, pp. 94-108, 2017.

[75] X. Ma, T. Sha, J. Wang, H. Jia and R. Tian, "Investigating impact of emission inventories on PM2. 5 simulations over North China Plain by WRF-Chem," *Atmospheric Environment,* vol. 195, pp. 125-140, 2018.

[76] M. Schaap, H. Van Der Gon, F. Dentener, A. Visschedijk, M. Van Loon, H. Ten Brink, J. Putaud, B. Guillaume, C. Liousse and P. Builtjes, "Anthropogenic black carbon and fine aerosol distribution over Europe," *Journal of Geophysical Research: Atmospheres,* vol. 109, no. D18, 2004.

[77] M. Crippa, G. Oreggioni, D. Guizzardi, M. Muntean, E. Schaaf, E. Lo Vullo, E. Solazzo, F. Monforti-Ferrario, J. Olivier and E. Vignati, "Fossil CO2 and GHG emissions of all world countries," Publication Office of the European Union, Luxemburg, 2019.

[78] M. Crippa, E. Solazzo, G. Huang, D. Guizzardi, E. Koffi, M. Muntean, C. Schieberle, R. Friedrich and G. Janssens-Maenhout, "High resolution temporal profiles in the Emissions Database for Global Atmospheric Research," *Scientific data,* vol. 7, no. 1, p. 121, 2020.

[79] M. Pesaresi, A. Florczyk, M. Schiavina, M. Melchiorri and L. Maffenini, "GHS-SMOD R2019A-GHS settlement layers, updated and refined REGIO model 2014 in application to GHS-BUILT R2018A and GHS-POP R2019A, multitemporal (1975-1990-2000-2015)," European Commission, Joint Research Centre (JRC), 2019.

[80] M. Crippa, D. Guizzardi, M. Muntean, E. Schaaf, F. Dentener, J. A. van Aardenne, S. Monni, U. Doering, J. G. J. Olivier, V. Pagliari and G. Janssens-Maenhout, "Gridded emissions of air pollutants for the period 1970–2012 within EDGAR v4.3.2," *Earth Syst. Sci. Data,* vol. 10, p. 1987–2013, 2018.

[81] C. Wiedinmyer and L. Emmons., "Fire Inventory from NCAR version 2 Fire Emission. Research Data Archive at the National Center for Atmospheric Research," Computational and Information Systems Laboratory, 2022. [Online]. Available: https://doi.org/10.5065/XNPA-AF09. [Accessed 3 10 2023].

[82] G. Grell, S. R. Freitas, M. Stuefer and J. Fast, "Inclusion of biomass burning in WRF-Chem: impact of wildfires on weather forecasts," *Atmospheric Chemistry and Physics,* vol. 11, no. 11, pp. 5289-5303, 2011.

[83] A. Guenther, T. Karl, P. Harley, C. Wiedinmyer, P. I. Palmer and C. Geron, "Estimates of global terrestrial isoprene emissions using MEGAN (Model of Emissions of Gases and Aerosols from Nature)," *Atmospheric Chemistry and Physics,* vol. 6, no. 11, pp. 3181-3210, 2006.

[84] W. Wei, H. Zhang, X. Cai, Y. Song, Y. Bian, K. Xiao and H. Zhang, "Influence of intermittent turbulence on air pollution and its dispersion in winter 2016/2017 over Beijing, China," *Journal of Meteorological Research,* vol. 34, no. 1, pp. 176-188, 2020.

[85] H. Tao, J. Xing, G. Pan, J. Pleim, L. Ran, S. Wang, X. Chang, G. Li, F. Chen and J. Li, "Impact of anthropogenic heat emissions on meteorological parameters and air quality in Beijing using a high-resolution model simulation," *Frontiers of Environmental Science & Engineering,* vol. 16, pp. 1-11, 2022.

[86] Y. Shi, F. Hu, G. Fan and Z. Zhang, "Multiple technical observations of the atmospheric boundary layer structure of a red-alert haze episode in Beijing," *Atmospheric Measurement Techniques,* vol. 12, no. 9, pp. 4887-4901, 2019.

[87] S. Kotthaus and C. S. B. Grimmond, "Energy exchange in a dense urban environment–Part I: Temporal variability of long-term observations in central London," *Urban Climate,* vol. 10, pp. 261-280, 2014.

[88] X. Liu, W. Yue, Y. Zhou, Y. Liu, C. Xiong and Q. Li, "Estimating multi-temporal anthropogenic heat flux based on the top-down method and temporal

downscaling methods in Beijing, China," *Resources, Conservation and Recycling,* vol. 172, p. 105682, 2021.

[89] S. Y. Hong, "A new stable boundary-layer mixing scheme and its impact on the simulated East Asian summer monsoon," *Quarterly Journal of the Royal Meteorological Society,* vol. 136, no. 651, pp. 1481-1496, 2010.

[90] M. Guevara, C. Tena, M. Porquet, O. Jorba and C. Pérez García-Pando, "HERMESv3, a stand-alone multi-scale atmospheric emission modelling framework–Part 2: The bottom–up module," *Geoscientific Model Development,* vol. 13, no. 3, pp. 873-903, 2020.

[91] J. Bieser, A. Aulinger, V. Matthias, M. Quante and H. D. Van Der Gon, "Vertical emission profiles for Europe based on plume rise calculations," *Environmental Pollution,* vol. 159, no. 10, pp. 2935-2946, 2011.

[92] M. Guevara, A. Soret, G. Arévalo, F. Martínez and J. M. Baldasano, "Implementation of plume rise and its impacts on emissions and air quality modelling," *Atmospheric environment,* vol. 99, pp. 618-629, 2014.

[93] M. Guevara, O. Jorba, C. Tena, H. Denier van der Gon, J. Kuenen, N. Elguindi, S. Darras, C. Granier and C. Pérez García-Pando, "Copernicus Atmosphere Monitoring Service TEMPOral profiles (CAMS-TEMPO): global and European emission temporal profile maps for atmospheric chemistry modelling," *Earth System Science Data,* vol. 13, no. 2, pp. 367-404, 2021.

[94] A. Mues, J. Kuenen, C. Hendriks, A. Manders, A. Segers, Y. Scholz, C. Hueglin, P. Builtjes and M. Schaap, "Sensitivity of air pollution simulations with LOTOS-EUROS to the temporal distribution of anthropogenic emissions," *Atmospheric Chemistry and Physics,* vol. 14, no. 2, pp. 939-955, 2014.

[95] J. Zheng, L. Zhang, W. Che, Z. Zheng and S. Yin, "A highly resolved temporal and spatial air pollutant emission inventory for the Pearl River Delta region, China and its uncertainty assessment," *Atmospheric Environment,* vol. 43, no. 32, pp. 5112-5122, 2009.

[96] L. Menut, A. Goussebaile, B. Bessagnet, D. Khvorostiyanov and A. Ung, "Impact of realistic hourly emissions profiles on air pollutants concentrations modelled with CHIMERE," *Atmospheric environment,* vol. 49, pp. 233-244, 2012.

[97] T. Doumbia, C. Granier, N. Elguindi, I. Bouarar, S. Darras, G. Brasseur, B. Gaubert, Y. Liu, X. Shi, T. Stavrakou, S. Tilmes, L. F., D. A. and T. Wang, "Changes in global air pollutant emissions during the COVID-19 pandemic: a dataset for atmospheric chemistry modeling," *Earth System Science Data Discussions,* pp. 1-26, 2021.

[98] T. Le, Y. Wang, L. Liu, J. Yang, Y. L. Yung, G. Li and J. H. Seinfeld, "Unexpected air pollution with marked emission reductions during the COVID-19 outbreak in China," *Science,* vol. 369, no. 6504, pp. 702-706, 2020.

[99] T. Stavrakou, J. Müller, M. Bauwens, T. Doumbia, N. Elguindi, S. Darras, C. Granier, I. Smedt, C. Lerot, M. Van Roozendael and B. Franco, "Atmospheric impacts of COVID-19 on NOx and VOC levels over China based on TROPOMI and IASI satellite data and modeling," *Atmosphere,* vol. 12, no. 8, p. 946, 2021.

[100] Y. Liu, T. Wang, T. Stavrakou, N. Elguindi, T. Doumbia, C. Granier, I. Bouarar, B. Gaubert and G. Brasseur, "Diverse response of surface ozone to COVID-19 lockdown in China," *Science of the Total Environment,* vol. 789, p. 147739, 2021.

[101] B. Gaubert, I. Bouarar, T. Doumbia, Y. S. T. Liu, A. Deroubaix, S. Darras, N. G. C. Elguindi, F. Lacey and J. Müller, "Global changes in secondary atmospheric pollutants during the 2020 COVID-19 pandemic," *Journal of Geophysical Research: Atmospheres,* vol. 126, no. 8, p. e2020JD034213, 2021.

[102] S. Mailler, D. Khvorostyanov and L. Menut, "Impact of the vertical emission profiles on background gas-phase pollution simulated from the EMEP emissions over Europe," *Atmospheric Chemistry and Physics,* vol. 13, no. 12, pp. 5987-5998, 2013.

[103] M. Buchhorn, B. Smets, L. Bertels, B. De Roo, M. Lesiv, N. Tsendbazar, M. Herold and S. Fritz, "Copernicus Global Land Service: Land Cover 100m: collection 3: epoch 2019: Globe," 2020. [Online]. Available: https://doi.org/10.5281/zenodo.3939050. [Accessed 3 10 2023].

[104] A. Rose, J. McKee, K. Sims, E. Bright, A. Reith and M. Urban, "LandScan Global 2019," Oak Ridge National Laboratory, 2020. [Online]. Available: https://doi.org/10.48690/1524214. [Accessed 3 10 2023].

[105] OpenStreetMap contributors, "Planet dump retrieved from https://planet.osm.org," 2017. [Online]. Available: https://www.openstreetmap.org. [Accessed 3 10 2023].

[106] L. Tang, X. Xue, J. Qu, Z. Mi, X. Bo, X. Chang, S. Wang, S. Li, W. Cui and G. Dong, "Air pollution emissions from Chinese power plants based on the continuous emission monitoring systems network," *Scientific Data,* vol. 7, no. 1, p. 325, 2020.

[107] X. Xu, J. Liu, S. Zhang, R. Li, C. Yan and S. Wu, "China Multi-period Land Use Land Cover Remote Sensing Monitoring Data Set," China Resource and Environment Science and Data Centre, 2020. [Online]. Available: https://www.resdc.cn/DOI/doi.aspx?DOIid=54. [Accessed 3 10 2023].

[108] M. Biggart, J. Stocker, R. Doherty, O. Wild, M. Hollaway, D. Carruthers, J. Li, Q. Zhang, R. Wu, S. Kotthaus and S. Grimmond, "Street-scale air quality modelling for Beijing during a winter 2016 measurement campaign," *Atmospheric Chemistry and Physics,* vol. 20, no. 5, pp. 2755-2780, 2020.

[109] D. Yao, G. Tang, Y. Wang, Y. Yang, Y. Wang, Y. Liu, M. Yu, Y. Liu, H. Yu, J. Liu and B. Hu, "Oscillation cumulative volatile organic compounds on the northern edge of the north China plain: Impact of mountain-plain breeze," *Science of The Total Environment,* vol. 821, p. 153541, 2022.

[110] M. Tao, L. Chen, X. Xiong, M. Zhang, P. Ma, J. Tao and Z. Wang, "Formation process of the widespread extreme haze pollution over northern China in January 2013: Implications for regional air quality and climate," *Atmospheric environment,* vol. 98, pp. 417-425, 2014.

[111] Q. Huang, X. Cai, Y. Song and T. Zhu, "Air stagnation in China (1985–2014): climatological mean features and trends," *Atmospheric Chemistry and Physics,* vol. 17, no. 12, pp. 7793-7805, 2017.

[112] V. Shah, D. Jacob, K. Li, R. Silvern, S. Zhai, M. Liu, J. Lin and Q. Zhang, "Effect of changing NO x lifetime on the seasonality and long-term trends of satellite-observed tropospheric NO 2 columns over China," *Atmospheric Chemistry and Physics,* vol. 20, no. 3, pp. 1483-1495, 2020.

[113] T. Doumbia, C. Granier, N. Elguindi, I. Bouarar, S. Darras, G. Brasseur, B. Gaubert, Y. Liu, X. Shi, T. Stavrakou, S. Tilmes, L. F., D. A. and T. Wang, "The CONFORM covid-19 global emission factors," 2020. [Online]. Available: https://doi.org/10.25326/88. [Accessed 3 10 2023].

[114] G. A. Grell and S. R. Freitas, "A scale and aerosol aware stochastic convective parameterization for weather and air quality modeling," *Atmospheric Chemistry and Physics,* vol. 14, no. 10, pp. 5233-5250, 2014.

[115] H. Kusaka and F. Kimura, "Coupling a single-layer urban canopy model with a simple atmospheric model: Impact on urban heat island simulation for an idealized case," *Journal of the Meteorological Society of Japan. Ser. II,* vol. 82, no. 1, pp. 67-80, 2004.

[116] K. M. Han, R. S. Park, H. K. Kim, J. H. Woo, J. Kim and C. H. Song, "Uncertainty in biogenic isoprene emissions and its impacts on tropospheric chemistry in East Asia," *Science of the total environment,* vol. 463, pp. 754-771, 2013.

[117] B. Lamb, A. Guenther, D. Gay and H. Westberg, "A national inventory of biogenic hydrocarbon emissions," *Atmospheric Environment (1967),* vol. 21, no. 8, pp. 1695-1705, 1987.

[118] E. Slater, L. Whalley, R. Woodward-Massey, C. Ye, J. Lee, F. Squires, J. Hopkins, R. Dunmore, M. Shaw, J. Hamilton and A. Lewis, "Elevated levels of OH observed in haze events during wintertime in central Beijing," *Atmospheric Chemistry and Physics,* vol. 20, no. 23, pp. 14847-14871, 2020.

[119] K. Li, D. Jacob, H. Liao, Y. Qiu, L. Shen, S. Zhai, K. Bates, M. Sulprizio, S. Song, X. Lu and Q. Zhang, "Ozone pollution in the North China Plain spreading into the late-winter haze season," *Proceedings of the National Academy of Sciences,* vol. 118, no. 10, p. e2015797118, 2021.

[120] F. Zheng, Y. Yuan, Y. Ding, K. Li, X. Fang, Y. Zhao, Y. Sun, J. Zhu, Z. Ke, J. Wang and X. Jia, "The 2020/21 extremely cold winter in China influenced by the synergistic effect of La Niña and warm Arctic," *Advances in Atmospheric Sciences,* vol. 39, p. 546–552, 2022.

[121] X. Chen, S. Jeong, H. Park, J. Kim and C. R. Park, "Urbanization has stronger impacts than regional climate change on wind stilling: a lesson from South Korea," *Environmental Research Letters,* vol. 15, no. 5, p. 054016, 2020.

[122] T. Wang, L. Xue, Z. Feng, J. Dai, Y. Zhang and Y. Tan, "Ground-level ozone pollution in China: a synthesis of recent findings on influencing factors and impacts," *Environmental Research Letters,* vol. 17, no. 6, p. 063003, 2022.

[123] IPCC, "Revised 1996 IPCC guidelines for national greenhouse gas inventories," *Intergovernmental Panel on Climate Change,* 1997.

Acknowledgement

I would like to express my gratitude to my supervisor Prof. Guy P. Brasseur for his visionary and patient guidance of my doctoral research. During his supervisor, I have learned important experiences of understanding science and composing scientific stories. I also want to thank my supervisor Prof. Jürgen Ossenbrügge for his great support from the university side. I thank Max Planck Institute for meteorology for hosting me and providing me the office during my doctoral studies. I am grateful to the China Scholarship Council for funding four years of my doctoral studies and to the Merit Scholarship in University of Hamburg for financing my research for one year. I also would like to thank Prof. Eva-Maria Pfeiffer for being my panel chair.

Besides, I want to thank the School of Integrated Climate and Earth System Sciences (SICSS) for offering me valuable opportunities of participating in workshops, courses and social events. I thank the coordinator Dr. Berit Hachfeld for many helps over the years. I especially want to thank Ms. Marion Brusch from the Studienbüro Erdsystemwissenschaften for helping me clarify and solve the issues in my doctoral procedures.

I would like give many thanks to my colleagues Angelika, Cathy, Idir, Pablo, Jianing, Mengjiao, Ina, Natalia and Diego for their generous helps either in science or in personal life. I want to especially say thank you to Dr. Cathy Li, Dr. Idir Bouarar, Mr. Diego Arruda, Prof. Klaus Fraedrich and Prof. Guy P. Brasseur for reviewing the thesis draft and giving valuable comments. I acknowledge the contributions of Dr. Adrien Deroubaix to the thesis by proposing the nudging strategies, downloading of ERA5 reanalysis data, proposing the vertical profile of vertical emission injection, proposing the increase of vertical resolution, writing the script for vertical and temporal emission redistributions and writing the auto-resubmission script for cluster jobs. I thank the Deutsches Klimarechenzentrum (DKRZ) for providing numerical computing resources. I thank Dr. Claire Granier for inspiring the idea of downscaling and clarifying questions in the CAMS emission inventory. I thank Dr. Gabriele Pfister for advising the namelist of WRF-Chem simulations. I thank Dr. Stacy Walters for debugging the WRF-Chem source code for aircraft emission input. I thank Dr. Rajesh Kumar for providing chemical mapping from CAMS emission to MOZART-t1 chemical mechanism.

In the end, I would like thank my family for their support and understanding as well as my friend Patrick for his companionship for four years.

Eidesstattliche Versicherung

Declaration on Oath

Hiermit erkläre ich an Eides statt, dass ich die vorliegende Dissertationsschrift selbst verfasst und keine anderen als die angegebenen Quellen und Hilfsmittel benutzt habe.

I hereby declare upon oath that I have written the present dissertation independently and have not used further resources and aids than those stated.

Hamburg, den 29. Januar 2024

Xiaoqin Shi